Model of impedance changes in nerve fibres

Ilya Vitalievich Tarotin

A thesis submitted for the degree of

Doctor of Philosophy

of

University College London

Department of Medical Physics and Bioengineering

University College London

May 2019

Declaration

I, Ilya Tarotin, confirm that the work presented in this thesis is my own. Where information has been derived from other sources, I confirm that this has been indicated in the thesis.

Signed:

Abstract

Fast neural Electrical Impedance Tomography (EIT) is a method able to image electrical activity in nerves by measuring impedance changes (dZ) which occur as ion channels open. While it can image fast activity in large peripheral nerves, for imaging inside smaller nerves, the signal-to-noise-ratio must be maximized which requires optimization of EIT parameters. If optimized, fast neural EIT could be of benefit in the new field of electrical stimulation of autonomic nerves ("Electroceuticals") that could allow cross-sectional imaging of the fascicles and precise neuromodulation of internal organs supplied by them to treat associated medical conditions.

The purpose of this thesis work was to develop an accurate model of nerve fibres that could validate experimental data, predict optimal parameters for imaging with EIT and explain the nature of the observed signals. In chapter 2, relevant literature on EIT, membrane biophysics and existing models of nerve fibres is reviewed. Accurate 3D FEM models of unmyelinated fibres bi-directionally coupled with external space, including Hodgkin-Huxley giant axon of the squid (single and multiple) and mammalian C nociceptor are developed in chapter 3. The models explain available experimental data and optimize fast neural EIT in unmyelinated nerves. In chapter 4, an accurate FEM model of a myelinated fibre coupled with extracellular space is developed and utilized for the same purposes. Dispersion in unmyelinated fibres is studied in chapter 5 by development of the accurate FEM models of 50-fibre HH and C nociceptor nerves, followed by extension to the statistical models of realistic nerves with thousands of fibres. The models provide the maximum distances over which EIT may be used for imaging fascicular activity for each kind of nerve and showed that dZ could be seen further then compound action potential if it is biphasic.

Impact Statement

The work completed in this thesis covered implementation of bi-directionally coupled models of nerve fibres with the main goal of optimisation of fast neural EIT. This technique, when optimised, has a potential to non-invasively image compound activity in nerves that is beneficial for the new field of electroceuticals aimed at selective stimulation of the fascicles and subsequent neuromodulation of the internal organs supplied by them. If successful, it will allow treatment of various illnesses that do not usually respond to conventional therapy. The main nerve of interest to date is the vagus nerve which is the main autonomic nerve in the body supplying many vital internal organs. Through stimulation of the specific vagal fascicles, the illnesses to be potentially treated include diabetes, which may be addressed by neuromodulation of the pancreas leading to an insulin release; epilepsy, by suppressing the seizures, or rheumatoid arthritis, by inhibiting expression of inflammatory cytokines through the cholinergic anti-inflammatory pathway.

In addition, a novel methodology developed in this work can help to build accurate models of any types of nerves. Their applications may include optimisation of various medical techniques for further clinical usage or studying underlying causes of a broad spectrum of nerve related disorders. Biophysical explanation of the measured data can also be of a significant value for understanding the physiology of the nerve subjected to small currents and underlying the impedance measurement experiments. Discussed benefits can be brought about via setting up collaboration with researchers from different disciplines. All the findings were submitted to or published in peer-reviewed journals so that they can be used immediately.

Acknowledgements

First, I would like to thank my supervisor Prof David Holder for providing this exciting opportunity to join the EIT group at UCL and his continuous support throughout the whole duration of my PhD.

I would also like to thank all my friends in the EIT group for the productive stimulating environment and help along the way towards a degree. I am particularly grateful to Dr Kirill Aristovich who supported me during the project in all possible ways providing numerous great ideas as well as helping with all arising modelling issues and postprocessing analysis. I highly appreciate thought-provoking questions asked by Dr Martin Smith which often led to helpful discussions and new ideas. The quality of writing in the published papers and this thesis was profoundly improved by careful reviewing done by members of the EIT team.

I am very thankful to my second supervisor Prof Kenneth Harris for valuable ideas during the initial stages of the project and the transfer viva. This work would not have been possible without the funding kindly provided by GSK/Galvani Bioelectronics which enabled me to conduct this research and do what I really enjoy.

Finally, I am especially grateful to my mother and my girlfriend Ksenia who provided inestimable support and encouragement during four long years when I was studying abroad.

Contents

Contents

List of Abbreviations

AC	Alternating Current
AP	Action Potential
BC	Boundary Condition
CAP	Compound Action Potential
CV	Conduction Velocity
DC	Direct Current
dZ	Impedance Change
EAP	Extracellular Action Potential
EIT	Electrical Impedance Tomography
FEM	Finite Element Method
FLUT	Fluted Segment
HH	Hodgkin-Huxley
MYSA	Myelin Sheath Attachment Segment
PDE	Partial Differential Equation
PSD	Power Spectral Density
S.D.	Standard Deviation
SNR	Signal-To-Noise Ratio
STIN	Stereotyped Internodal Segment

List of Figures

List of Figures

List of Tables

Chapter 1
Introduction

1.1 Overview

The work described in this thesis is a part of an electroceuticals project that aims at treating illnesses by selective stimulation of neural fascicles innervating specific internal organs (Famm *et al.*, 2013; Waltz, 2016). For example, stimulation of the vagus nerve supplying all major organs in the body was previously shown to have anti-inflammatory action (Bonaz *et al.*, 2016) as well as to positively affect treatment of heart failure (Gold *et al.*, 2016), epilepsy (Ben-Menachem, 2002) and rheumatoid arthritis (Koopman *et al.*, 2016). However, selectivity of stimulation is essential for improvement of treatment efficiency and avoidance of unexpected side effects arising from modulation of non-targeted organs.

In order to selectively stimulate the neural fascicles, it is essential to know their precise location within the nerve. Furthermore, it is impossible to organise closed-loop neuromodulation without functional activity measurement of the fascicle of interest. Electrical impedance tomography (EIT) is a method that could provide both capabilities. EIT is based on the reconstruction of images of electrical impedance changes (dZ) of an object by injecting direct or alternating currents (DC or AC) and recording voltages measured with electrodes placed on the object's surface. With EIT it is possible to image slow dZ occurring due to blood flow changes or cell swelling during epilepsy, stroke, spreading depression or evoked activity. These physiological events cause resistance changes of the order of 10% occurring over seconds (Holder, 2004*a*). Additionally, EIT is capable of imaging fast dZ during neuronal depolarization

occurring over milliseconds (Holder, 1992; Gilad *et al.*, 2009; Hannan *et al.*, 2018; Faulkner *et al.*, 2018*a*; Aristovich *et al.*, 2018) that is referred to as fast neural EIT.

Fast neural EIT has been successful in imaging depolarization in the cerebral cortex of the rat during evoked potentials (Aristovich *et al.*, 2016; Hannan *et al.*, 2018; Faulkner *et al.*, 2018*a*) as well as in visualising independently stimulated tibial and peroneal branches of rat sciatic nerve in its cross-section (Aristovich *et al.*, 2018). The principle of its operation is based on imaging the apparent dZ which occur when ion channels open during tissue excitation. When this happens, the applied EIT current starts passing through the open ion channels leading to a decrease in the recorded voltages proportional to the impedance. As a membrane can be classically represented as a parallel capacitance and a resistance, the dZ is expected to be inversely proportional to the frequency of the applied current, reaching maximum values at DC. A previously developed passive electrical model of the nerve fibres has shown this relation (Liston *et al.*, 2012). In contrast, recent experiments carried out in UCL EIT laboratory showed that the dependence of dZ on current frequency may be different. For example, it was shown that dZ in rat sciatic nerve could only be measured at above 4 kHz AC with the highest signal-to-noise ratio (SNR) observed at 6 kHz (Aristovich *et al.*, 2018). Other experiments also demonstrated an impedance increase at several AC frequencies that was not predicted with the passive model (Vongerichten, 2015). Therefore, the developed passive model was inadequate for accurate representation of the experimental data, so the new model with active voltage-gated ion channels is required which would better explain observed phenomena.

The impedance changes measured in fast neural EIT have amplitudes of the order of 0.1% even in the case of activation of the whole mainly myelinated nerve following its electrical stimulation (Aristovich *et al.*, 2018) and they are even smaller in unmyelinated nerves. Therefore, the signal-to-noise ratio (SNR) of the measured dZ signals during spontaneous physiological neuronal activity is expected to be extremely low that makes it impossible to obtain reliable images of such activity. To improve SNR and enable imaging, EIT parameters require optimization. These parameters include amplitude and frequency of the injected current, size and location of the electrodes and specifications of signal processing utilised to obtain dZ signals from the recorded voltages. With the determined optimal parameters, maximal possible dZ

could be recorded and the best possible images of the cross-section of the nerve could be obtained.

The approach generally used for optimisation is *in silico* modelling. A realistic and validated model of the nerve would predict the ideal parameters for imaging nerve fibres at the fascicular level with EIT, help to validate and interpret recent experimental data obtained in the laboratory as well as explain the biophysical nature of the observed dZ.

At present, there is no model that broadly represents all the properties and parameters of nerve fibres in 3D space. The existing models have certain limitations: some do not have realistic ion channels representing complex features of action potentials (AP) in mammalian nerve fibres (Hodgkin & Huxley, 1952; Frankenhaeuser & Huxley, 1964), while others lack the functionality of simultaneous coupling with external space in both directions (McIntyre *et al.*, 2002; Howells *et al.*, 2012; Tigerholm *et al.*, 2014; Sundt *et al.*, 2015). The models developed in this thesis cover all of the relevant processes, including simulation of the accurate spatial structure of the unmyelinated and myelinated fibres possessing experimentally validated ion channels, as well as modelling of multiple interacting fibres. At the same time, they allow for the stimulation of fibres via external electrodes and simultaneous recording of the extracellular electric field being generated by the fibres, known as bi-directional coupling. Using this approach, accurate electrical behaviour of nerve fibres in three-dimensional space has been simulated and optimal parameters for imaging with fast neural EIT have been determined.

1.2 Purpose

The main purpose of the study presented in this thesis is to optimize fast neural EIT in peripheral nerves. For this, a complete active model of the nervous tissue bi-directionally coupled with external space has to be developed. Such a model should correctly predict interaction between the applied current and the tissue as well as include both unmyelinated and myelinated fibres.

General points to be addressed include the following:

1. Development of a 3D FEM model of a single and multiple unmyelinated nerve fibres to:
   a. Determine the optimal parameters for obtaining the largest dZ signal;
   b. Verify the recently obtained experimental data;
   c. Identify biophysical origin of the measured dZ;
   d. Examine how dZ varies with the number and properties of modelled fibres;
2. Development of an accurate FEM model of a mammalian myelinated nerve fibre for the same purposes;
3. Design of the accurate and statistical nerve models to study how dispersion affects the dZ in various scenarios for various nerves.

1.3 Statement of Originality

The work presented in this thesis is all my own and has not been previously submitted for a degree in a University. Nevertheless, as the fields of biophysics and Electrical Impedance Tomography are very interdisciplinary, I was always able to discuss and receive all necessary assistance from my supervisor and my colleagues.

My supervisor Prof David Holder helped me a lot regarding the strategy of the project, experimental design, structuring of the thesis and its presentation. The main work presented in this thesis would not be possible without the help of my colleague Dr. Kirill Aristovich, who provided invaluable assistance during every aspect of the projects including setting up the models, their implementation and optimisation as well as throughout analysis of the data generated with them.

I have received helpful assistance from my second supervisor Prof. Kenneth Harris regarding the project outline and strategy. Prof. Hugh Bostock, who works at the Institute of Neurology, helped me to find relevant literature which made the process of familiarizing with different existing models much easier. My colleagues Dr Kirill Aristovich and Dr Martin Smith helped with reviewing English and scientific issues in the published and submitted papers as well as the final version of the thesis.

1.4 List of Publications

The work presented in this thesis has been published or accepted for publication in the following peer-reviewed journal papers:

- **Chapter 3.** Tarotin I, Aristovich K & Holder D (2019). Model of Impedance Changes in Unmyelinated Nerve Fibers. *IEEE Trans Biomed Eng* **66,** 471–484. doi: 10.1109/TBME.2018.2849220.

- **Chapter 4.** Tarotin I, Aristovich K & Holder D (2019). Simulation of impedance changes with a FEM model of a myelinated nerve fibre. *J Neural Eng*. Accepted for publication in June 2019. doi: 10.1088/1741-2552/ab2d1c.

- **Chapter 5.** Tarotin I, Aristovich K & Holder D (2019). Effect of dispersion in nerve on compound action potential and impedance change: a modelling study. *Physiol Meas* **40**, 034001. doi: 10.1088/1361-6579/ab08ce.

Chapter 2
Literature review

2.1 Electrical Impedance Tomography (EIT)

2.1.1 Bioimpedance

During the application of a current or voltage to a biological tissue, the electrical properties of the tissue itself can be described by its impedance, *Z* (Holder, 2004*b*). The tissue can be modelled as a parallel resistance and a capacitance (RC circuit), so the lipid cell membrane is represented by the capacitance and extracellular and intracellular spaces as the resistances conducting current through ion diffusion (Figure 2.1a).

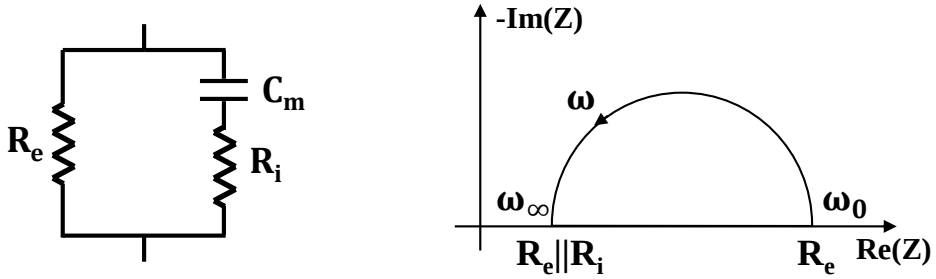

(a) (b)

Figure 2.1 (a) Electrical circuit of an excitable cell; (b) Cole-Cole plot of the circuit: dependence of complex impedance on frequency.
R_i and R_e are intracellular and extracellular resistances, C_m is the membrane capacitance.

The impedance of the tissue in this case is:

$$Z(\omega) = \frac{R_e R_i + R_e / j\omega C_m}{R_e + R_i + 1/j\omega C_m} \tag{2.1}$$

where R_i and R_e are intracellular and extracellular resistances in $[Ohm]$, C_m is the membrane capacitance in $[F]$, ω is angular AC frequency, $[rad/s]$.

The important property of the tissue impedance is that it changes with frequency due to the frequency dependence of the capacitive reactance. At low frequencies current does not penetrate the cell membrane and flows only through the extracellular space:

$$\lim_{\omega \to 0} Z(\omega) = R_e \tag{2.2}$$

With the increase of the frequency, the current starts flowing into the intracellular space and the imaginary component of the impedance starts to increase. The real and imaginary components of the impedance can be represented as:

$$Re(Z) = \frac{R_e R_i (R_e + R_i) + \frac{R_e}{(\omega C_m)^2}}{(R_e + R_i)^2 + \frac{1}{(\omega C_m)^2}} \tag{2.3}$$

$$Im(Z) = -\frac{R_e^2 / \omega C_m}{(R_e + R_i)^2 + \frac{1}{(\omega C_m)^2}} \tag{2.4}$$

The ratio between the real and imaginary parts of the impedance defines the phase angle θ between the current and the voltage:

$$tan(\theta) = \frac{Im(Z)}{Re(Z)} \tag{2.5}$$

At very high frequencies the capacitance remains uncharged and the impedance becomes resistive again, but has lower magnitude:

$$\lim_{\omega \to \infty} Z(\omega) = \frac{R_e R_i}{R_e + R_i} \tag{2.6}$$

The discussed dependence of impedance on frequency can be demonstrated in the Cole-Cole plot which was previously used by Cole and Cole to study properties of dielectrics (Cole & Cole, 1941) (Figure 2.1, b).

2.1.2 General principles of EIT

Electrical impedance tomography (EIT) is a technique which allows images of apparent electrical impedance changes (dZ) to be reconstructed from voltages measured with surface electrodes. The main principle of EIT is the injection of alternating current through a pair of electrodes and recording the voltages at the remaining ones. Several hundred measurements can be made by switching between injection electrode pairs (Holder, 2004*a*; Bayford, 2006). Then, with the use of numerical methods such as finite element method (FEM) and inverse problem techniques, tomographic images of the internal electrical impedance of the tissue can be reconstructed.

Impedance of neural tissue imaged with EIT can be subdivided into two categories: slow, occurring over seconds, and fast – over milliseconds.

Slow dZ may occur either due to cell swelling during ischemia or energy supply failure, when the water moves from extracellular space to cells; or because of blood flow, volume or temperature changes during different kinds of physiological activity. In all these cases, dZ are a few percent over several seconds (Holder, 2004*a*). EIT is able to image slow dZ in thorax occurring during cardiac cycle and pulmonary perfusion (Eyuboglu *et al.*, 1987), in stomach during gastric emptying (Smallwood *et al.*, 1994) as well as to clinically monitor lung function during ventilation (Frerichs, 2000).

Fast dZ occur during neuronal depolarization by a fraction of a percent with milliseconds durations. The first measurements of the dZ during fast neural activity were made by Cole and Curtis on Nitella and the giant axon of the squid (Cole & Curtis, 1939): they showed that the impedance of the axon significantly decreases during excitation and this decrease is associated with ionic properties of the membrane. At the same time, the capacitance and phase angle remain almost unchanged. Imaging of fast dZ was successfully performed in various recent studies (Aristovich *et al.*, 2016, 2018; Hannan *et al.*, 2018; Faulkner *et al.*, 2018*a*) but the technique is still being developed and improved.

Impedance measurements are based on the Ohm's law:

$$Z = \frac{V}{I} = \frac{|V|e^{j(wt+\varphi_V)}}{|I|e^{j(wt+\varphi_I)}} = |Z|e^{j(\varphi_V-\varphi_I)} \tag{2.7}$$

where I is the current injected using a current source, V is the voltage produced on the surface of the tissue, and Z is the sought for impedance. Z, V and I are complex values with the amplitudes |V|, |I| and |Z| and phases φ_V, φ_I and $\varphi_Z = \varphi_V - \varphi_I$. In real applications, $\varphi_V \approx \varphi_I$ (Cole & Curtis, 1939), so absolute values of Z are usually measured and reconstructed (Aristovich *et al.*, 2016, 2018).

2.1.3 Methods for imaging neural activity

Visualisation of neural activity always attracts considerable interest. Knowledge of the nature and location of the activity permits to gain insight into how the brain or nerves process information associated with various cognitive or physiological events. This, in turn, can be a vital step in better understanding their operation and mechanisms, and can be helpful in treating associated illnesses.

Methods able to image neural activity can be subdivided into two groups known as penetrating, where electrodes are injected into the tissue and non-penetrating where they are placed on its surface or at a small distance from it. Penetrating methods mainly include the use of microelectrode arrays (MEAs) for direct recording of the membrane

currents from a population of cells. For instance, Utah or Michigan arrays can be used for accurate visualisation of the neural activity but they are highly invasive that increases the risk of affecting normal physiology and causing damage to the tissue (Maynard *et al.*, 1997; Yoshida Kozai *et al.*, 2012). Non-penetrating methods consist of inverse source localization of the recorded electromagnetic fields (like EEG or MEG), voltage-sensitive optogenetics, positron emission tomography (PET) and functional magnetic resonance tomography (fMRI).

Neural activity can be visualised via inverse modelling of the recorded electrical or magnetic fields. While high temporal resolutions can be obtained (<1 ms), the spatial resolution is worse than in the majority of other techniques (Baillet *et al.*, 2001). For example, inverse modelling of electrical activity recorded from the surface of the sciatic nerve of the rat has recently been shown to have significantly worse spatial accuracy than EIT for imaging fascicles inside this nerve (Aristovich *et al.*, 2018). Also, the inverse problem does not have a unique solution and therefore requires introducing simplifying assumptions that decreases the probability of successful imaging (Hämäläinen *et al.*, 1993; Baillet *et al.*, 2001).

PET can image metabolic activity of the tissue by applying biologically active molecule containing radioactive positron-emitting tracer. Temporal and spatial resolutions of PET are poor (seconds, >8 mm) (Ollinger & Fessler, 1997) which is unsuitable for imaging small entities, such as nerves.

fMRI is a relatively modern non-invasive technique allowing to image inside the brain and possibly in the nerve. However, because it does not image the neural activity itself but the associated changes in blood flow, it has poor time resolution measured in seconds (Ogawa *et al.*, 1998).

Voltage sensitive optical imaging allows monitoring activity of neural tissue with the use of optical sensors that change its fluorescence properties. The concept of the technique is in application of light to the tissue covered with sensors and subsequent recording of the resultant level of light emission. Optical sensors, also known as voltage sensitive dyes, work by binding to the cell membrane – they react to the change in membrane potential or in the concentration of calcium ions (Hillman, 2007). Images can be obtained using confocal or higher resolution two- or three-photon microscopy techniques.

In a confocal microscopy a laser beam is directed into the tissue and a signal from the depth level being in focus is recorded; out of focus signals are rejected using a spatial filter. Although confocal microscopy allows imaging inside the tissue, it uses visible range excitation wavelengths where absorption and tissue scattering (photon absorption and reemission in random directions) increase. A laser beam cannot focus at depths exceeding 200-300 μm resulting in infeasibility of imaging deeper than that (Hillman, 2007; Ntziachristos, 2010). Two-photon microscopy is based on the principle where two low-energy near-infrared photons are nearly simultaneously absorbed by a tissue causing excitation of fluorophore at visible wavelength. Compared to confocal microscopy, scattering and absorption are less for higher near-infrared wavelengths allowing it to image deeper into the tissue (up to 600 μm) and get very high spatial resolution (<1 μm) (Ntziachristos, 2010). Similar principle is used in three-photon microscopy, which is able to exceed the depth limit of two photon microscopy to 1 mm (Horton *et al.*, 2013; Ouzounov *et al.*, 2017). However, these techniques demand high flux of photons for excitation that is achievable only with very expensive high energy femtosecond lasers (Hillman, 2007; Horton *et al.*, 2013). The discussed optical methods also require higher exposure resulting in additional time needed to capture a single image that can significantly decrease temporal resolution. Also, these techniques have very small fields of view (<1 mm^2) (Ntziachristos, 2010) and therefore insufficient imaging volumes (<1 mm^3) that will not allow visualisation of large scale structures as entire brain or nerves.

2.1.4 Fast neural EIT

Fast neural EIT is a novel technique which allows imaging impedance changes in neural tissue arising from the opening of ion channels during its depolarization. This technique is advantageous compared to the other methods discussed above: it is cheap, it has better spatiotemporal resolution (Hannan *et al.*, 2018; Faulkner *et al.*, 2018*a*; Aristovich *et al.*, 2018), it has a unique solution (Harrach, 2019) and it is non-invasive which is desirable for medical applications – surface electrodes currently used in EIT cause no damage or fibrosis to the tissue (Hannan *et al.*, 2019).

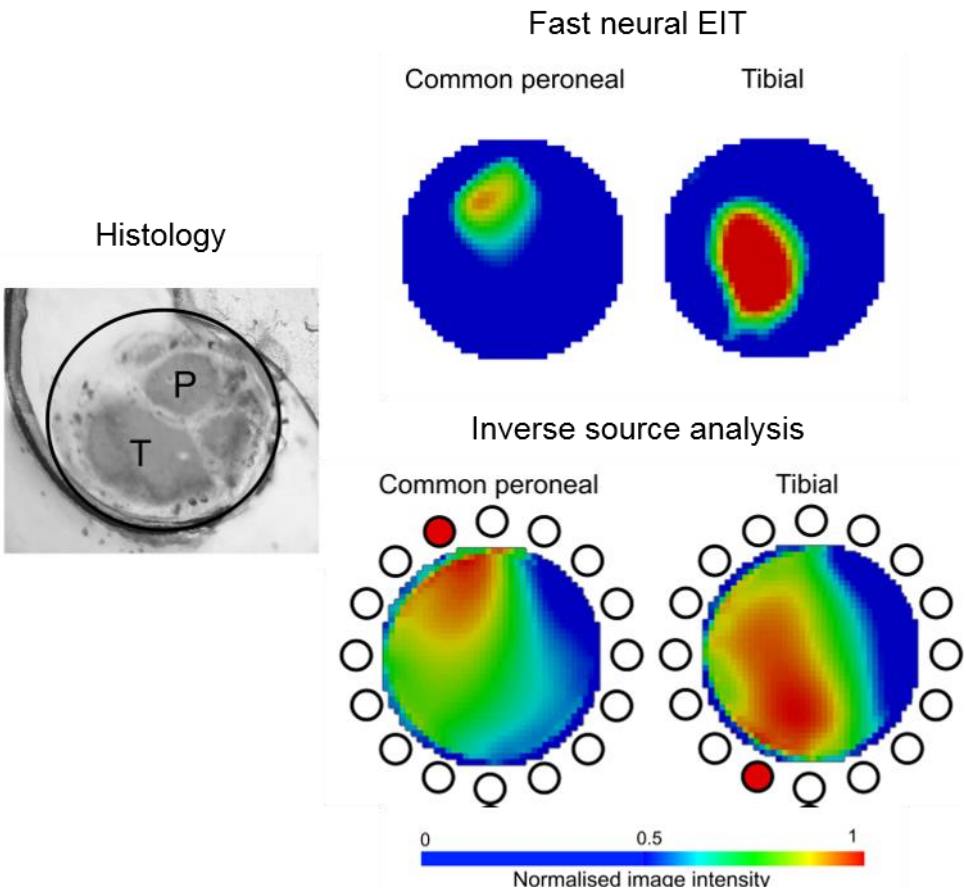

Figure 2.2 Images of fascicle activity in the sciatic nerve of the rat obtained by (Aristovich *et al.*, 2018).
Histology (left), corresponding images produced using fast neural EIT and inverse source analysis using the recorded compound APs (right).

Fast neural EIT has been shown to be successful in imaging fast neural activity of somatosensory cerebral cortex of the rat during evoked potentials with the use of 30 electrode surface epicortical arrays. The temporal and spatial resolutions of the imaged changes were up to 2 ms and 200 µm respectively (Aristovich *et al.*, 2016). Imaging evoked potentials at up to 2.5 mm below the surface of the rat cortex (Faulkner *et al.*, 2018*a*) as well as ictal epileptiform discharges in the cortex (Hannan *et al.*, 2018) were also shown to be feasible with similar resolution.

Fast neural EIT was also capable to localize functional activity in peripheral nerves. Recently, imaging of electrically-evoked activity in a cross-section of a rat sciatic nerve during compound action potential propagation was accomplished with a temporal resolution of 0.3 ms and spatial resolution of < 100 µm (Figure 2.2) (Aristovich *et al.*, 2018). In this study, peroneal and tibial fascicles of the main branch

of the sciatic nerve were visualized following the electrical stimulation of the posterior peroneal and tibial nerves. For this, a flexible cylindrical microelectrode cuff with 16-32 electrodes was used for application of alternating currents and recording of voltages. In another recent study (Chapman *et al.*, 2019) and using the similar approach, images of the recurrent laryngeal nerve (RLN) of the sheep at a fascicular level were obtained. For this, following electrical stimulation of RLN, a 28-contact microelectrode cuff was used for AC injection (9 kHz) longitudinally along the nerve and simultaneous activity was recorded in the cervical vagus nerve.

However, producing images in autonomic nerves is more challenging due to a lower signal-to-noise ratio (SNR) originating from two main reasons. First, autonomic nerves mainly consist of small unmyelinated fibres (C fibres) (Prechtl & Powley, 1987; Soltanpour & Santer, 1996; Shimizu *et al.*, 2011) producing lower dZ; second, conduction velocities of C fibres are significantly slower and variable (Coleridge & Coleridge, 1984) that causes dispersion of action potentials along the nerve so that compound AP and the corresponding dZ may not be visible beyond a few centimetres from the point of stimulation (Boone, 1995; Aristovich *et al.*, 2018). If imaging inside autonomic nerves is accomplished, EIT may be applied to the new area of bioelectronic medicines, or electroceuticals (Famm *et al.*, 2013; Waltz, 2016), which aims to treat diseases by selective electrical stimulation of fascicles inside these nerves resulting in modulation of associated internal organs. To accomplish successful imaging, the optimal EIT parameters to obtain the largest possible dZ must be found that can be achieved using computational modelling.

The classic explanation of the mechanism and physiological basis of fast neural EIT is based on a simple model of a neural membrane which is represented as a parallel connected resistance formed by ion channels and a capacitance produced by a lipid bilayer (Figure 2.3a). When a neuron depolarizes, the ion channels that were previously closed - open, and the resistance decreases. AC current starts flowing through them causing a decrease in the bulk resistance of the tissue over milliseconds. Hence, qualitatively, the resistance of the depolarized neural tissue is expected to decrease while the extra ion channels remain open. Currents of higher frequencies can flow inside the neural tissue through capacitance in any state of ion channels, so the decrease of the impedance for higher frequencies will be lower with the highest value

achieved at DC. Previous modelling of the nerve based on the passive cable model where resistance could assume two states (Figure 2.3a) predicted this impedance-frequency dependence (Liston *et al.*, 2012).

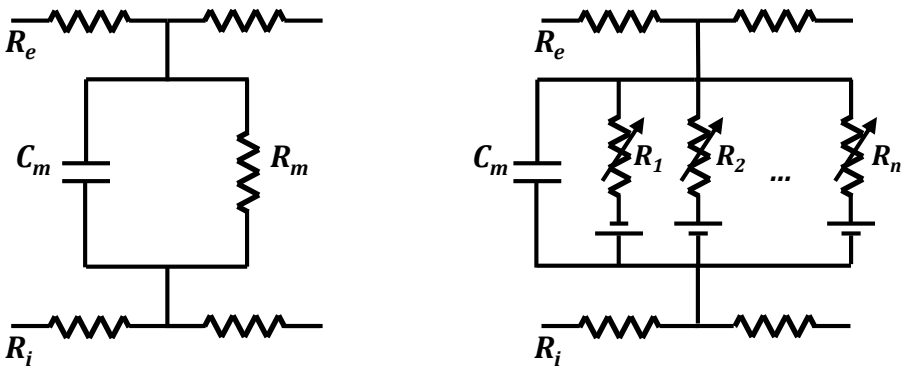

(a) (b)

Figure 2.3 Representation of the membrane as (a) a simple RC circuit model where R_m can assume two (opened and closed) states and (b) an active model with voltage dependent resistances – ion channels.
R_e and R_i designate extracellular and intracellular longitudinal resistances, C_m is the capacitance of the lipid bilayer, batteries represent the electrochemical gradients of ions 1, 2, …, n.

In contrast, the recently undertaken experiments have shown that the dependence of apparent impedance decrease on EIT current frequency is different from a simple decrease with frequency. These measurements differed from this model in one of the following ways: 1) the dZ did not monotonically decrease with AC frequency across the whole frequency range (Faulkner *et al.*, 2018*b*); 2) the dZ did not decrease to ~0 at frequencies higher than 1 kHz but was sustained at about -0.1% (Faulkner *et al.*, 2018*b*); 3) an increase in the dZ was measured (Vongerichten, 2015) or 4) the dZ could not be measured at frequencies lower than 4 kHz (Aristovich *et al.*, 2018).

The reason for this difference is that the value of the resistance of the real membrane depends on the voltage across it (Hodgkin & Huxley, 1952). In other words, ion channels are voltage-gated, so that they can interact with the alternating current injected during EIT (Figure 2.3b). Thus, unlike the simple model where ion channels assume discrete open and closed states, the active membrane has a highly nonlinear resistance-voltage dependence that is influenced by applied currents of various

frequencies. This leads to the need for a new accurate models of nerve fibres the development of which was the main purpose of this project.

2.2 Excitable cell membrane

The cell membrane (or plasma membrane) is the outer layer of the cell that contains a lipid bilayer and embedded proteins serving as diffusion barriers and referred to as ion channels. The main functions of the membrane are to protect the cell from the surrounding medium and to control the transport of ions through it into and out of the cell.

2.2.1 Ion channels in nerve fibres

Membranes in all biological cells have pores called ion channels. Ion channels play a fundamental role in the life of the cell and control diversity of the mechanisms occurring inside it. Typical ion channels consist of proteins embedded into the lipid bilayer of the membrane (Figure 2.4). These proteins have a small central pore selectively permeable for ions, which can change the state to opened or closed in reaction to various stimuli. The property of ion channels by means of which ions can move from inside to outside of the cell and vice versa is called gating. This is critical for establishing resting potentials and excitation of the membrane, as well as for regulation of the cell volume. To permit only the specific types of ions into or out of the cell, ion channels have selectivity filters and voltage sensors, so that they are permeable only for ions with specific charge or binding structure (Schmidt & Thews, 1989; Hille, 2001).

Movement of different substances through ion channels occurs because of the existence of concentrations and electrical gradients at the different sides of the membrane. For example, the concentration of the potassium ions outside of the cell is much lower than inside leading to outward K current through potassium channels. This makes the largest impact in establishing resting potential of the membrane.

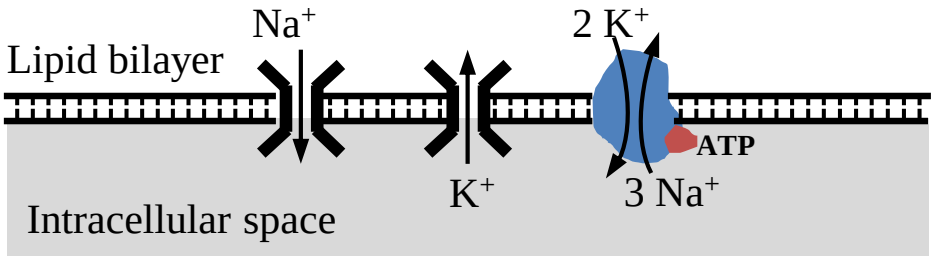

Figure 2.4 Schematic representation of ion channels embedded into the membrane. Sodium and potassium channels as well as the Na/K ATPase are presented.

Alternatively, when the membrane is depolarized, equilibrium of concentration and electrical gradients is violated. This leads to the closing of potassium ion channels and the opening of sodium ones, allowing sodium ions to be transported inside the cell (Hille, 2001). This is the basic mechanism of generation of action potential.

This section will describe several different types of ion channels found in mammalian nerves. Some channels are omitted from consideration because they either only play a background role in regulating excitation in the axonal part of neurons, like calcium channels (Meves & Vogel, 1973; Baker *et al.*, 1975; Hille, 2001) or are not frequently found there, like chloride channels (Hille, 2001).

Sodium (Na) channels

Sodium (Na) channels carry sodium ions and are responsible for generating the rapid regenerative upstroke of action potential in axons. They have the ability to quickly open and close leading to the membrane depolarization and subsequent inactivation. Apart from opened and closed states, these channels also have a state known as inactivated (Hille, 2001): it follows opening of the channels during depolarization and prevents these channels to be quickly activated again before repolarization or hyperpolarization of the neuron. Na channels are present in myelinated and unmyelinated axons, neuron cell bodies, vertebrate skeletal and cardiac muscles, endocrine glands; they are very similar in function and much less diverse than potassium channels (Finn & LoPresti, 2002).

There are two types of Na channels: voltage-gated and ligand-gated. Voltage-gated ion channels react to the change in the membrane potential while ligand-gated channels

open in response to certain chemical substances close to it by binding with them. The voltage-gated channels are of the utmost interest as they are much more widespread and play a critical role in propagation of action potentials (Hille, 2001) to be simulated in this thesis.

As ion channels are proteins, they differ in the sequences of amino acids they are formed of. These acids are produced from nucleotide sequences and are defined by certain genetic codes. The family of sodium voltage-gated channels forms a homologous gene superfamily consisting of 9 genes evolved from the same ancestral structure. Thus, the standard nomenclature of the Na voltage-gated channels ($Na_v1.1$ to $Nfa_v1.9$) is based on the genes from which corresponding proteins are formed (Goldin *et al.*, 2000).

Despite functional similarity of sodium channels, differences between them also exist. There are tetrodotoxin-sensitive ($Na_v1.1$, $Na_v1.2$, $Na_v1.3$ and $Na_v1.7$) and tetrodotoxin-resistant ($Na_v1.1$, $Na_v1.5$, $Na_v1.8$ and $Na_v1.9$) sodium channels which are expressed in different tissues and possess various kinetic properties (Campbell, 1992; Goldin *et al.*, 2000). For example, $Na_v1.1$, $Na_v1.2$, $Na_v1.3$ and $Na_v1.6$ are mostly present in neurons of the central nervous system, $Na_v1.4$ and $Na_v1.5$ – in the skeletal muscle and the heart (Goldin *et al.*, 2000). $Na_v1.7$, $Na_v1.8$ and $Na_v1.9$ have been found in axons of peripheral nerves (Toledo-Aral *et al.*, 1997; Djouhri *et al.*, 2003; Sheets *et al.*, 2007).

$Na_v1.7$ channels participate in generation of action potentials: they rapidly activate at the start of the depolarization phase but deactivate before the AP reaches its peak value (Sheets *et al.*, 2007). In contrast, $Na_v1.8$ current activates and inactivates much more slowly, appears during all stages of the action potential and plays the dominant role in its generation (Blair & Bean, 2002). $Na_v1.9$ is a conceptually different channel as it only weakly participates in action potential generation but flows persistently and has slow inactivation. It comprises about 5% of the transient sodium current and has functional significance in setting subthreshold excitability and resting potential (Kiss, 2008; Maingret *et al.*, 2008).

Potassium (K) channels

The main function of potassium (K) channels, permeable to K^+ ions, is to stabilize membrane potential: they repolarise the membrane in the end of an action potential, have the largest impact in setting the resting potential, set the minimal interval between repetitive action potentials and have many other functions. A huge variety of K channels are expressed in the majority of excitable cells (Hille, 2001).

The most widespread K channels are voltage-gated K channels (K_v) controlled by the change in the membrane potential. The broadest class of K_v channels are *delayed rectifier potassium channels (K_{DR})*, which activate with a delay after the preceding depolarization caused by influx of sodium current.

There are two types of delayed rectifiers – slow and fast. Slow ones are primarily located in cardiac cells and close to synapses. Fast delayed rectifiers are activated during the action potential and responsible for recovering the membrane potential to its resting values in its end. Various fast K_{DR} channels can be found in practically all excitable cells with the exception of nodes of Ranvier in mammalian myelinated fibres (Hille, 2001). Instead, K^+ ions flow through voltage independent leakage channels to repolarize the membrane. The nomenclature of voltage-gated K channels is similar to that of voltage-gated Na channels and based on the genes of the corresponding proteins (K_vx.y).

The M-type or *muscarinic K channels (K_M)* are expressed where neurons are regulated by neurotransmitters, such as acetylcholine and present mostly in the heart and sympathetic neurons (Brown & Adams, 1980). Any agonist for these receptors turns off the K_M current making neuron more responsive to synaptic stimuli so that it can fire bursts of spikes. Thus, the main function of K_M channels opened at rest is to slow down neuronal activity allowing neurons to fire single action potentials instead of bursts of repetitive spikes. For instance, K_M current helps to slow down the heart rate (Kunkel & Peralta, 1995).

A-type potassium channels (K_A), or transient outward K channels, are situated primarily near neuronal cell bodies and sensory terminals and can be found, for instance, in nodose ganglion and dorsal motor nucleus of the vagus (Cooper, 1989; Karschin *et al.*, 1998; McAlexander & Undem, 2000). K_A channels are rapidly

activated when a cell is starting to depolarize after the period of hyperpolarization and then quickly deactivated. Activation of K_A currents prevents fast depolarization of the fibre after closing the delayed rectifier K channels and opening Na channels. Thus, current through these channels slows down the frequency of repetitive firing of action potentials and helps to regulate interspike intervals (Hille, 2001).

K_{Na} channels, or sodium activated potassium channels, are potassium channels activated by increasing amounts of intracellular ions of Na^+. These channels are known to be present in small dorsal root ganglion (DRG) neurons, in the nodal region of myelinated axons and elsewhere in neurons where sodium ions accumulation is possible. Such accumulation usually occurs due to long repetitive firing of the neuron. *K_{Na}* channels do not actively contribute to formation of the AP but are responsible for stabilization of the resting potential (Bischoff *et al.*, 1998).

Hyperpolarization-activated cyclic nucleotide-gated (HCN) channels

HCN, or *h*- channels are a class of ion channels activated by hyperpolarization of the membrane and are present in the majority of neuronal cells in the peripheral and central nervous system as well as in the heart and smooth muscle (Lüthi & McCormick, 1998). These channels produce inward current through the membrane (I_h current or h-current) when it is hyperpolarized. They are permeable to both K^+ and Na^+ ions; permeability to Na^+ ions is much higher at lower levels of hyperpolarization. During further depolarization, when the transmembrane potential reaches potassium reversal potential, permeability to K^+ increases (Grafe *et al.*, 1997; Kouranova *et al.*, 2008).

The main function of h-current is to participate in establishing repetitive firing and pace making, as activation of this current leads to slow depolarization of the cell (DiFrancesco *et al.*, 1986; Lüthi & McCormick, 1998) which helps the membrane to fire with higher frequency. As some HCN channels are activated at rest, h-current plays an important role in determination of the value of the resting potential, increasing it by several millivolts. Also, these channels may form a significant part of the overall membrane conductance in a subthreshold state and therefore participate in regulation of neuronal responsiveness (Lüthi & McCormick, 1998).

Na^+/K^+-ATPase

Na^+/K^+-ATPase (Na-K pump) is an enzyme constantly pumping 3 ions of sodium out and 2 ions of potassium into the cell against their concentration gradients using the energy released from the hydrolysis of ATP. With every ATP molecule spent, the pump transports one positive charge out of the cell which, in total, leads to a decrease in resting potential by about 10 mV. Thus, one of the main functions of the pump is to help to maintain resting membrane potential (Hille, 2001). Another vital activity of Na^+/K^+-ATPase is to regulate cell volume by maintaining right concentrations of the ions inside and outside of the cell. Failure of the pump leads to flowing of ions inside the cell and its swelling.

Also, the energy stored in the gradient of Na^+ ions provided by the work of Na^+/K^+-ATPase is used by transport proteins to carry different substances like glucose or amino acids through the membrane. Such transport is vital for neurons and fully depends on the gradient of sodium ions and proper work of Na-K pump. The Na-K pump can be found in every cell of a living organism (Schmidt & Thews, 1989).

Leakage channels

Leakage ion channels are not voltage-gated, so their permeability is constant, and ions can flow through them upon the electrochemical gradient. These channels are present in the membrane of most neuronal cells and there is usually a prevalence of K^+ and Cl^- leakage channels that helps to establish resting potential (Hille, 2001).

2.2.2 Membrane potential

The difference between the internal and external electrical potential of the cell is called the membrane potential. The membrane potential is derived from the concentration and electric gradients of ions across the membrane inside and outside of the cell. According to the principles of diffusion, ions tend to move from the areas with higher concentration to the areas with lower concentration. Also, because ions are electrically charged, they are influenced by the electrical force trying to balance the

overall charge on the sides of the membrane. The ion flux through the membrane under the influence of these forces can be written as a Nernst-Planck equation (Johnston & Wu, 1995):

$$J_{ion} = J_{diff} + J_{el} = -D\frac{\partial[C]}{\partial x} + \sigma_{el}E = -\left(\frac{\mu kT}{q}\frac{\partial[C]}{\partial x} + \mu z[C]\frac{\partial V}{\partial x}\right) \qquad (2.8)$$

where J_{ion} is the ionic flux though the membrane, J_{diff} and J_{el} are fluxes due to diffusion and electrical forces, all in $\left[\frac{molecules}{cm^2 s}\right]$; D is the diffusion coefficient, $\left[\frac{cm^2}{s}\right]$; σ_{el} is electrical conductivity in $\left[\frac{S}{cm}\right] = \left[\frac{molecules}{V\ s\ cm}\right]$; $[C]$ is concentration in $\left[\frac{molecules}{cm^3}\right]$; E is electric field in $\left[\frac{V}{cm}\right]$; μ is mobility in $\left[\frac{cm^2}{Vs}\right]$; z is ion valence; k is Boltzmann's constant ($1.38 * 10^{-23}\left[\frac{J}{K}\right]$); T is temperature in $[K]$ and q is electric charge of the molecule in $[C]$.

When the membrane is at rest, the ionic flux through the membrane is zero and that is how Nernst equation for equilibrium potential is derived:

$$E_{eq} = \frac{RT}{zF}\ln\frac{[C]\text{-}_{out}}{[C]\text{-}_{in}} \qquad (2.9)$$

The value of the membrane potential in resting conditions is known as the resting potential. When the neuron is at rest, the membrane is highly permeable for potassium. For this reason, potassium ions flow out of the cell where their concentration is low, they carry positive charge that is therefore balanced by the negative charge appearing on the inner surface of the membrane. Therefore, the resting potential of the cell is always negative and close to the potassium reversal potential, approximately -70 mV (Johnston & Wu, 1995). Nevertheless, the value of the resting potential more or less depends on all the ions present inside and outside the cell and can be calculated with Goldman-Hodgkin-Katz voltage equation:

$$E_r = \frac{RT}{F} \ln \frac{P_K[K^+]\text{-}_{out} + P_{Na}[Na^+]\text{-}_{out} + P_{Cl}[Cl^-]\text{-}_{out} + \cdots}{P_K[K^+]\text{-}_{in} + P_{Na}[Na^+]\text{-}_{in} + P_{Cl}[Cl^-]\text{-}_{in} + \cdots} \quad (2.10)$$

where P is the permeability of the particular ion in $\left[\frac{m}{s}\right]$, $[I^+]$ is the concentration of the ion inside and outside of the cell in $\left[\frac{mol}{cm^3}\right]$, T is the temperature in $[K]$, R and F are the gas and Faraday's constants.

Maintaining the resting potential at negative values plays a vital role in normal excitation and sensitivity of the cells to synaptic inputs. Membrane potential depends not only on the quantity of the ions present in the cell and its surroundings but also on the work of the active Na^+/K^+-ATPase, that continuously pumps three ions of sodium out of the cell in exchange for two ions of potassium into the cell maintaining low intracellular concentration of Na^+ ions and high of K^+ ions and decreasing the resting potential by several millivolts.

2.2.3 Action potential

Neural cells, or neurons, can transmit information via electrical signals propagating along them. The action potential (AP) is the excitation wave moving along the excitable cell as the change in its membrane potential (Figure 2.5). When the AP occurs, the potential difference between internal and external surfaces of the cell reverses. APs are the basis of neural communication. They can propagate along axons to the axon terminals where they can be transmitted to other neurons through synaptic clefts.

The physiological basis of the AP can be explained by the activity of voltage-gated ion channels on the membrane, where sodium and potassium channels play a pivotal role. For the AP to happen, the membrane should be depolarized to the values above so-called threshold potential which varies among cells but usually equals about -30 mV (Hille, 2001). In this case the resistance of the sodium channels drops, and the inflow of the corresponding current rapidly increases. It causes the membrane potential to rise up to positive values. Then, after sodium channels close, potassium channels

start to open so that potassium ions flow out of the cell to reverse the potential back to the resting value, which is referred to as hyperpolarization. As the additional potassium ion channels are opened compared to the resting state, and as they cannot close immediately, afterhyperpolarization (AHP) phenomenon usually occurs after this stage. The time period during which membrane potential is lower than resting potential is called the refractory period (Figure 2.5). After occurrence of the AP the membrane needs time to recover to be able to fire again. This refractory period appears because after opening sodium channels become inactivated and can't immediately return to their resting closed state (Schmidt & Thews, 1989).

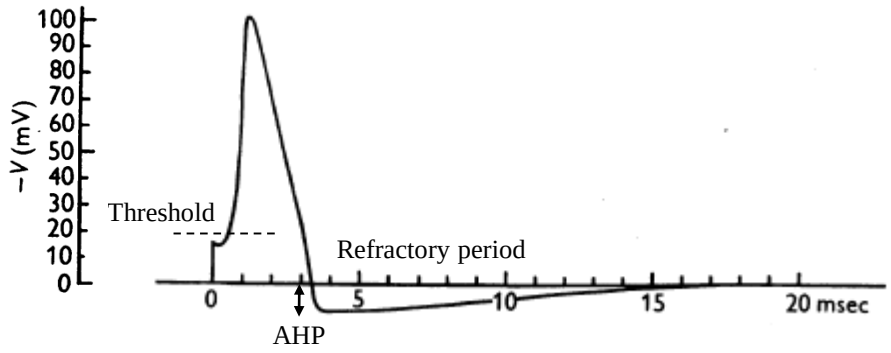

Figure 2.5 Action potential of the giant axon of the squid simulated by (Hodgkin & Huxley, 1952). Y axis represents the displacement of the membrane potential from the resting potential, $V = V_r - V_m$.

AP is subject to an all-or-none principle which means that its amplitude does not depend on the amount of the current which produced it if the voltage change reached the threshold. If it does not happen, the sodium current inflow is much smaller than resting potassium current, so the membrane potential returns to the resting value without generating an AP.

An AP initiated locally can spread or propagate along the axon. The ionic currents flowing inside and outside the axon can also flow along it thus depolarizing adjacent sections of the membrane. If this depolarization is enough for the membrane to reach the threshold, this may cause APs at these regions to spread further both ways along the axon (Figure 2.6).

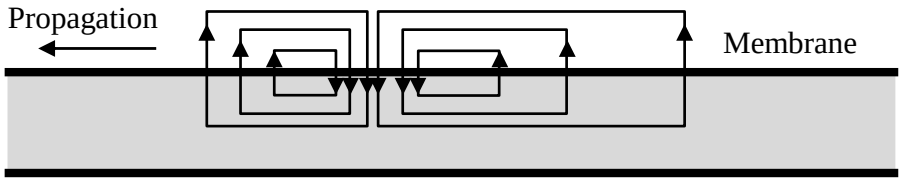

Figure 2.6 Mechanism of action potential propagation in unmyelinated axon.
Arrows depict the direction of ionic currents. The AP originates from the rapid influx of sodium ions into the membrane and subsequent slower outflux of potassium ions out of the membrane.

The conduction velocity (CV) of the AP is different for different types of fibres. In unmyelinated axons, where propagation occurs as explained above, APs spread with a speed of meters per second increasing with the square root of the diameter of the axon (Gasser, 1950). It may be qualitatively explained by the decrease of longitudinal resistance of the axon in respect to membrane resistance when the diameter of the axon is increased. This is because the membrane surface area is proportional to the diameter of the axon while its cross-sectional area is proportional to the square of the diameter. Consequently, longitudinal currents in the larger axons will spread at longer distances and that will increase the conduction velocity (Schmidt & Thews, 1989).

Unlike unmyelinated axons, APs in myelinated fibres conduct quickly and efficiently with the speeds of up to 100 m/s (Rushton, 1951). This is because the myelin sheath surrounding the axon is an insulator and increases the resistance of the membrane manifold. Therefore, current cannot cross the membrane under the myelin and can spread under it for long distances. The delays only occur at the nodes of Ranvier, very short sections on the myelinated fibre not covered with myelin, where the current has to depolarize the membrane and induce excitation. This is the nature of AP propagation in myelinated fibres known as saltatory conduction (Figure 2.7) (Schmidt & Thews, 1989).

Similarly to the unmyelinated fibres, CV in the myelinated fibres increases with their diameter but this relationship is close to linear (Rushton, 1951).

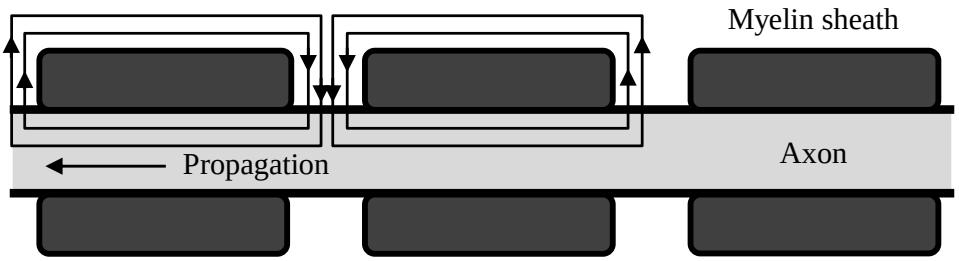

Figure 2.7 Mechanism of saltatory conduction in myelinated fibre.
Myelin sheath acts as an insulator so that ionic currents depicted by arrows can enter the axon only at the nodes of Ranvier.

2.2.4 Methods of recording membrane activity

Membrane activity and corresponding APs can be recorded in two main ways: intra- or extracellularly.

Intracellular recordings usually involve a microelectrode inserted into the axon with respect to an isopotential extracellular reference electrode (ground). One of the oldest and most frequently applied intracellular measurement techniques is the voltage clamp that was originally used by Hodgkin and Huxley in 1952 to study mechanisms of membrane excitation and develop their famous model of the squid giant axon (Hodgkin *et al.*, 1952; Hodgkin & Huxley, 1952). This method allows recording ionic currents through the membrane while holding the membrane voltage at a constant level using negative feedback. It is implemented by applying current through an injecting electrode while measuring transmembrane voltage through a recording electrode (in respect to ground) (Figure 2.8). Long silver wire electrodes are inserted into the axon during recording which makes it iso- or equipotential along its length or, in other words, space-clamped (Johnston & Wu, 1995). With this procedure, current through the membrane capacitance (Figure 2.3) is eliminated which allows recording ionic current exclusively. This can be seen in the equation for the total membrane current derived from the circuit in Figure 2.3 (full description is provided in Section 2.3):

$$I_m = I_{ion} + I_C = I_{ion} + C_m \frac{\partial V_m}{\partial t} = I_{ion} \; if \; V_m = const \tag{2.11}$$

where I_m is the total membrane current per unit length $\left[\frac{\mu A}{cm}\right]$; I_{ion} is the ionic current $\left[\frac{\mu A}{cm}\right]$; I_C is the capacitive current $\left[\frac{\mu A}{cm}\right]$; C_m is the membrane capacitance $\left[\frac{\mu F}{cm}\right]$ and V_m is the transmembrane voltage in $[mV]$.

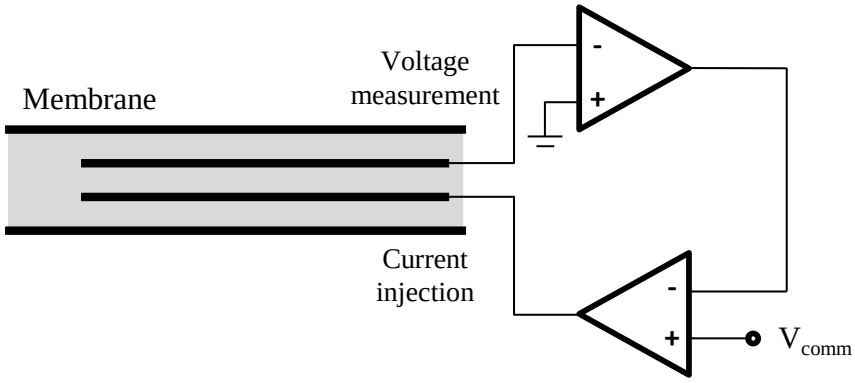

Figure 2.8 Scheme of two-electrode voltage clamp technique.
One electrode is used to record membrane potential and the other is for current injection. Long electrodes are utilised to space-clamp the axon (make it isopotential along the length); the negative feedback system is used to maintain the command voltage V_{comm} and measure the injected current.

The alternative way of intracellular recording very similar to voltage clamp is the current clamp technique where ionic currents through the membrane are held constant via negative feedback and changes in voltages are recorded (Johnston & Wu, 1995). APs recorded intracellularly are referred to as intracellular action potentials or simply action potentials (Figure 2.5).

The improvement of voltage clamp technique known as patch clamp is used to measure currents of very small areas on the membrane - even single ion channels. For this, the tip of a 3-5 µm diameter glass pipette filled with electrolyte solution is used to electrically isolate a small patch of membrane and reduce a background noise (Figure 2.9). The recording is performed by an electrode inserted into the pipette and connected to an amplifier relative to the reference electrode located in the extracellular medium (Neher & Sakmann, 1976). This technique offers a possibility of measuring very small ionic currents of single ion channels which allows thorough investigation of the physiological nature of processes occurring in neural tissues as well as inclusion of the correct ion channels into the biophysical models providing accurate representation of these processes (Llano, 1988; Sheets *et al.*, 2007; Sundt *et al.*, 2015).

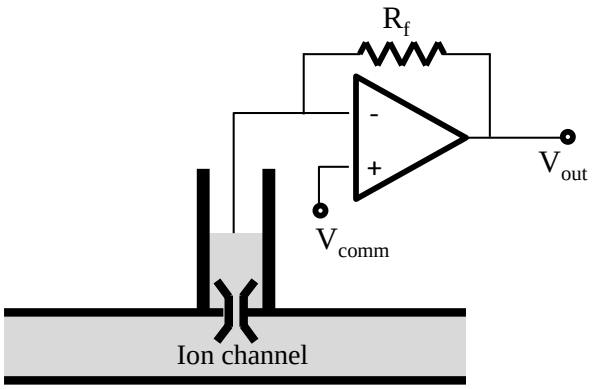

Figure 2.9 Scheme of a patch clamp technique.
A glass micropipette filled with an electrolyte solution serves for electrical sealing of the membrane. The ionic currents of a single isolated ion channels can be recorded by an electrode inserted into the pipette using a current to voltage converter with the feedback resistor R_f (transimpedance amplifier). Command voltage V_{comm} is maintained across the membrane using the voltage clamp technique.

Intracellular recording allows precise measurement of membrane electrical activity; however, the technique is complicated and there is a risk of damaging the cell while inserting the electrode. In contrast, the extracellular recording technique involves measurements with the electrode on the surface of the cell with respect to extracellular medium as a ground: extracellular APs (EAPs) are measured without penetration of the cell. Because voltage on the surface rather than across the membrane is now recorded, the magnitude of the EAP is much lower than the intracellular one. The shape of the EAP is also different and usually has a bi- or triphasic waveform due to the recording procedure depending on a position of the ground electrode and a size of the external bath (Pine, 1980; Gold *et al.*, 2006; Ghitani *et al.*, 2017). In the case of a large bath with the ground located at its border (Figure 2.10a), the EAP shape is tripolar. The reason is that at the point where the AP is initiated, there is a current sink into the axon, so current has to flow out further along the axon, including the place where the recording electrode is positioned. Therefore, positive change in the potential is recorded at this point. During the propagation, AP reaches the recording electrode and current starts to flow inside the axon there, so the negative voltage change can be recorded. Then, after the AP passes the electrode, there is an outflow of the current and positive change is recorded again (Figure 2.10a) (Johnston & Wu, 1995). Bipolar EAP waveform originated from the small size of the surrounding bath (insulation) and the position of the ground electrode at one of its ends. In this case, the external current

is able to flow only in one direction towards the ground leading to disappearance of one of the EAP poles (Figure 2.10b).

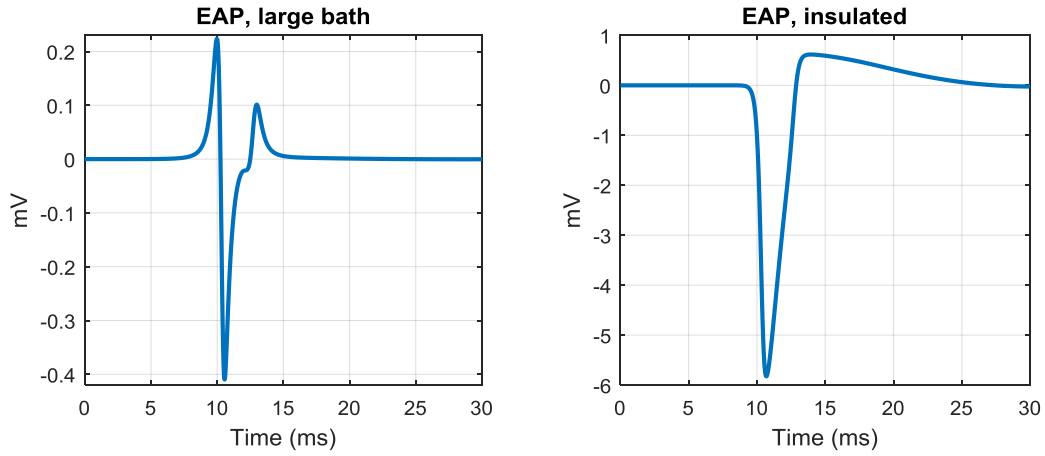

(a) (b)

Figure 2.10 Extracellular action potentials (EAPs) of the giant axon of the squid simulated with COMSOL Multiphysics using the HH model (Hodgkin & Huxley, 1952).
(a) Recoding was carried out in the large bath with respect to the ground electrode located at its border; (b) Recoding was done in the insulated cylinder of a small diameter relative to the ground electrode located at the end of a long fibre, as in the Chapters 3 and 4.

It is usually assumed that EAPs do not contain useful information and were mainly used to find out if the neuron has been excited or to distinguish between different classes of neurons (Mountcastle *et al.*, 1969; Csicsvari *et al.*, 1999). However, accurately recorded or modelled EAPs were shown to have highly variable waveforms depending on composition of ionic currents and location of the electrodes (Henze *et al.*, 2000; Gold *et al.*, 2006).

Finally, the aggregate AP of the whole nerve consisting of many fibres recorded with extracellular electrodes placed on its surface is known as a compound action potential (CAP) (Figure 2.11). Because a nerve usually consists of fibres of various diameters, individual EAPs' velocities are different, leading to the increase in the duration and decrease in the amplitude compared to individual EAPs (Freeman, 1972; Olney *et al.*, 1987). The size and duration of CAPs usually depend on the strength of the applied stimulus: larger stimulus excites more fibres in the nerve until all the fibres are recruited.

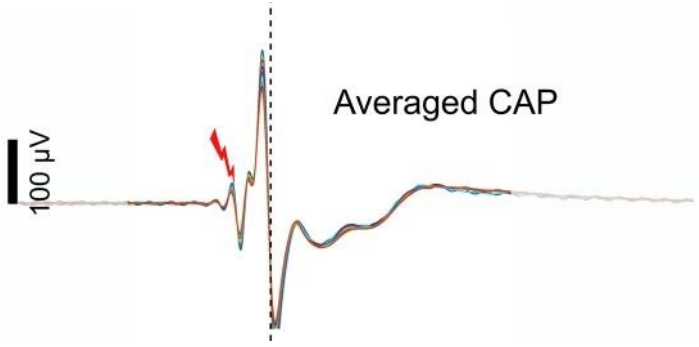

Figure 2.11 Compound action potentials (CAPs) recorded from the sciatic nerve of the rat. The figure is adapted from (Aristovich *et al.*, 2018).

2.2.5 Dispersion in nerves

Due to variability in sizes of fibres in nerves and proportionality of conduction velocity to the fibre diameter (Waxman, 1980), propagation velocities of individual fibres vary. As a result, the amplitude of the CAP being an aggregate sum of all individual APs decreases along the nerve following its initiation; this is commonly defined as temporal dispersion (Freeman, 1972; Dorfman, 1984; Olney *et al.*, 1987; Taylor, 1993; Schulte-Mattler *et al.*, 2001) (Figure 2.12).

Dispersion has mainly been studied in peripheral nerves consisting of mainly large myelinated fibres because they produce signals of higher magnitudes and possess lower stimulation thresholds (Hallin & Torebjörk, 1973; Torebjo¨rk & Hallin, 1974). For example, there was a 36% reduction in the CAP when stimulating the human ulnar nerve at above-elbow and wrist regions and recording at the fifth digit (Olney *et al.*, 1987). In (Taylor, 1993) and (Schulte-Mattler *et al.*, 2001), large human peripheral nerves including median, ulnar, common peroneal and tibial were stimulated and compound motor APs were recorded a few tens of cm away from the stimulus. These studies showed only a small amplitude and area decay which were in the range of 5-45% per meter of nerve length. In contrast, the effect of dispersion is much greater in small diameter unmyelinated nerves. In the olfactory nerve of the cat (Freeman, 1972) which comprises mainly small unmyelinated fibres 0.1 – 0.5 μm in diameter, CAPs could not be recorded further than 2.5 mm from the stimulation site. In vagal C fibres

in the mouse, there was a > 50% decrease at 4 mm from the point of activation (Chang *et al.*, 2015).

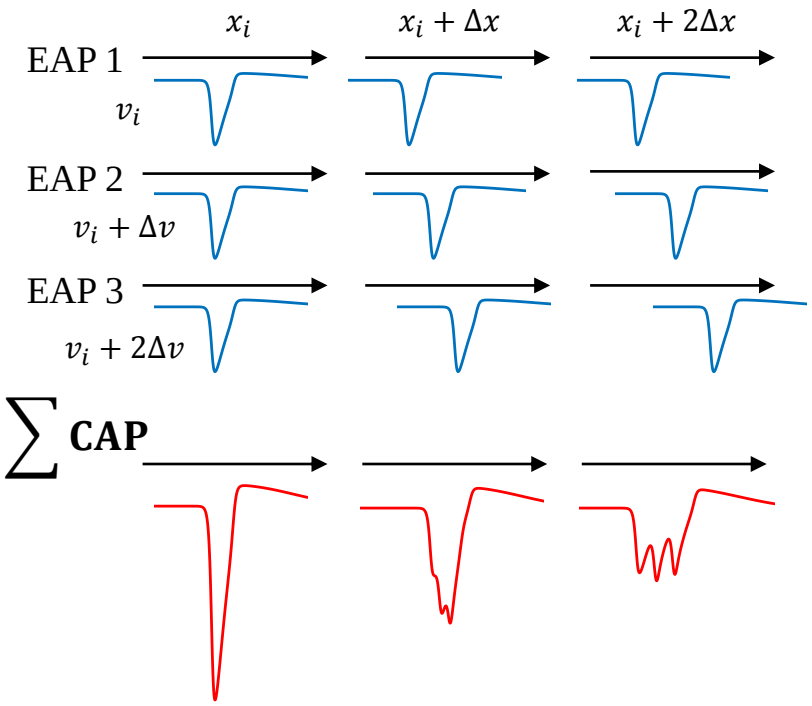

Figure 2.12 Schematic representation of dispersion of the CAP formed from three single EAPs of the giant squid axon (Hodgkin & Huxley, 1952) with slightly different conduction velocities simulated in COMSOL Multiphysics (Figure 2.10b).
In each fibre, the AP propagates with constant velocity v_i, $v_i+\Delta v$ or $v_i+2\Delta v$. The compound AP equals to the sum of EAPs of these single fibres; its amplitude decreases with distance x from stimulation.

2.3 Nerve fibre modelling

There are many neuronal models which have been developed since 1950s; most of them utilise a cable principle to simulate an AP propagation.

2.3.1 Neuronal cable model

The basic method for mathematical description of excitation and its conduction in the nerve tissue is the cable model (Cole & Curtis, 1938; Hodgkin & Rushton, 1946). In the passive cable model, the membrane is represented as a constant resistance and

a capacitance connected in parallel (Figure 2.3a). The capacitance comes from the thin lipid bilayer which is able to store charge. The resistance representing ion channels is voltage-independent, and it takes on two fixed values when they are opened and closed. It means that when ion channels change their state, there is an instantaneous drastic change in resistance, and this does not fully correspond to the realistic experimental behaviour of nerve fibres (Hodgkin & Huxley, 1952; Scriven, 1981; Cross & Robertson, 2016). In contrast, more accurate active cable model includes resistances which depend on the voltages across the membrane so that their state is actively changing during membrane activity (Figure 2.3b).

In the cable model, the longitudinal resistances are connected in series inside and outside of the fibre (Figure 2.3) allowing to simulate propagation of excitation along it. This principle can be used for simulation of AP conduction in both passive and active models with constant or voltage-dependent membrane resistance (Figure 2.3a and b).

The equation for description of the membrane current in the passive cable model can be derived by application of Ohm's and Kirchhoff's laws to the circuit in Figure 2.3a:

$$\frac{1}{R_{int} + R_{ext}} \frac{d^2 V_m}{dx^2} = C \frac{dV_m}{dt} + \frac{V_m}{R_m} \tag{2.12}$$

where R_{int} and R_{ext} are the axial intracellular and extracellular resistances, $[\Omega/m]$; R_m is the membrane resistance, $[\Omega \cdot m]$; V_m and C are membrane potential, $[V]$ and capacitance, $[F/m]$.

The cable model has two assumptions. First, the potential difference across the axon should be negligible compared to the one along it. This assumption is valid for long axons with small diameters located far enough from the stimulation electrodes, at the distance of at least five diameters of the fibre (Schnabel & Struijk, 2001). The second assumption demands conductivity to be uniform along the axon. It means that the ratio of the cytoplasm resistivity to cross sectional area must not change, or in other words, the diameter of the axon should be constant (Finn & LoPresti, 2002).

The passive cable model has been developed and utilised by many researchers for various applications (Hodgkin & Rushton, 1946; Durand, 1984; Basser, 1993) as well as our group at UCL for optimisation of EIT (Liston *et al.*, 2012). However, the latter model has not shown itself to be reliable in validation of the recent experimental data regarding the relationship of dZ with external parameters (Aristovich *et al.*, 2015, 2018). This led us to consideration of models with active properties.

2.3.2 Models of unmyelinated nerve fibres

Two main types of formalisms may be used to model active nervous tissue: Hodgkin-Huxley and Markovian (Strassberg & DeFelice, 1993; Clancy & Rudy, 1999). The Markovian formalism implies probabilistic behaviour of ion channels in the membrane, where each channel occupies certain state and the transition between states is described by a system of differential equations. This approach is good for modelling the behaviour of single ion channels but too computationally heavy to simulate the macroscopic properties of the whole fibre and particularly multiple fibres. For this purpose, there is a different type of formalism, called Hodgkin-Huxley formalism, which treats ion channels as populations controlled by gating variables. There are many models created using the Hodgkin-Huxley formalism, all based on the Hodgkin-Huxley model of the giant axon of the squid (HH model) (Hodgkin & Huxley, 1952).

Hodgkin-Huxley (HH) model

The HH model contains active ion channels and simulates the electrical behaviour of the axon of giant squid – very large unmyelinated axon with the diameter of 1 mm. The size of the axon gave the authors experimental advantage to insert two electrodes into the intracellular space. It made possible to use the voltage clamp (Figure 2.8) for obtaining the experimental data which they analysed to develop the final model.

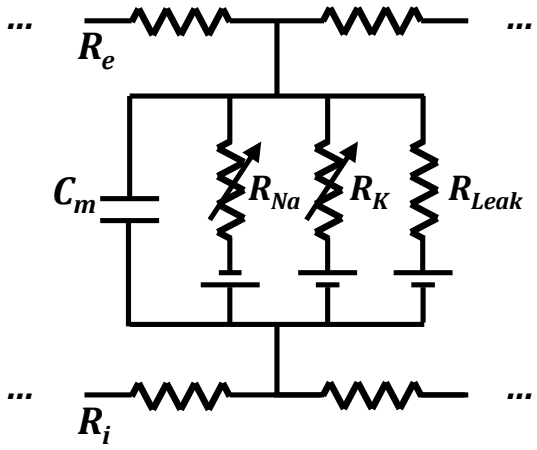

Figure 2.13 Element of the membrane circuit in the HH model of the giant axon of the squid. R_e and R_i designate extracellular and intracellular longitudinal resistances, C_m is the capacitance of the lipid bilayer, batteries represent the ionic electrochemical gradients which can be described by the Nernst equation (2.9).

The HH model represents the membrane as the electrical network which includes parallel-connected capacitance of lipid bilayer and the resistance of ion channels. Unlike the passive model, the resistance in HH model is variable and depends on the voltage across the membrane (Figure 2.13).

The model is described by a system of differential equations where the coefficients were selected so that the response of the membrane to electrical stimulation was as close to experimental as possible. The currents through ion channels are controlled by gating variables possessing values from 0 to 1; states of ion channels can continuously vary depending on the values of these variables. Propagation of APs can be described with the use of cable theory, the same as in the passive model (Figure 2.3, eq. (2.12)).

The system of Hodgkin-Huxley equations extended by the inclusion of propagation term is presented below. The first equation describing the flow of electric current through the membrane and along the axon was derived from Ohm's and Kirchhoff's laws, the same as equation (2.12). In (2.13), the intracellular and membrane resistances as well as the membrane capacitance are replaced by specific resistivities (or conductivities) and specific capacitance so that they are independent from the axon geometry.

$$\begin{aligned}
&\frac{r_{ax}}{2\rho_i}\frac{d^2V_m}{dx^2} = c_m\frac{dV_m}{dt} + \sum I_{ion}(V_m)\,;\\
&\sum I_{ion}(V_m) = \bar{g}_K n^4(V_m - V_K) + \bar{g}_{Na} m^3 h(V_m - V_{Na})\\
&\qquad\qquad + g_{Leak}(V_m - V_L);\\
&\frac{dn}{dt} = k\cdot(\alpha_n(1-n) - \beta_n n);\\
&\frac{dm}{dt} = k\cdot(\alpha_m(1-m) - \beta_m m);\\
&\frac{dh}{dt} = k\cdot(\alpha_h(1-h) - \beta_h h).
\end{aligned} \tag{2.13}$$

In the system, V_m and c_m are membrane potential, $[mV]$ and specific capacitance, $[\mu F/cm^2]$; r_{ax} is the radius of the axon, $[cm]$; ρ_i is the resistivity of the axoplasm, $[k\Omega\cdot cm]$; $\sum I_{ion}(V_m)$ is the sum of ionic currents through the membrane; $\bar{g}_K, \bar{g}_{Na}$ and $\bar{g}_{Leak}$ denote maximal conductances of potassium, sodium and leakage channels respectively, $[mS/\,cm^2]$; V_K, V_K and $V_L$are reversal potentials of corresponding ions, in $[mV]$, calculated with the Nernst equation (eq. (2.9)). n, m and h are gating variables controlling the fraction of ion channels in opened or closed state. Gating variables are governed by first-order kinetics with coefficients $\alpha_x = \alpha_x(V)$ and $\beta_x = \beta_x(V)$ experimentally obtained by Hodgkin and Huxley (Hodgkin & Huxley, 1952); they were:

$$\begin{aligned}
&\alpha_m = 0.1(35 + V_m)/\left(1 - e^{-0.1(35+V_m)}\right)\\
&\beta_m = 4e^{-(60+V_m)/18}\\
&\alpha_n = 0.01(50 + V_m)/\left(1 - e^{-0.1(50+V_m)}\right)\\
&\beta_n = 0.125e^{-(60+V_m)/80}\\
&\alpha_h = 0.07e^{-(60+V_m)/20}\\
&\beta_h = 1/\left(1 + e^{-0.1(30+V_m)}\right)
\end{aligned} \tag{2.14}$$

Coefficient *k* explains temperature dependence of the model:

$$k = Q_{10}^{\frac{T-T_0}{10}} \tag{2.15}$$

where Q_{10} was set to 3 and T_0 = 6.3ºC (Hodgkin & Huxley, 1952; Fitzhugh, 1966).

With the HH model, all the basic properties of the membrane temporal behaviour can be simulated. The model is fairly accurate, comparatively simple and quick to compute, therefore, the model itself and its modifications are still being extensively used in the current scientific research (Tigerholm *et al.*, 2014; Sundt *et al.*, 2015; Hope *et al.*, 2018; Sadleir *et al.*, 2019).

Complex active models of unmyelinated fibres

Since the basic Hodgkin-Huxley model is insufficient to describe all the details accompanying excitation in mammalian nerve fibres, new models of unmyelinated axons have been developed. Their complexity increased by the addition of more ion channels and tweaking the parameters so that they better correlate with the experimental data. These models steadily improved the accuracy of simulation of the APs' shape, excitability thresholds' temporal behaviour and its different complex features like activity dependent slowing (Thalhammer *et al.*, 1994) and recovery cycles (Kiernan *et al.*, 1996). For example, Scriven simulated repetitive firing phenomena by modelling the Na-K pump, finite intra-axonal and periaxonal volumes and calcium ion channels (Scriven, 1981); Herzog and colleagues first included TTX resistant sodium channels (now called Nav1.9) in a model of DRG neurons (Herzog et al., 2001); Tigerholm together with his group were able to model activity-dependent slowing and recovery cycles for C-nociceptors (Tigerholm et al., 2014); Cross and Robertson studied ionic mechanisms accompanying high-frequency firing of the descending contralateral movement detector axons (Cross & Robertson, 2016). Numerous other neural models have been developed in recent years, including for myelinated fibres (Jihwan Woo et al., 2009; Howells et al., 2012) and for groups of fibres (Qiao & Yoshida, 2013; Yin *et al.*, 2013; Pelot *et al.*, 2017).

2.3.3 Models of myelinated fibres

In the first active models of myelinated fibres, the HH equations (2.13)–(2.15) were applied at the nodes and the myelin sheath was simulated as a perfect insulator

(Fitzhugh, 1962) or as a constant resistor (Goldman & Albus, 1968). To better replicate experimental data, and since the ion channels utilized in the HH model could predict only basic behaviour of the membrane, new models started to appear possessing more complex ion channels and finer excitability properties (McNeal, 1976; Warman *et al.*, 1992) as well as with the addition of active ion channels in internodal segments (Bostock *et al.*, 1991; Stephanova & Bostock, 1995; Howells *et al.*, 2012).

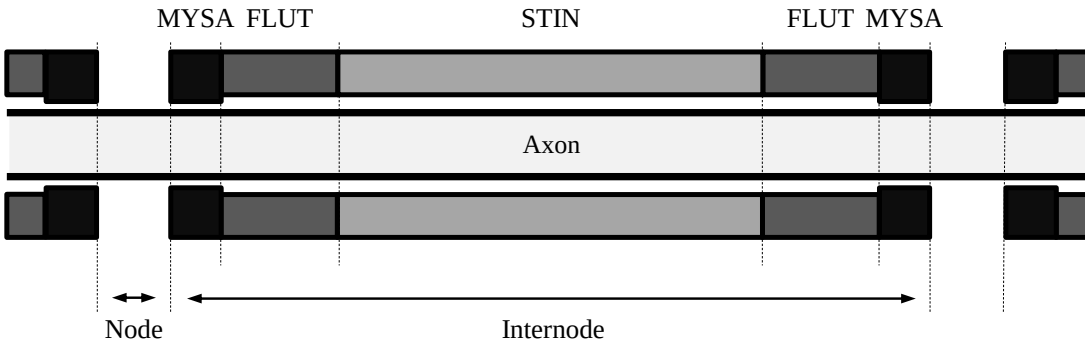

Figure 2.14 Simplified schematic representation of the myelinated fibre.
The scheme is based on the electron microscopy study (Berthold & Rydmark, 1983) in the myelinated spinal root fibre of the cat. Internodal sections are designated by myelin attachment (MYSA), fluted (FLUT) and stereotyped internodal (STIN) sections discussed in the text.

In addition to ion channels, the spatial structure of the nerve fibre was also revealed to play an important role in the accurate simulation of its excitability properties and shape of nodal and internodal transmembrane potentials.

The longitudinal structure of the modelled myelinated fibres has been developing from a simple classic cable (McNeal, 1976) to the novel paradigm where signals propagated along two parallel cables including axolemma and periaxonal space (Figure 2.14, Figure 2.15). Such a structure allowed simultaneous simulation of the transmembrane and transmyelin potentials for accurate description of the signals originating in the fibre.

The double-cable structure is based on the accurate myelinated fibre morphology obtained using electron microscopy of the paranode-node-paranode region of the spinal root fibre of the cat (Berthold & Rydmark, 1983) (Figure 2.14). This study demonstrated existence of a thin interspace (<5 nm) located between the axon and the

myelin sheath forming an additional current pathway along the fibre. As a result, the excitation is able to conduct in parallel along the axoplasm and the periaxonal space.

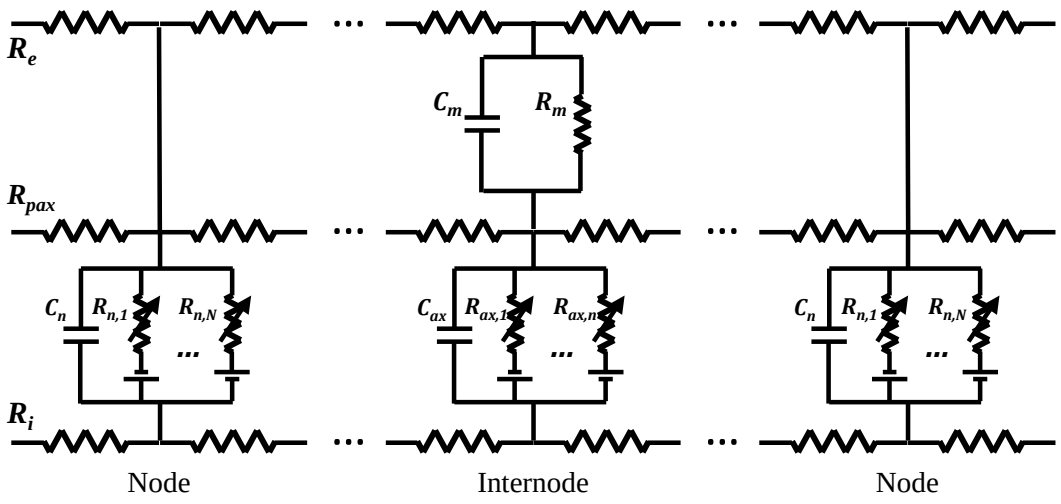

Figure 2.15 Circuit diagram of the double cable model of the myelinated fibre.
The fibre is represented as two parallel cables of the axon (R_i) and the periaxonal space (R_{pax}) between the axon and the myelin sheath; an external space (R_e) may be presented as a third cable.
Internodal section is depicted as a union of myelin attachment (MYSA), fluted (FLUT) and stereotyped internodal (STIN) sections; their description is given in Figure 2.14 and in the text. Nodal and internodal membranes as well as myelin are represented by parallel capacitance and resistance(s); equations describing the diagram can be derived from Ohm's and Kirchhoff's laws (eq. (2.16) - (2.18)).

The same study (Berthold & Rydmark, 1983) described finer morphological properties of the myelinated fibre (Figure 2.14): in addition to the short (~1 μm) node of Ranvier, the internodal section can be extended into three subsections including myelin sheath attachment (MYSA), fluted (FLUT) and stereotyped internodal (STIN) segments. MYSA is the short (3-4 μm) section describing the attachment of the myelin sheath to the axon. In this section, the width of the periaxonal space is smaller thus increasing its resistance forming a so-called paranodal seal between the axon and the myelin. FLUT is the fluted region (70 μm) which is usually combined with the adjacent main internodal STIN section (~ 1400 μm).

The double-cable structure was first utilised for modelling by Blight (Blight, 1985) and has subsequently been used in various studies (Halter & Clark, 1991; Stephanova & Bostock, 1995; McIntyre *et al.*, 2002; Dimitrov, 2009; Hope *et al.*, 2018).

Description of the double-cable circuit (Figure 2.15) may be given by application of Ohm's and Kirchhoff's laws (Stephanova & Bostock, 1996). At the node:

$$\frac{1}{R_i}\frac{\partial^2 V_{ax}}{\partial x^2} = C_n\frac{dV_{ax}}{dt} + \sum_{node} I_{ion}(V_{ax}) \tag{2.16}$$

where $\sum_{node} I_{ion}(V_{ax})$ designate all ionic currents at the nodal membrane, $[A]$; R_i is the axial intracellular resistance, $[\Omega/m]$; V_{ax} and C_n are transaxonal membrane potential, $[V]$ and capacitance of the axonal membrane, $[F/m]$.

At the internodal axolemma (MYSA, FLUT and STIN combined):

$$\frac{1}{R_i}\left(\frac{\partial^2 V_{ax}}{\partial x^2} + \frac{\partial^2 V_m}{\partial x^2}\right) = C_{ax}\frac{dV_{ax}}{dt} + \sum_{Int} I_{ion}(V_{ax}) \tag{2.17}$$

In the equation, $\sum_{Int} I_{ion}(V_{ax})$ designate all ionic currents at the internodal membrane, $[A]$; R_i is the axial intracellular resistance, $[\Omega/m]$; V_{ax} and V_m are transaxonal and transmyelin membrane potentials, $[V]$; C_{ax} is the axonal membrane capacitance, $[F/m]$.

At the periaxonal space, the circuit equation becomes:

$$\frac{1}{R_i}\left(\frac{\partial^2 V_{ax}}{\partial x^2} + \frac{\partial^2 V_m}{\partial x^2}\right) + \frac{1}{R_{pax}}\frac{\partial^2 V_m}{\partial x^2} = C_m\frac{dV_m}{dt} + \frac{V_m}{R_m} \tag{2.18}$$

where R_i and R_{pax} are the axial resistances of intracellular and periaxonal space, $[\Omega/m]$; R_m is the myelin resistance, $[\Omega \cdot m]$; V_{ax} and V_m are transaxonal and trynsmyelin membrane potentials, $[V]$; C_m is the capacitance of the myelin sheath, $[F/m]$.

In the new models, incorporation of the discussed fine structural features, such as paranodal seal, conducting periaxonal space and multi-layered myelin sheath, were shown to be essential in replication of various excitation properties of the fibre such as the depolarizing afterpotentials or the realistic spatial distribution of AP during conduction (Stephanova & Bostock, 1995; Stephanova, 2001; McIntyre *et al.*, 2002).

2.3.4 Coupling of the models with extracellular space

Communication between two models via transmission of their output values from one model to another is referred to as coupling. Coupling of the nerve fibre model with extracellular space can be implemented in one direction (unidirectional coupling) or in two directions (bidirectional coupling) (Figure 2.16). First, for stimulation of the fibre with external electrodes, the electrical field computed in the extracellular space must be passed to the model of the fibre. Second, to externally record extracellular APs, the membrane currents from the model of the fibre must be passed into the external space.

Unidirectional coupling was implemented in various studies described below, however, there are no models to date allowing continuous simultaneous coupling in both directions.

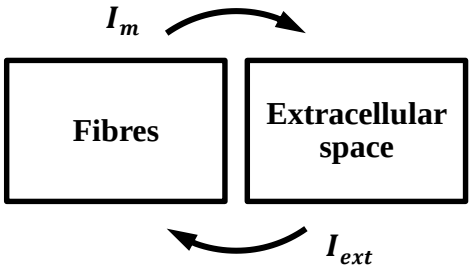

Figure 2.16 Principle of bi-directional coupling the membrane with the extracellular space. Membrane currents I_m are passed from the fibre into the external space simultaneously with passing the externally applied currents I_{ext} into the fibre.

1. Simulation of extracellular action potentials

For simulation of AP propagation along the axon in the extracellular space (or EAPs), the electrical field distribution formed as a result of passing the membrane currents from the fibre into this space must be computed. The physics behind it is governed by Maxwell's equations:

$$\nabla \cdot \boldsymbol{E} = \frac{\rho}{\varepsilon_0} \tag{2.19}$$

$$\nabla \times \boldsymbol{E} = -\frac{\partial \boldsymbol{B}}{\partial t}$$

$$\nabla \times \boldsymbol{B} = \mu_0 \boldsymbol{J} + \mu_0 \varepsilon_0 \frac{\partial \boldsymbol{E}}{\partial t}$$

In the equations, $\boldsymbol{E}$ and $\boldsymbol{B}$ are the electric and magnetic fields, $[V/m]$ and $[T]$; $\boldsymbol{J}$ is the current density $[A/m^2]$, ρ is the charge density, $[C/m^3]$; ε_0 and μ_0 are the electric and magnetic constants.

Taking the divergence of the last equation in (2.19) (Ampere's law) and combining with the first equation (Gauss's law) leads to the continuity equation:

$$\nabla \cdot \boldsymbol{J} + \frac{\partial \rho}{\partial t} = 0 \tag{2.20}$$

In the absence of electric sources and sinks $\partial\rho/\partial t = 0$, and therefore $\nabla \cdot \boldsymbol{J} = \mathbf{0}$**.** Together with Ohm's law $\boldsymbol{J} = (\sigma + \boldsymbol{j}\omega\epsilon)\boldsymbol{E}$**,** where σ and ϵ are the conductivity $[S/m]$ and permittivity $[F/m]$ of the medium, ω is the angular frequency, it becomes:

$$\nabla \cdot ((\sigma + \boldsymbol{j}\omega\epsilon)\boldsymbol{E}) = \mathbf{0} \tag{2.21}$$

Consideration of low-frequency currents only, which is usually the case in EIT at up to 1 MHz (Lionheart et al., 2004; Soni et al., 2006), leads to $\partial\boldsymbol{B}/\partial t = 0$ and the third equation in (2.19) (Faraday's law) becomes $\nabla \times \boldsymbol{E} = \mathbf{0}$. Therefore, electric field is conservative and can be represented as a gradient of the electric potential $\boldsymbol{E} = -\nabla \mathrm{V}$.

The analysis of the quasi-static approximation of Maxwell's equations applied for signals generated by excitable cells (Plonsey & Heppner, 1967) as well as for neural stimulation at frequencies up to 100 kHz (Bossetti *et al.*, 2008) has shown that the capacitive effects introduced by the term $\boldsymbol{j}\omega\epsilon$ do not significantly affect the output of the simulations. Therefore, this term can be neglected and the equation (2.21) thus transforms to the Laplace's equation in the volume V:

$$-\nabla \cdot (\sigma \nabla V) = 0 \tag{2.22}$$

Joined with the equations describing ionic currents, like HH (2.13) or more complex ones (McIntyre *et al.*, 2002; Tigerholm *et al.*, 2014; Sundt *et al.*, 2015), the Laplace's equation allows simulation of the AP propagation in both intracellular and extracellular spaces. For this, the membrane current applied to the boundary of the fibre Γ can be written as:

$$I_m|_\Gamma = \sigma_e \nabla V_e \cdot \boldsymbol{n} = C_m \frac{dV_m}{dt} + \sum I_{ion}(V_m)\,, \text{ on } \Gamma_m \tag{2.23}$$

where σ_e and V_e are conductivity, $\left[\frac{S}{m}\right]$ and electric potential, $[mV]$ of the extracellular space, Γ is the axonal boundary and $\boldsymbol{n}$ is the outward unit normal vector to it; the expression on the right designates the sum of the capacitive and ionic membrane currents of the nerve fibre, as in (2.12) or (2.13).

The discussed general approach has previously been widely used for simulation of APs in the extracellular space (Holt & Koch, 1999; Martinek *et al.*, 2008; Wang *et al.*, 2018; Pelot *et al.*, 2019).

Equations (2.22) and (2.23) can be solved numerically using discretization methods such as finite difference method (FDM), finite volume method (FVM) and finite element method (FEM). FDM approximates the differential equations as differences using regular grids, so the solution can be very efficient; however, this method has difficulties dealing with complex geometries (Smith, 1985). FVM and FEM are more general methods allowing to discretize the geometry into unstructured parts so that equations representing the system are reformulated and solved in each of these parts. FVM is a conservative method which utilises the equality of fluxes in the neighbouring elements and uses piecewise constant functions to approximate the solution (Eymard *et al.*, 2000). FEM is a more powerful method which can use continuous approximating functions of any order and may be applied for simulation of majority of physical phenomena (Pepper, 2017).

Simplification of external field calculation for the case of isotropic extracellular medium has recently been introduced; it is called line source approximation (LSA) (Holt & Koch, 1999; Gold *et al.*, 2006; Lubba *et al.*, 2019). The idea is representation of the nerve fibre as a set of point sources and computation of the electric potential as the sum of the potentials of from all the points, instead of explicitly solving Laplace's equation (2.22). LSA has shown itself accurate in EAPs simulation at distances larger than radius of the fibre (Holt, 1998); however, it requires the fibre to be separated from other sources in the medium which cannot be fulfilled in EIT where alternating currents interacting with the fibre are applied by means of external electrodes.

2. External stimulation of nerve fibres

Stimulation of nervous tissue with external electrodes has previously been implemented in various modelling studies (McNeal, 1976; Rattay, 1989; Greenberg *et al.*, 1999; Raspopovic *et al.*, 2011). The general approach utilised for this purpose was inclusion of an activating function (Rattay, 1999) into the equations for membrane currents (2.12) or (2.13). For a long homogeneous fibre with a constant diameter, the activating function can be written as:

$$f(x,t) = \frac{1}{C_m \cdot R_i} \frac{d^2 V_e(x,t)}{dx^2} \tag{2.24}$$

where V_e is the extracellular potential in $[mV]$, C_m as the membrane capacitance in $[F/m]$, R_i is the axial intracellular resistance, $[\Omega/m]$, which for the homogeneous fibre with constant radius r_{ax} can be transferred into specific capacitance c_m $[F/m^2]$ and resistivity ρ_i $[\Omega \cdot m]$ used in (2.13) as $c_m = C_m/2\pi r_{ax}$ and $\rho_i = \pi r_{ax}^2 \cdot R_i$.

With inclusion of the activating function into the equation describing the temporal behaviour of the membrane in the HH model (2.13), it can be rewritten as:

$$\frac{r_{ax}}{2\rho_i}\left(\frac{d^2 V_m(x,t)}{dx^2} + \frac{d^2 V_e(x,t)}{dx^2}\right) = c_m \frac{dV_m}{dt} + \sum I_{ion}(V_m) \tag{2.25}$$

The activating function can be easily derived by applying Ohm's and Kirchhoff's laws to the HH circuit (Figure 2.13) taking extracellular potential R_e into consideration. The same can be done for any nerve fibre circuit of this type (Figure 2.3, Figure 2.15).

For the general case of any fibre, the activating function can be written as:

$$f(x,t) = \frac{1}{C_m}\left[\frac{V_{e,n-1} - V_{e,n}}{R_{n-1}/2 + R_n/2} + \frac{V_{e,n+1} - V_{e,n}}{R_{n+1}/2 + R_n/2}\right] \tag{2.26}$$

where $V_{e,n}$ and R_n are the extracellular potential and axial intracellular resistance at the compartment *n* of the fibre.

The concept of activating function can be applied for modelling stimulation any nerve fibre whose membrane currents are governed by the HH-type equations, such as (2.12), (2.13) or (2.16) – (2.18).

Chapter 3
Model of impedance change in unmyelinated nerve fibres

3.1 Introduction

3.1.1 Overview

Fast neural EIT has been successful in imaging electrically evoked fascicular activity of the largest myelinated fibres in rat sciatic nerve (Aristovich *et al.*, 2018) and recurrent laryngeal nerve of the sheep (Chapman *et al.*, 2019). In order to extend fast neural EIT to work in small autonomic nerves containing mostly unmyelinated, slow-conducting fibres with a smaller impedance response, EIT parameters require optimisation. These parameters include optimal strength and frequency of injected current as well as electrodes position and geometry. Also, thorough validation of experimental recordings has to be performed in order to understand consequences of the underlying interaction between applied current and dynamic conduction of action potentials. This was not possible with the previously developed passive model (Liston *et al.*, 2012) which was not fully supported by experimental data (Aristovich *et al.*, 2015, 2018; Vongerichten, 2015; Faulkner *et al.*, 2018*b*).

Currently, there is no model able to accurately and simultaneously simulate both intracellular and extracellular electric fields in 3D for interacting active fibres. Ideally, the model would contain thousands of closely packed active unmyelinated and myelinated interacting fibres with varied sizes, propagation velocities and ion channel

properties. This chapter addresses the gap by developing the first building block of such a complete model via introducing models of single and multiple unmyelinated fibres with their accurately simulated external and internal electric fields. Various parameters affecting these models were studied including electrodes position, injected current and fibre complexity. The resulting models enable the experimental data previously obtained for an unmyelinated crab leg nerve (Holder, 1992; Boone, 1995; Gilad *et al.*, 2009; Oh *et al.*, 2011) to be interpreted and give preliminary values for optimal parameters of EIT in unmyelinated nerves.

3.1.2 Purpose

The overall purpose of the work presented in this chapter was to develop models of single and multiple unmyelinated nerve fibres and evaluate how impedance changes across them during the action potential. This was evaluated in models of one, two, four and eight interacting squid giant axons with Hodgkin-Huxley ion channels and a single C fibre with mammalian nociceptor ion channels. Specific questions to be addressed were:

1. How does the impedance change (dZ) vary with experimental parameters? These include
    a. AC amplitude and frequency;
    b. size and position of the electrodes;
    c. number of fibres and interaction between them;
    d. model complexity;
2. Does this agree with the previous studies?
    a. Does the model confirm experimental recordings (Holder, 1992; Boone, 1995; Gilad *et al.*, 2009; Oh *et al.*, 2011; Aristovich *et al.*, 2015)?
    b. Does it offer any explanation?
    c. Does it differ from the previous modelling (Liston *et al.*, 2012)?
3. Which model options are recommended for further modelling studies?

3.1.3 Experimental design

The work was divided into the following steps:

1) A 3D FEM Hodgkin-Huxley model of the giant axon of the squid was developed in three-dimensional space. An action potential (AP) was induced at the distal end of the axon and its propagation was simulated intra- and extracellularly. An electric current was applied through two external ring electrodes and the axonal activity was measured by the identical electrode with respect to ground (Figure 3.1). The model was transformed into the equivalent 2D axisymmetric one to accelerate computations. The effects of varying experimental parameters on dZ were studied. This model became the basis for all further simulations.

2) Additional axons were added such that their extracellular APs (EAPs) influenced each other. The effects of increasing number of fibres and their interactions was studied with 2, 4 and 8-axonal nerves.

3) A full accurate 3D model of a mammalian C fibre (and corresponding 2D axisymmetric model) containing ten experimentally validated ion channels and variable concentrations of the ions inside and outside of the membrane was developed based on (Tigerholm *et al.*, 2014). Simulations were performed using the same parameters as the HH model. To study how dZ is affected by the complexity of ion channels and spatial structure of the model, the C fibre model was compared with a spatially modified HH model whose dimensions, fibre diameter and axoplasm resistivity were reduced to match the C fibre, while temporal properties matched those of the classic HH model.

4) The impedance changes simulated in the developed models were compared with the experimental data previously obtained in unmyelinated crab nerves.

3.2 Methods

3.2.1 General modelling principles

A model comprising a simultaneous simulation of electrical fields generated by nerve fibres and external sources in intra- and extracellular spaces was constructed using the finite element method (FEM) approach in COMSOL Multiphysics software (COMSOL Inc, USA). The finite element method implies the decomposition of the model geometry into separate parts so that element equations approximating the original ones are locally solved in each of the parts. These equations are then assembled into the global domain and solved there using initial conditions (Zienkiewicz *et al.*, 1977). With the use of FEM, COMSOL allows automation of the solution of partial differential equations (PDEs) describing neural tissue in temporal and spatial dimensions. In addition to FEM, other methods allowing spatial discretization for solving PDEs exist – these are finite difference and finite volume methods (FDM and FVM). Although these methods provide faster solution, they either cannot be applied to non-regular geometries (FDM) (Smith, 1985) or lack flexibility of using high-order continuous approximating functions (FVM) (Section 2.3.4) (Eymard *et al.*, 2000).

A simplification of the experimental design in the crab leg nerve with the 4-electrode impedance measurement paradigm was simulated (Aristovich *et al.*, 2015). In this experiment, an excised crab nerve was placed on a linear electrode array, action potentials were stimulated by 2 electrodes at the proximal end of the nerve, electric current was injected in the middle and voltages were measured with the electrode located before the injecting ones in respect to the one at the distal end of the nerve.

The geometry of the model consisted of extracellular space represented by a 3D cylinder with the electrical conductivity of an extracellular medium equalling 10 *mS/cm* (Figure 3.1a) (Elia & Lamberti, 2013). Axons were represented as 1D lines, so that the membrane and intracellular space were not treated separately. In the model, the full transfer impedance of the system "fibre + external space" (Z) was continuously

measured; this impedance changed during AP propagation (dZ). By injecting current and measuring external voltage the dZ modulating this voltage could be measured. Equations representing Z and dZ in terms of injected current and measured voltage are given in (2.7) of section 2.1.2 and extended below:

$$Z = \frac{|V|e^{j(\omega t+\varphi_V)}}{|I|e^{j(\omega t+\varphi_I)}} = |Z|e^{j(\varphi_V-\varphi_I)} \approx |Z| \tag{3.1}$$

In the equation, *Z, V* and *I* are complex values representing electrical impedance of the system, measured voltage and injected current, $|Z|$, $|V|$ and $|I|$ are their amplitudes; φ_V and φ_I are voltage and current phases, where the phase shift $\Delta\varphi = \varphi_V - \varphi_I \approx 0$ as the membrane does not significantly change the phase of the externally measured current (Cole & Curtis, 1939). However, the small phase shift may affect the measurements at high frequencies (*Results*, Figure 3.12).

Impedance change dZ is equal to the relative change of the impedance $Z(t_0)$ when AP passes under the electrodes with respect to the baseline impedance of the system $Z=Z(t)$. Using (3.1), the complex dZ and absolute $|dZ|$ can be expressed in terms of the measured voltages $V=V(t)$ and $V(t_0)$:

$$\begin{aligned} dZ &= \frac{Z(t) - Z(t_0)}{Z(t)} \\ &= \frac{|V(t)|e^{j\Delta\varphi} - |V(t_0)|e^{j\Delta\varphi_0}}{|V(t)|e^{j\Delta\varphi}} \approx \frac{|V(t)| - |V(t_0)|}{|V(t)|} = |dZ| \end{aligned} \tag{3.2}$$

Application of alternating current was simulated via two ring extracellular electrodes situated on the boundary of the cylinder (Figure 3.1):

$$I_{inj} = \pm I_{amp} \cdot sin(2\pi f t + \varphi) \tag{3.3}$$

where I_{amp} is an amplitude of the applied alternating current, it was expressed in the current density terms – $[\mu A/cm^2]$, f in $[kHz]$ and φ are its frequency and phase, time is in $[ms]$.

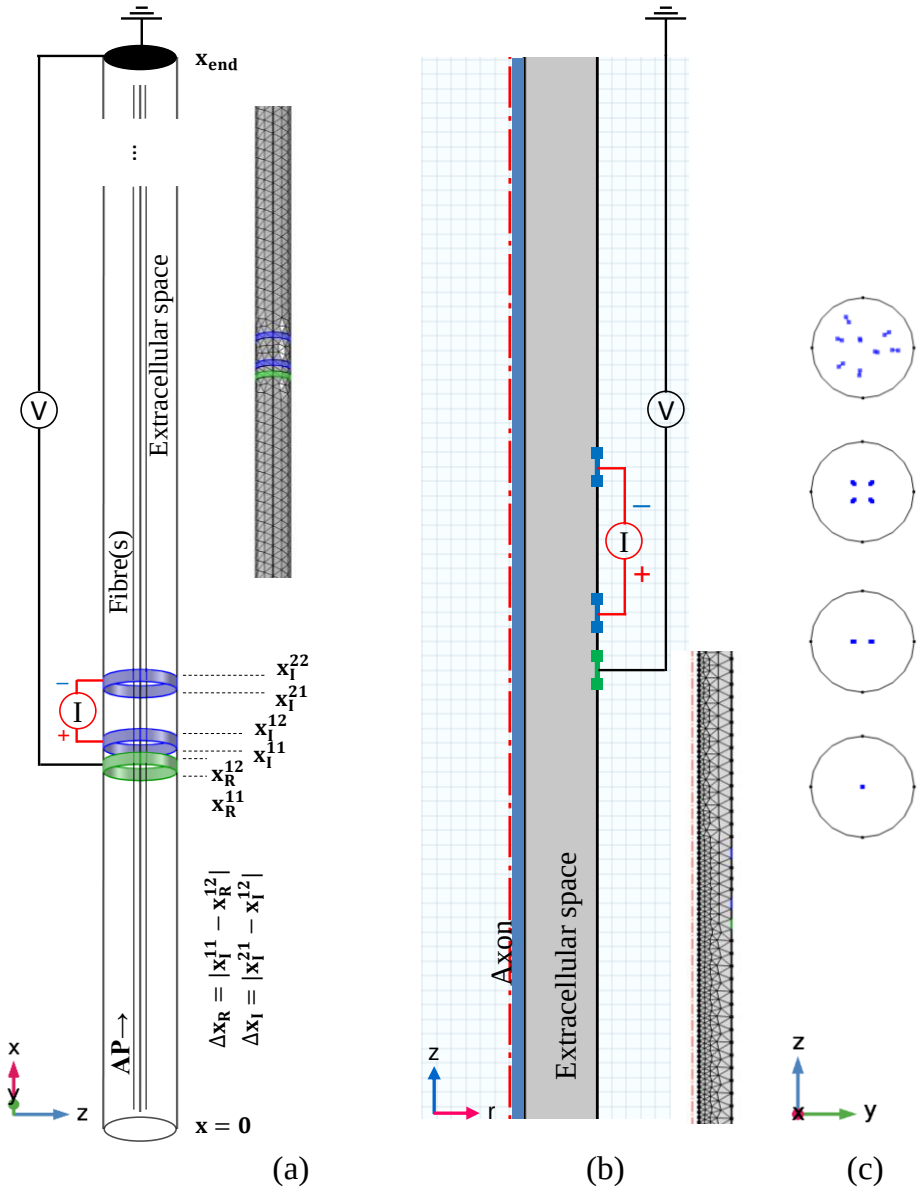

Figure 3.1 Geometrical structure of the developed unmyelinated fibre models and their FEM meshes. (a) The 3D geometry of the models and corresponding 3D FEM mesh. AP was induced from the end of the axon(s); DC or AC was applied through two external electrodes (blue); the electric field was recorded by an external electrode (green) placed before the injecting ones (with respect to ground). Coordinates along the fibre are represented by x with corresponding indices, for example x_R^{11} designates the position of the beginning of the recording electrode and x_I^{22} – the end of the second injecting electrode. Detailed models' geometric dimensions are given in the text (Table 3.2); (b) Equivalent 2D axisymmetric model with a single fibre and corresponding triangular FEM mesh; (c) Side view on the 1-, 2-, 4- and 8-axonal HH models. In the 8-axonal model, axons were uniformly distributed inside the cylinder.

In the model, APs were initiated at the end of the axons by bipolar stimulation. The compound activity was recorded by a recording electrode situated before the equally sized injecting electrodes with respect to ground (Figure 3.1). The model was grounded

at the distal end only to prevent the current from propagating along the fibre in the direction opposite to the AP and subsequently causing artefacts in dZ measurements (Aristovich *et al.*, 2015). The coupled feedback approach was utilized in the developed model so that the current injected through the external electrodes affected the fibres and the fibres' activity affected the external electric field recorded by the external electrode.

In the model, resistance of the external medium was constant (*0.1 kΩ·cm)* while the impedance of the fibre was variable and depended on the transmembrane voltage. A volume conduction Laplace's equation (2.22), equation defining activity of the axon subjected to external stimulation (2.25) and the equation describing their coupling with each other (2.23) were solved for each time step simultaneously with respect to membrane and external potentials V_m and V_e.

In mathematical terms, the resulting equations to be solved in the models were as follows (Figure 3.1):

$$-\nabla \cdot (\sigma \nabla V_e(x,y,z,t)) = 0 \tag{3.4}$$

$$\frac{r_{ax}}{2\rho_i}\left(\frac{d^2V_m(x,t)}{dx^2} + \frac{d^2V_e(x,y_{ax},z_{ax},t)}{dx^2}\right) = C_m\frac{dV_m(x,t)}{dt} + \sum I_{ion}(V_m(x,t)) \tag{3.5}$$

The first equation describes the volume conduction in the external space (2.22) and the second is for the fibre (2.25); y_{ax} and z_{ax} are y and z coordinates of the axon in the model (Figure 3.1). The composition of ionic currents depends on the model and will be explained further. Boundary conditions (BCs) on 1D axons in 3D space were ($y = y_{ax}$, $z = z_{ax}$; Figure 3.1a):

$$\begin{aligned} &x \in (0, x_{end}):\\ &-\nabla(\sigma_e \nabla V_e(x,y_{ax},z_{ax},t)) \cdot S_n = 2\pi r_{ax} \cdot \left(C_m\frac{dV_m(x,t)}{dt} + \sum I_{ion}\big(V_m(x,t)\big)\right) \end{aligned} \tag{3.6}$$

where r_{ax} is the radius of the axon, S_n is the unit surface area. All other variables are described in the previous sections of the thesis (eq. (2.23), (3.3)).

On the external cylinder ($y_0^2 + z_0^2 = R^2$, Figure 3.1a), BCs were:

$$\begin{aligned}
&x \in \left(0, x_{I_{11}}\right): \sigma_e \nabla V_e(x, y_0, z_0, t) \cdot \boldsymbol{n} = 0 \\
&x \in [x_{I_{11}}, x_{I_{12}}] : \sigma_e \nabla V_e(x, y_0, z_0, t) \cdot \boldsymbol{n} = +I_{amp} \cdot sin(2\pi f t + \varphi) \\
&x \in (x_{I_{12}}, x_{I_{21}}): \sigma_e \nabla V_e(x, y_0, z_0, t) \cdot \boldsymbol{n} = 0 \\
&x \in [x_{I_{21}}, x_{I_{22}}] : \sigma_e \nabla V_e(x, y_0, z_0, t) \cdot \boldsymbol{n} = -I_{amp} \cdot sin(2\pi f t + \varphi) \\
&x \in (x_{I_{22}}, x_{end}): \sigma_e \nabla V_e(x, y_0, z_0, t) \cdot \boldsymbol{n} = 0 \\
&x = 0, y, z \in (0, R): \sigma_e \nabla V_e(0, y, z, t) \cdot \boldsymbol{n} = 0 \\
&x = x_{end}, y, z \in (0, R): V_e(x_{end}, y, z, t) = 0
\end{aligned} \tag{3.7}$$

In the above equations, **n** is the inward unit normal vector to the surface of the outer cylinder, R is the radius of this cylinder. The initial conditions for the fibres depended on the model and are discussed further; the general condition in all developed models was $V_e(t = 0) = 0$.

A 3D tetrahedral mesh was constructed, and the fibres were divided at equal intervals so that they formed a continuous mesh within the volume. The length of these intervals and the size of the mesh elements close to the fibre depend on the model and must be much smaller for the C fibre than for the HH model. This is because the C fibre diameter is 10^3 times smaller, leading to the smaller space constant and associated AP characteristics. The number of elements also grows with additional fibres because many small elements appear between the adjacent fibres.

In all models, time stepping was implemented using the backward differentiation formula (BDF) with adaptive step size and variable order from 1 to 5. This method is implicit and known for its stability in the solution of stiff equations (Hindmarsh *et al.*, 2005). The corresponding systems of linear equations at each time step were solved in the spatial domain using a parallel sparse direct solver (PARDISO). PARDISO is used to solve systems of equations in the general form and allows efficient parallelization of the solution by the usage of multithreading (Schenk & Gärtner, 2004). Since PARDISO is the direct solver, convergence was tested by checking the approximate deviation of the obtained numerical solution from the exact solution. For this, the numerical solution was put back into the original equations at each time step so that

the relative difference between the resulting value and the obtained solution was found. If this relative difference, known as the residual, exceeded the specified tolerance – the time step was decreased. The relative tolerance depended on the model: it was set to 0.01 for the HH model and 0.001 for the C fibre model.

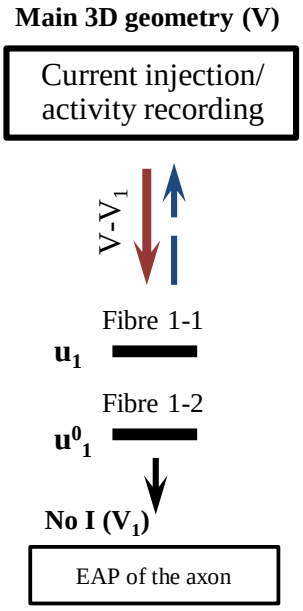

Figure 3.2 Schematic representation of the feedback coupling models' operation for a single fibre. Additional 3D geometry was to simulate electric field of the "pure" EAP with no injected current (V_1); at each time step, their difference with the main field (V, with injected current) was applied to the active fibre ($V-V_1$, red line) and resultant membrane current was coupled to the main 3D geometry (blue dashed line).

Using the same approach and the signal processing routine (3.2.5 *Signal processing*) as in the experiment (Aristovich *et al.*, 2015) together with the voltages obtained by solving the above equations, changes in the impedance Z of the system "fibre + external space" (*dZ*) were measured. As the main interest was in the electrical properties and corresponding impedance changes of the system as a whole, separate consideration of the membrane and the volume inside the fibre was omitted.

For an accurate simulation of the fibre and external volume conductor affecting each other, 1D and 3D problems corresponding to them had to be solved twice. Otherwise, the extracellular action potential modelled by coupling the transmembrane current from the fibre to the external space (2.23) would be coupled back into the fibre (2.25). That would mean that the fibre would be doubly affected by its own electric

field that is already implicitly included in the cable theory underlying AP propagation. Thus, the main 1D/3D pair (Figure 3.2, top) served for simulation of the fibre, current injection into it and external activity recording. The additional 1D/3D pair (Figure 3.2, bottom) did the same simulations but without injected current. The simulated external electric field in the adjoint 3D geometry (EAP with no current) was being subtracted from the compound activity in the first 3D geometry to be applied to the fibre at each simulation step ($V\text{-}V_1$ on Figure 3.2).

To accelerate computations of the single-fibre models without reducing their complexity, 3D models were transformed into the 2D ones with axial symmetry (Figure 3.1b). For this, spatial coordinates (*x*, *y*, *z*) were exchanged for the cylindrical ones (*r*, *z)*, the same was performed for the del operators. As a result, equation (3.4) was transformed into:

$$-\sigma \cdot \nabla_{rz}^2 V_e(r,z,t) = 0 \tag{3.8}$$

where Laplace operator has the form $\nabla_{rz}^2 = \frac{1}{r}\frac{\partial}{\partial r}\left(r\frac{\partial}{\partial r}\right) + \frac{\partial^2}{\partial z^2}$.

The BCs at the boundary of the external cylinder remained the same as in the 3D case (3.7), with the coordinates *x*, *y* exchanged for *r* and *x* exchanged for *z*:

$$\begin{aligned}
&z \in \left(0, z_{I_{11}}\right): \sigma_e \nabla V_e(R,z,t) \cdot \boldsymbol{n} = 0\\
&z \in [z_{I_{11}}, z_{I_{12}}] : \sigma_e \nabla V_e(R,z,t) \cdot \boldsymbol{n} = +I_{amp} \cdot sin(2\pi f t + \varphi)\\
&z \in (z_{I_{12}}, z_{I_{21}}): \sigma_e \nabla V_e(R,z,t) \cdot \boldsymbol{n} = 0\\
&z \in [z_{I_{21}}, z_{I_{22}}] : \sigma_e \nabla V_e(R,z,t) \cdot \boldsymbol{n} = -I_{amp} \cdot sin(2\pi f t + \varphi)\\
&z \in (z_{I_{22}}, z_{end}): \sigma_e \nabla V_e(R,z,t) \cdot \boldsymbol{n} = 0\\
&z = 0, r \in (r_{ax}, R): \sigma_e \nabla V_e(r,0,t) \cdot \boldsymbol{n} = 0\\
&z = z_{end}, r \in (r_{ax}, R): V_e(r, z_{end}, t) = 0
\end{aligned} \tag{3.9}$$

The BCs for the fibres (3.6) were reorganized into:

$$z \in (0, z_{end}):$$
$$\sigma_e \nabla V_e(r_{ax}, z, t) \cdot \boldsymbol{n} = C_m \frac{dV_m(z,t)}{dt} + \sum I_{ion}(V_m(z,t)), \; on \; \Gamma_m \tag{3.10}$$

where Γ_m is the boundary of the axon (Figure 3.1b), r_{ax} is the radius of the axon, **n** is the outward unit normal vector. The numerical schemes for solving the reduced models remained the same as for the original 3D models.

Unlike in the 3D model with 1-dimensional fibre, in the 2D model the fibre was represented as a cylinder which did not significantly affect the precision of simulations at the distances exceeding fibre diameter (*Results*, Figure 3.6). The model had a triangular FEM mesh which made the computations up to 10 times faster. The main disadvantage of this model is its lack of flexibility: multiple fibres and non-symmetric electrodes cannot be simulated.

3.2.2 FEM model of Hodgkin-Huxley squid giant axon

The system of four equations (2.13) describing the HH model is presented in section 2.3.2. Extension of the main circuit equation (first equation in (2.13)) with the activating function (2.24) originating from the application of the external field to the fibre, is shown below (3.11). The variables' definitions are provided in the literature review following (2.13) and (2.24).

$$\frac{r_{ax}}{2\rho_i}\left(\frac{d^2V_m}{dx^2} + \frac{d^2V_e}{dx^2}\right) = c_m \frac{dV_m}{dt} + \bar{g}_K n^4 (V_m - V_K) + \bar{g}_{Na} m^3 h (V_m - V_{Na}) + g_{Leak}(V_m - V_L) \tag{3.11}$$

In this model, six equations have been solved in total including the system of four equations consisting of (3.11) and gating variables from (2.13), external electric field (2.22) and coupling from 1D fibre to the surrounding volume (2.23). All the utilized boundary conditions are presented in equation (3.7). The main parameters and initial values of the model were chosen as in (Hodgkin & Huxley, 1952) (Table 3.1).

Geometrical parameters of the HH model were as follows: the axon was 60 cm long, the recording electrode was situated 18.65 cm from the AP initiation point; with the injecting electrodes placed 0.1 cm further, separated by a 0.4-cm gap, similarly to (Aristovich *et al.*, 2015). All of the electrodes had a cylindrical shape 0.1 cm in width and 0.6 cm in diameter (Figure 3.1a, Table 3.2). The extracellular space had a cylindrical shape with the same diameter as the electrodes. The diameter of the squid giant axon was 0.1 cm, but it was modelled as a 1D line.

3D FEM mesh of the model consisted of approximately 55 thousand tetrahedral elements with the axon divided by 600 equal intervals. The size of the mesh was chosen using mesh convergence analysis (Shapeev & Lin, 2009): the number of elements was being increased until the solution stayed constant. As a result, a minimal number of elements required to obtain an accurate solution was used. In order to accelerate computations, the model was transformed into the 2D one with the axial symmetry along the fibre length (Figure 3.1b). All the geometrical parameters remained the same except for the mesh which became triangular (7500 elements in total). The numerical approach used for the solution of the reduced 2D axisymmetric models was the same as for the 3D models presented in the previous section.

Table 3.1
ELECTRICAL PARAMETERS OF THE HODGKIN-HUXLEY MODEL

Parameter	Value
ρ_i	50 Ω·cm
C_m	1 μF/cm^2
$\bar{g}_{Na}$	120 mS/cm^2
$\bar{g}_K$	36 mS/cm^2
$\bar{g}_{Leak}$	0.3 mS/cm^2
V_{Na}	55 mV
V_K	–72 mV
V_{Leak}	–50 mV
r_{ax}	0.5 mm
σ_e	10 mS/cm
V_{m0}	–60.15 mV
m_0	0.05
n_0	0.32
h_0	0.6

The first step was to study the effect of reducing the model into the 2D axisymmetric paradigm. For that, impedance changes simulated with this model at DC and 625 Hz were compared with the ones obtained with the 3D model (Figure 3.1a, b). Then, direct currents of various amplitudes (1.9 – 188 μA) and of two polarities at each amplitude were injected to check the amplitudes at which the impedance change was proportional to the applied current as it follows from Ohm's law. Too small currents would not allow dZ measurement due to modelling errors or, in case of

experiments, due to instrumentation noise; too large currents would influence the ion channels and modify the nerve physiology so that the dZ recordings become unreliable. Thus, the challenge was to find the optimal AC amplitude for the nerve dZ recording. The chosen amplitude was used at all studied frequencies. The same procedure was performed using 625 Hz AC, with a larger range of currents (1.9 – 754 μA).

Direct current and a range of alternating currents at 225 Hz, 625 Hz, 1025 Hz, 2, 4, 6, 8 and 10 kHz at the previously chosen amplitude were applied through the external injecting electrodes. The AP was initiated, and the signal was recorded via the external recording electrode with respect to ground. Simulations lasted 40 milliseconds to let the action potential, with velocity of ~15 *m/s*, propagate to the end of the axon. The time step used in the simulations equalled 10 μs which was equivalent to the recording sampling rate of 100 kHz. The obtained impedance changes were validated by injecting the current in different phase-antiphase pairs locked to the AP initiation. This procedure allowed elimination of artefacts occurring from the AP and its possible coherence with the AC wave. A more detailed explanation on the injection paradigm, extraction of dZ from the recorded voltages and on the origin of artefacts is provided in the signal processing section 3.2.5.

Table 3.2
GEOMETRICAL PARAMETERS OF THE HH AND C FIBRE MODELS

Parameter	HH axon	C fibre
Length	60 cm	2 cm
Fibre diameter	1 mm	1 μm
Propagation velocity	15 m/s	0.6 m/s
Diameter of the electrodes / surrounding volume, D_{el}	0.6 cm*; 0.05 – 1 cm	10 μm*; 5 – 100 μm
Width of the electrodes, H_{el}	0.1 cm; 0.02 – 0.4 cm	10 μm; 5 – 50 μm
Distance between recording and injecting electrodes, Δx_R	0.1 cm; 0.02 – 5.1 cm	0.01 cm; 10^{-3} – 0.1 cm
Distance between injecting electrodes, Δx_I	0.4 cm; 0.2 – 5.1 cm	$2 \cdot 10^{-3}$ cm; 10^{-3} – 0.1 cm

* First number in each row is the value used by default; range of values shows a variation of the parameter

To study the influence of the size and location of the electrodes on the simulations, diameters of the electrodes (together with the corresponding surrounding volume) and their widths were varied from 0.05 to 1 cm and 0.02 to 0.4 cm respectively. The position of the recording electrode with respect to the injecting pair (distance Δx_R), was varied from 0.02 to 5.1 cm. The same was done for the relative positions of the injecting electrodes Δx_I, from 0.2 to 5.1 cm (Table 3.2).

To study artefacts introduced by moving the recording electrode, dZ was measured and compared at different distances before and after the site of current injection, to match the experimental technique (Aristovich *et al.*, 2015).

To investigate how dZ depends on temperature, DC and AC currents, at 225, 625, 1025 Hz, 2, 4 kHz, were injected at 6.3 (original temperature), 11 and 21^{o}C. This was necessary for a valid comparison of the results of the HH model with the C fibre model and crab nerve experiments.

Finally, the changes in the flow of injected current through the membrane channels were studied to gain insight into the source of the observed apparent dZ. These changes were recorded and averaged at 18.65-18.75 cm along the fibre, the same location as the recording electrode.

3.2.3 A multiple fibre model with/without interaction

A model with multiple interacting fibres contained adjacent HH axons forming an "artificial nerve", so that axons interacted via extracellular potentials. The interaction between adjacent fibres was included in the model, as the external membrane activity of the fibres has previously been shown to affect membrane potentials of adjacent fibres (Clark & Plonsey, 1971; Barr & Plonsey, 1992). The effect of interaction was expected to be especially strong in the model containing HH axons due to high amplitudes of their extracellular APs (≈ 6.5 mV, Figure 3.5).

The scheme of the N-axon model operation (Figure 3.3) was similar to the one of a single fibre depicted in Figure 3.2. It contained one main and N additional 3D geometries. The first main 3D geometry served for the EIT current injection as well as

for compound nervous activity recording. N additional geometries simulated EAPs of each fibre separately without the applied current: their aim was to exclude the influence of the fibres' aggregate external field back on themselves but keep interaction between them. Two 1D models were done for each fibre (2·N 1D models in total): the first one served for simulation of the fibre with the applied current to be then transferred back to the main 3D geometry; the second one was needed to model interaction between axons so that each axon influenced all the surrounding axons apart from itself. The resultant field in each of the N additional geometries was subtracted from the compound activity in the main 3D geometry to be applied to each fibre at each simulation step. Eventually, this is an extension of the approach used for the single fibre (Figure 3.2).

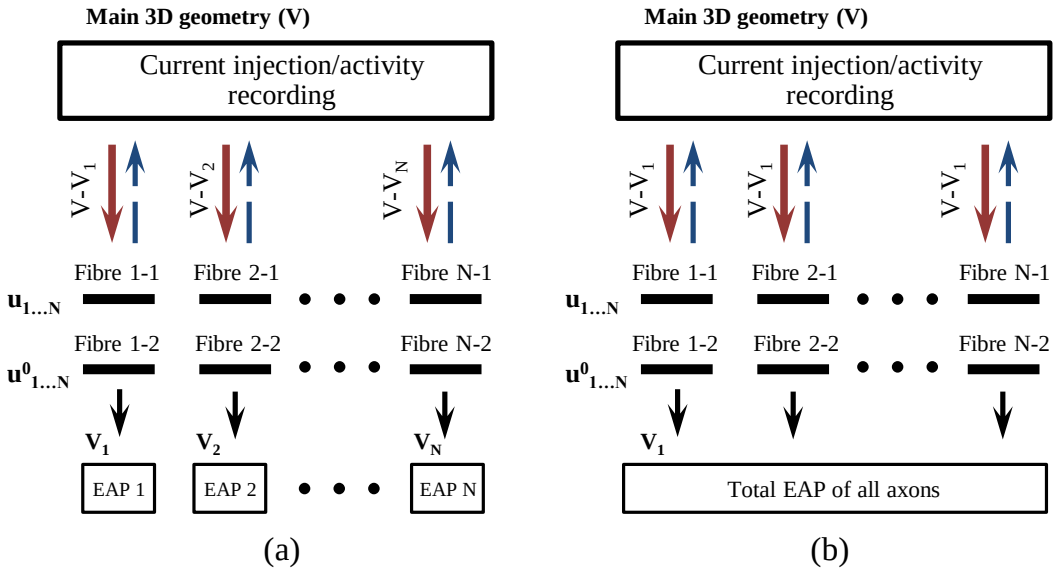

Figure 3.3 Schematic representation of the feedback coupling models' operation for multiple fibres. (a) Multiple interacting fibres. The same paradigm as for a single fibre was used, but there were N additional 3D geometries to simulate pure EAPs of N differently located fibres (V_1, …, V_N); (b) Multiple non-interacting fibres. The difference from the model with interaction is that there was only one additional 3D geometry with no applied current which included EAPs of all axons simulated together (V_1).

1D geometries were simulated with the HH equations (2.13), (3.11); current injection (3.3) together with volume conduction (2.22) and coupling (2.23) were modelled in all 3D geometries. All sub-models were fully coupled and computed simultaneously as described in the previous sections.

The dimensions of the multi-axon models were the same as the one-axon ones (Figure 3.1). The tetrahedral meshes of the 2, 4 and 8 axonal models contained 60, 78 and 88 thousand elements. To study the effect of interaction on dZ, all the intermediate N 3D models at the bottom of Figure 3.3a needed to be exchanged by one 3D model containing all the axons but no applied current (Figure 3.3b). The pure compound activity simulated in this geometry could then be subtracted from the summary activity in the main 3D geometry to be applied to each axon.

The complexity of the model with interaction increased with the number of fibres – an additional 3D and two additional 1D models had to be simulated for each added axon. Therefore, the influence of interaction on the impedance needed to be studied as it was a major consumer of computational resources. By taking interaction away or, by introducing a coefficient representing interaction, the model complexity could be dramatically reduced, and the computation time could be significantly decreased.

In order to measure the effect of the number of axons on the impedance change and to study the effect of interaction, the same simulations as for a single HH axon were undertaken for 2, 4, and 8 interacting axons (Figure 3.1c) – larger amount of fibres demanded considerably longer computation times.

3.2.4 Model of a mammalian C fibre

Because the electrical properties of a giant axon in the HH model differ from those small unmyelinated fibres, and because it, therefore, could not predict the behaviour of their activity with high accuracy, a new complex model had to be developed. It was based on one of the latest experimentally validated models of unmyelinated fibres (Tigerholm *et al.*, 2014) where the temporal dynamics of ion channels in mammalian C-nociceptor had been simulated. Compared to this model, the one developed in this chapter additionally contained the spatial dimension to simulate AP propagation as well as coupling with the extracellular space to inject current and record the activity externally.

Compared to the HH axon, the dimensions generally decreased because the diameter, magnitude of EAP and propagation velocity of a C fibre were many times

smaller (1 μm, 2 mV and ~0.6 m/s; Table 3.2). Therefore, the diameters (and corresponding external volume) and lengths of the electrodes were reduced to 10 μm, and the length of the axon to 2 cm. The electrodes were situated 0.769 cm from the end and the distances between them were: $\Delta x_R = 0.01$ cm and $\Delta x_I = 0.002$ cm (Figure 3.1a, Table 3.2). This model was also constructed in a 2D axisymmetric paradigm, as was done for a single HH fibre. Its triangular mesh contained about 4800 elements with the fibre divided by 1600 intervals.

The model contained ten time and potential-dependent nonlinear ion channels which were shown to be present in C-nociceptors (Tigerholm *et al.*, 2014): $Na_v1.7$, $Na_v1.8$, $Na_v1.9$, K_{DR}, K_A, K_M, K_{Na}, h-channel, Na-K Pump and Leakage. All the internal fibre equations and main parameters used for simulations were taken from (Tigerholm *et al.*, 2014) (Table 3.3). The external properties were modelled the same way as in the HH case (2.22) – (2.23), (3.7).

The main equation of the model describing AP propagation along the fibre and external current injection repeats the of for the HH model (3.11) except for the different ionic currents:

$$\begin{gathered}\frac{r_{ax}}{2\rho_i}\left(\frac{d^2V_m}{dx^2}+\frac{d^2V_e}{dx^2}\right)=C_m\frac{dV_m}{dt}+\sum I_{ion}(V_m)\,;\\ \sum I_{ion}(V_m)=I_{Na_v1.7}+I_{Na_v1.8}+I_{Na_v1.9}+I_{K_{DR}}+I_{K_A}+I_{K_M}+\\ +I_h+I_{K_{Na}}+I_{Na/K\,pump}+I_{Leak}\end{gathered} \tag{3.12}$$

Equations defining the ionic currents are presented below:

$$I_{Na_v1.7}=\bar{g}_{Na_v1.7}{m_{17}}^3h_{17}s_{17}\cdot\left(V_m-E_{Na}\left([Na_{sp}],[Na_{in}]\right)\right) \tag{3.13}$$

$$I_{Na_v1.8}=\bar{g}_{Na_v1.8}{m_{18}}^3h_{18}s_{18}u_{18}\cdot\left(V_m-E_{Na}\left([Na_{sp}],[Na_{in}]\right)\right) \tag{3.14}$$

$$I_{Na_v1.9}=\bar{g}_{Na_v1.9}m_{19}h_{19}s_{19}\cdot\left(V_m-E_{Na}\left([Na_{sp}],[Na_{in}]\right)\right) \tag{3.15}$$

$$I_{K_{DR}}=\bar{g}_{K_{DR}}n_{K_{DR}}^4\cdot\left(V_m-E_K\left([K_{sp}],[K_{in}]\right)\right) \tag{3.16}$$

$$I_{K_A} = \bar{g}_{K_A} n_{K_A} h_{K_A} \cdot \left(V_m - E_K\left([K_{sp}], [K_{in}]\right)\right) \tag{3.17}$$

$$I_{K_M} = \bar{g}_{K_M} \cdot \left(n_{sM}/4 + 3n_{fM}/4\right) \cdot \left(V_m - E_K\left([K_{sp}], [K_{in}]\right)\right) \tag{3.18}$$

$$I_{h,Na} = 0.5\bar{g}_h \cdot \left(n_{sh}/2 + n_{fh}/2\right) \cdot \left(V_m + E_{Na}\left([Na_{sp}], [Na_{in}]\right)\right) \tag{3.19}$$

$$I_{h,K} = 0.5\bar{g}_h \cdot \left(n_{sh}/2 + n_{fh}/2\right) \cdot \left(V_m + E_K\left([K_{sp}], [K_{in}]\right)\right) \tag{3.20}$$

$$I_{K_{Na}} = g_{K_{Na}}([Na_{in}]) \cdot w_{K_{Na}} \cdot \left(V_m - E_K\left([K_{sp}], [K_{in}]\right)\right) \tag{3.21}$$

$$I_{pump} = I_{K_{pump}} + I_{Na_{pump}} \tag{3.22}$$

$$I_{K_{pump}} = 1.62/(1 + (6.7/([Na_{in}] + 8))^3) \cdot \bar{g}_{pump}/\left(1 + 1/[K_{sp}]\right)^2 + 1/(1 + (67.6/([Na_{in}] + 8))^3) \tag{3.23}$$

$$I_{Na_{pump}} = -\frac{3}{2} I_{K_{pump}} \tag{3.24}$$

$$I_{Leak} = g_{K_{Leak}}(I_{ion}) \cdot \left(V_m - E_K\left([K_{sp}], [K_{in}]\right)\right) + g_{Na_{Leak}}(I_{ion}) \cdot \left(V_m - E_{Na}\left([Na_{sp}], [Na_{in}]\right)\right) \tag{3.25}$$

Gating variables for ion channels were computed via the same scheme as for the HH model (2.13):

$$\frac{dm_{17}}{dt} = k_{Na,K,h}(\alpha_{m_{17}}(V_m) \cdot (1 - m_{17}) - \beta_{m_{17}}(V_m) \cdot m_{17}) \tag{3.26}$$

and similarly, for all other gating variables. Functions $\alpha_x(V)$ and $\beta_x(V)$ nonlinearly depend on voltage, their equations can be found in (Tigerholm *et al.*, 2014); k_{Na}, k_K and k_h are temperature coefficients with Q_{Na}, Q_K and Q_h presented in Table 3.3; T_0 = 21ºC (Sheets *et al.*, 2007; Tigerholm *et al.*, 2014).

Sodium and potassium ionic concentrations in the axoplasm and periaxonal space were modelled as dynamical values differing with the membrane potential and the ionic currents (Scriven, 1981):

$$\frac{d[Na_{sp}, K_{sp}]}{dt} = \frac{\left(\frac{-\sum I_{Na,K}}{F} - D_{Na,K}\left([Na_{sp}, K_{sp}] - [Na_0, K_0]\right)\right)}{\theta} \quad (3.27)$$

$$\frac{d[Na_{in}, K_{in}]}{dt} = \frac{2\sum I_{Na,K}}{FR} \quad (3.28)$$

where θ is the width of periaxonal space, [cm], F – Faraday's constant, [$\mu A{\cdot}ms/mmol$], R – radius of the axon, [cm], $D_{Na,K}$ – permeability to Na or K ions respectively, [cm/ms]; $[Na_{sp}, K_{sp}]$ and $[Na_{in}, K_{in}]$ are periaxonal or intracellular concentrations of Na and K in [mM], $[Na_0, K_0]$ – concentrations in the extracellular space in [mM]; $\sum I_{Na,K}$ – sum of sodium or potassium currents through the membrane, [$\mu A/cm^2$].

Table 3.3
ELECTRICAL PARAMETERS OF THE C FIBRE MODEL

Parameter	Value
ρ_i	35.4 Ωcm
C_m	1 μF/cm^2
$[Na_{in}]_0$	11.4 mM
$[Na_{sp}]_0$	154 mM
$[Na_{out}]$	154 mM
$[K_{in}]_0$	121.7 mM
$[K_{sp}]_0$	5.6 mM
$[K_{out}]$	5.6 mM
$D_{Na,K}$	0.2·10^{-7} cm/ms
$Q_{10,Na}$	2.5
$Q_{10,K}$	3.3
$Q_{10,h}$	3
θ	29 nm
d_C	1 μm
T	300 K
σ_e	10 mS/cm
$\bar{g}_{Na_v1.7}$	106.6 mS/cm^2
$\bar{g}_{Na_v1.8}$	242.7124 mS/cm^2
$\bar{g}_{Na_v1.9}$	0.0948 mS/cm^2
$\bar{g}_{K_{DR}}$	18.0017 mS/cm^2
$\bar{g}_{K_A}$	12.7555 mS/cm^2
$\bar{g}_{K_M}$	6.9733 mS/cm^2
$\bar{g}_h$	2.5377 mS/cm^2
$\bar{g}_{K_{Na}}$	0.0012 mS/cm^2
$\bar{g}_{K_{pump}}$	0.0048 mS/cm^2
V_{m0}	-55 mV

Overall, a system of 22 equations has been solved to model the C fibre: 17 for gating variables (3.26), 4 for concentrations (3.27), (3.28) and the main equation (3.12); equation (2.23) was used to simulate fibre-to-external space coupling and (2.22) for 3D volume conduction, the same as in the HH model. The unknowns were potentials V_m, V_e, gating variables $m_{17,18,19}$, $h_{17,18,19}$, $s_{17,18,19}$, u_{18}, n_{Kdr}, n_{Ka}, h_{Ka}, n_{sM}, n_{fM}, n_{sh}, n_{fh}, w_{kNa}; concentrations of intracellular and periaxonal space $[Na_{in}]$, $[Na_{sp}]$, $[K_{in}]$, $[K_{sp}]$. All known parameters are presented in Table 3.3. The boundary conditions were the same as in the HH model (3.7). The initial conditions were chosen by assuming $dX/dt = 0$, where X is one of the gating

variables in (3.26) or concentrations in (3.27), and solving the corresponding equation in respect to this variable.

The same simulations were carried out as for the HH axon, except the model variables were decreased. The range of measuring currents was 0.03 to 63 nA; distance from the recording electrode to the site of injection (Δx_R) and distance between the injecting electrodes (Δx_I) were varied from 10^{-3} to 0.1 cm; diameter and width of the electrodes were varied from $5 \cdot 10^{-4}$ to $1 \cdot 10^{-2}$ and $5 \cdot 10^{-3}$ cm respectively (Table 3.2). Impedance changes at different recording positions were studied. Temperatures at which simulations were run included 37 (original temperature), 30 and 21ºC for comparison with the HH axon.

To compare the effect of complex ion channels and spatial structure of the fibre on the impedance response, a simpler model able to represent the activity of small unmyelinated fibre, and with reduced computational demands, was developed: it had HH ion channels, but the diameter of the fibre was reduced, changing the AP shape and propagation velocity. If the impedance response of this model matches the C fibre model, it will reduce complexity of the further modelling studies that may include the development of the full model containing numerous axons.

The geometric dimensions of the model were the same as in the C fibre model (Table 3.2); the diameter of the axon and the axoplasm resistivity were decreased to correspond to the C fibre (1 μm and 0.0354 $kOhm \cdot cm$). For this model, the frequency sweep was carried out with the same parameters as for the C fibre and the processed data was compared to both previous models.

The COMSOL model files for both the HH and C fibre models are provided in the EIT-lab GitHub repository at https://github.com/EIT-team/Unmyelinated-Model.

3.2.5 Signal processing

Signal processing to extract apparent impedance changes (dZ) of the system “fibre + external volume” during AP propagation was identical for all the constructed models (Figure 3.4).

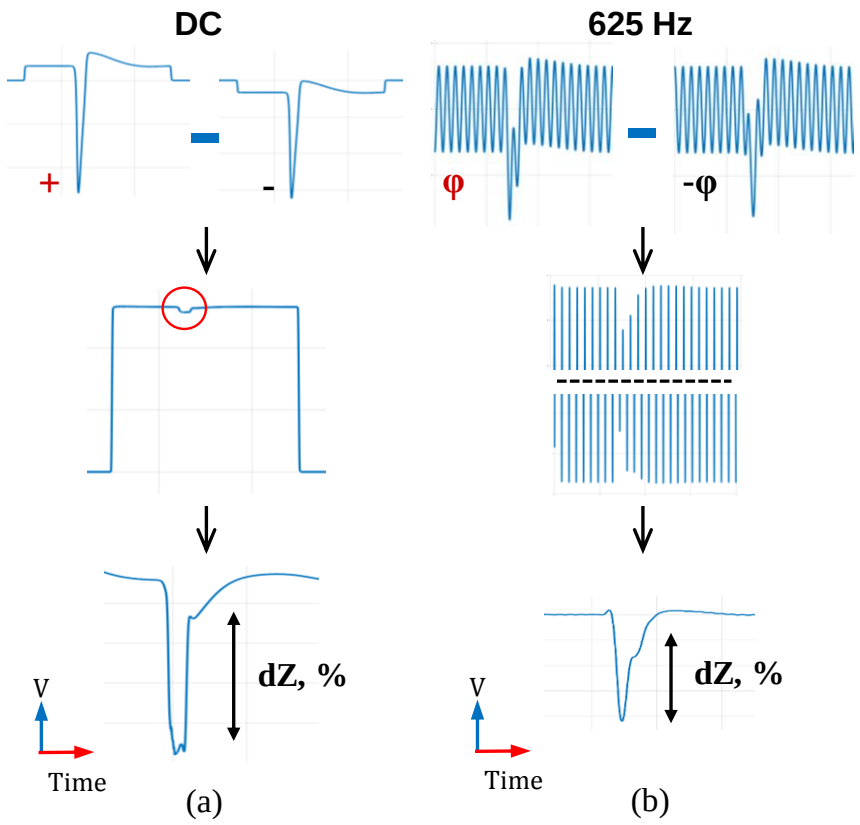

Figure 3.4 Extraction of the dZ during AP propagation for the developed models of unmyelinated fibres.
(a) DC. Signals simulated with the reversed polarity of the current were subtracted. The resultant impedance change was normalized to obtain the percentage value;
(b) AC. Signals simulated with the AC in phase and in antiphase with respect to AP initiation are subtracted. Impedance change is computed via band-pass filtering, demodulation and normalization of the resultant signal.

For the case of AC injection (Figure 3.4b), to obtain a single measurement, two simulations with AC applied in phase and in antiphase locked to the time of AP initiation were undertaken. At all simulated frequencies (225, 625, 1025 Hz, 2, 4, 6, 8, 10 kHz) in-phase recordings included phases: 0, $\pi/4$, $\pi/2$; and antiphases $-\pi$, $-3\pi/4$, $-\pi/2$ respectively; additional simulations with AC phases $7\pi/8$, $5\pi/8$, $19\pi/20$ and $-\pi/8$, $-3\pi/8$, $-\pi/20$ were done at 225 and 625 Hz for HH fibre and at 225, 625 and 1025 Hz for C fibre. This was necessary as these frequencies were lower or equal to the characteristic frequency of the dZ of the corresponding fibre, which increased errors in subsequent demodulation. In the DC case (Figure 3.4a), two simulations with the switched positive and negative electrodes were carried out for the same purpose. Based on this, standard deviations of the dZ at the range of frequencies were also calculated.

For the chosen amplitude of the current, [5 frequencies · (3 phases + 3 antiphases)] + [2 frequencies (225,625) · (3 phases + 3 antiphases)] + [1 frequency (DC) · 2 states] = 44 simulations were carried out.

At all frequencies, the resultant signals from simulations in phase and in antiphase were subtracted leading to cancellation of the AP and doubling of the dZ. Then, for AC currents, long (500 ms) sine waves of the same amplitude and frequency were artificially added on both sides of the signal to remove ringing artefacts in the subsequent filtered and demodulated signal. To completely eliminate the EAP, band-pass filtering around the carrier frequency was carried out using a 1st order Butterworth filter in forward and backward directions with a 400 Hz bandwidth for frequencies starting from 625 Hz and 200 Hz for 225 Hz. Finally, due to the fact that the membrane does not change the phase angle of the applied current (Cole & Curtis, 1939), the absolute value of the sought-for dZ could be found by demodulation using the modulus of the Hilbert transform (3.1). Then, it was normalized with respect to the baseline so that a percentage dZ plot could be obtained. For the DC case, signals with the current in the reversed polarity were subtracted and the resultant signal was normalized.

3.3 Results

3.3.1 FEM model of Hodgkin-Huxley squid giant axon

In the model, the AP amplitude, duration, spatial length and conduction velocity (110 *mV,* 17 *ms,* 26 *cm,* 15 *m/s*) corresponded to those recorded experimentally and modelled by Hodgkin and Huxley (Hodgkin & Huxley, 1952). The amplitude of the simulated extracellular AP was approximately 7 *mV* (Figure 3.5a).

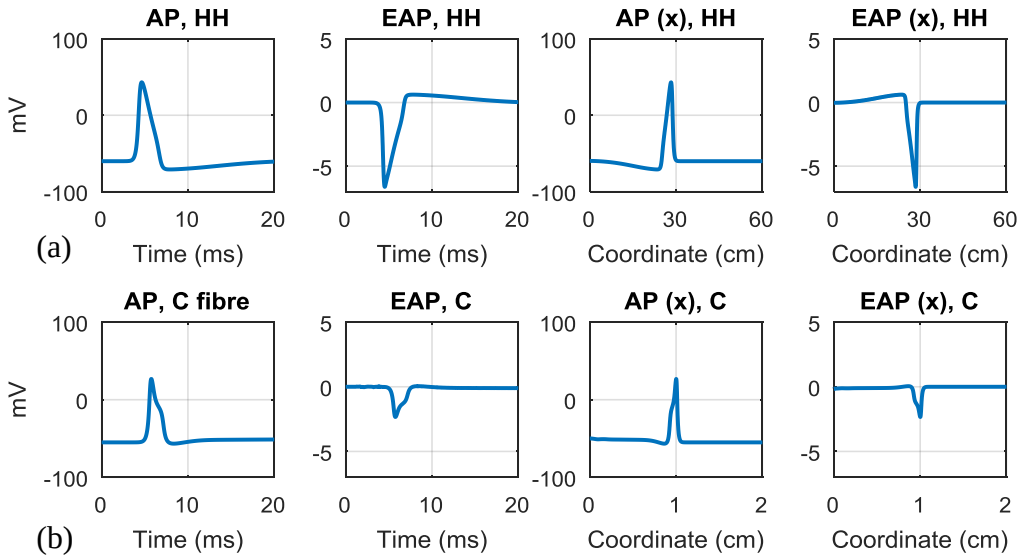

Figure 3.5 Action potentials simulated with the developed unmyelinated fibres models.
(a) HH model; (b) C fibre model. For both models, the first two columns show intracellular (AP) and extracellular action potentials (EAP) in time; columns 3 and 4 – along the fibre length.

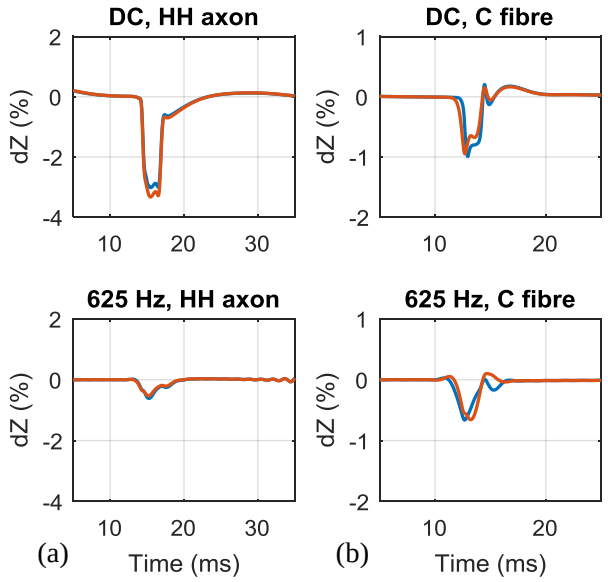

Figure 3.6 Comparison of dZ computed with 3D (blue lines) and 2D axisymmetric (red lines) models of (a) a single HH axon and (b) a C fibre at DC (top) and 625 Hz (bottom).
Time markers during simulation: AP excitation – 2 ms from the start (both fibres); AP passes under the recording electrode – 14.5 ms (HH axon) and 12 ms (C fibre), AP reaches the end of the fibres in 40 ms (HH axon) and in 26 ms (C fibre).

In a 2D axisymmetric model, the dZ closely matched those of the 3D model (Figure 3.6a, dZ at DC and 625 Hz are shown as an example). The 2D axisymmetric model was then therefore used for all further single fibre simulations.

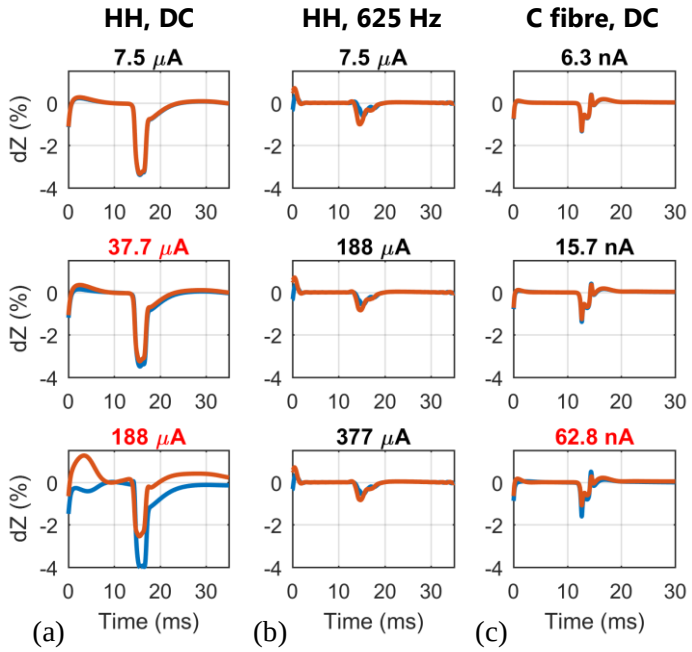

Figure 3.7 Modelled dZ at various current amplitudes for (a) HH fibre, DC; (b) HH fibre, 625 Hz; (c) C fibre, DC.
Titles highlighted in red show the current outside the safe range. Red and blue lines designate dZ recorded with current at different polarities. Distortions at the starts of the dZ curves are edge effects caused by switching the current on and its effect on the membrane. AP time markers are the same as in Figure 3.6.

The modelled dZ were linear with the applied DC currents from 1.9 up to 7.5 µA. Currents in this range did not induce membrane excitation and the dZ values in percentage terms were equal for all currents (Figure 3.7a). At higher currents, the dZ became nonlinear and started to depend on polarity. The upper limit increased at higher frequencies: for example, at 625 Hz dZ was still linear with the current at 377 µA (Figure 3.7b). Thus, currents below 7.5 µA were "safe" at all frequencies so that they did not activate the membrane and the measured impedance changes were linear with them; 7.5 µA was therefore chosen for use in all simulations with HH axons.

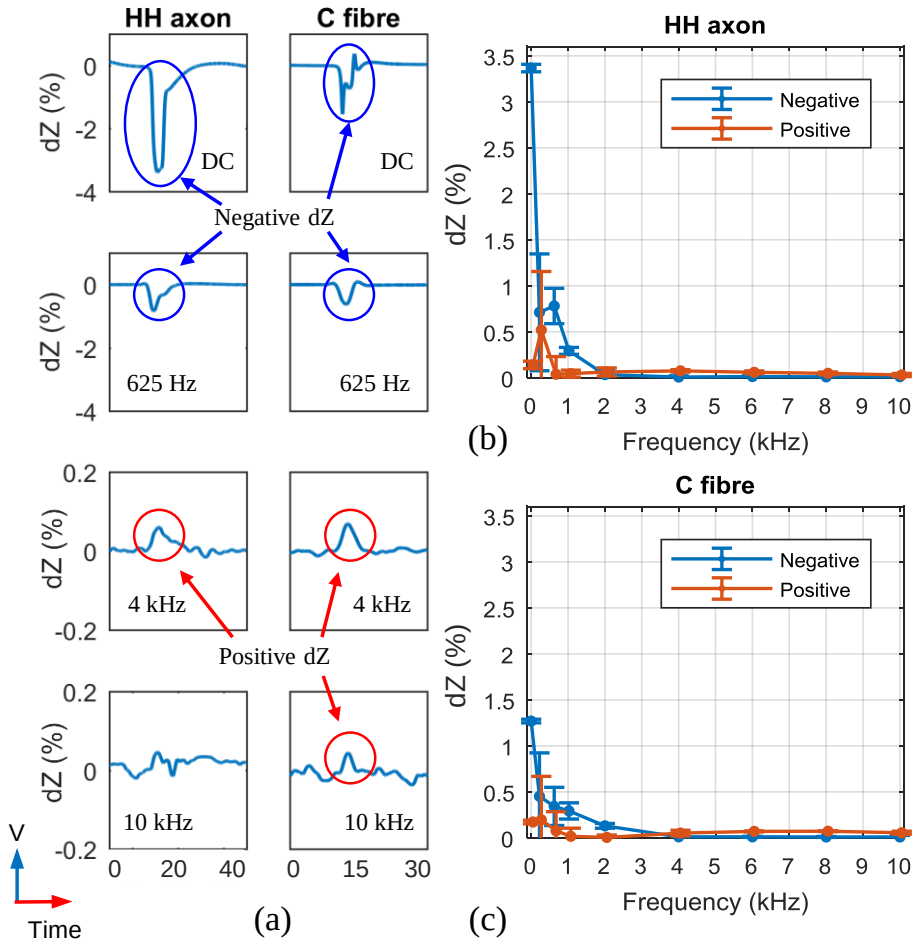

Figure 3.8 Dependence of the simulated dZ on frequency for the HH and C fibre models. (a) Examples of dZ at DC, 625 Hz, 4 and 10 kHz. Negative impedance changes are highlighted by blues circles, positive ones – by red circles; (b) Absolute dZ vs. frequency for HH axon, I = 7.5 µA; (c) Absolute dZ vs. frequency for C fibre, I = 6.3 nA. Blue lines designate impedance decrease (negative change), red – impedance increase (positive change). Error bars are standard deviations calculated for the dZ simulated at different phases of the current (AC) and at different polarities (DC). Time markers are in the caption of Figure 3.6.

For the initial geometry of the model (Figure 3.1, Δx_R = 0.1 cm, Δx_I = 0.4 cm), the simulated negative apparent impedance changes fell with frequency from -3.36±0.04% at DC to -0.7±0.6% at 225 Hz, -0.8±0.2% at 625 Hz to -0.30±0.04% at 1025 Hz and were around zero above 2 kHz (Figure 3.8a). The errors were larger at low frequencies because they were close to the characteristic frequency of dZ (~200 Hz, Figure 3.7a, b) resulting in errors in demodulation of corresponding sine waves (Figure 3.4). Significant dZ increases were observed at DC – 0.14±0.04%, and at high frequencies, where they were relatively constant at 2, 4 and 6 kHz: 0.06±0.04%, 0.07±0.02%,

0.06±0.01%, and decreased to 0.05±0.01% and 0.03±0.01% at 8 and 10 kHz (Figure 3.8a).

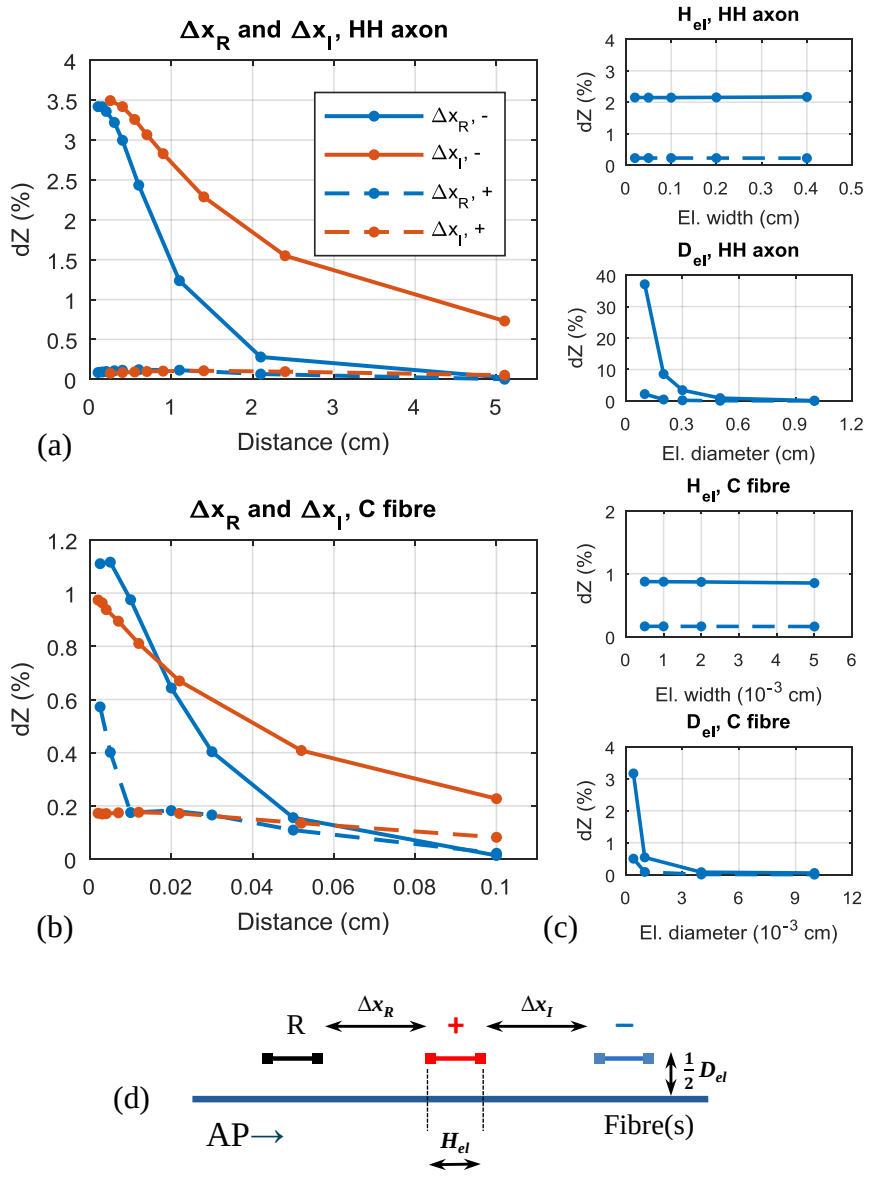

Figure 3.9 Absolute HH and C fibre dZ versus size and position of electrodes.
(a) HH model and (b) C fibre model dependence on distance between the recording and injection electrodes (Δx_R) and between injecting electrodes (Δx_I). dZ vs Δx_R is depicted with blue lines, dZ vs Δx_I – with red lines. Negative dZ are shown by solid lines, positive – by dashed lines.
(c) Dependence of dZ on width (H_{el}) and diameter (D_{el}) of the electrodes. HH model is on the top two graphs, C fibre – bottom graphs. Solid lines designate negative dZ, dashed lines – positive dZ;
(d) Scheme of the dimensions used in the study.

When increasing distances between the recording and injecting electrodes (Δx_R) and between the injecting electrodes (Δx_I), a dZ decrease was observed which was steeper

with Δx_R (Figure 3.9a). There was also a decrease at very small distances determined by limitations of the model: the size of the mesh elements became larger than these distances. The maximum values of dZ were simulated at Δx_R = 0.1 cm and Δx_I = 0.35 cm. The impedance increase was constant along the range of these values. The negative and positive dZ decreased significantly with increasing radii of the electrodes and was approximately independent of their length (Figure 3.9c).

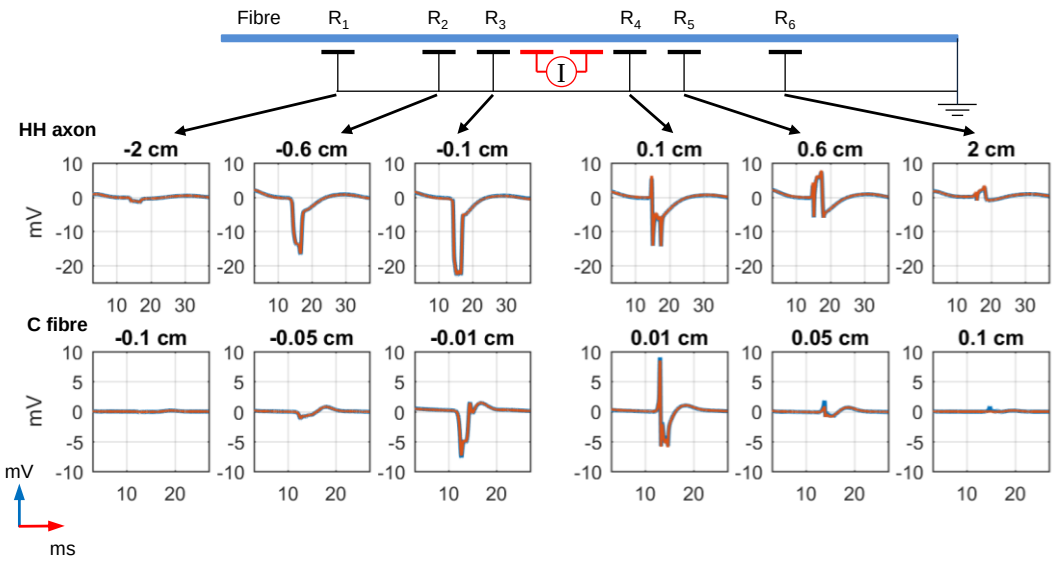

Figure 3.10 dZ in the HH and C fibre models simulated at DC with different positions of the recording electrode: 2, 0.6 and 0.1 cm before and after the site of injection.
The dZ shape recorded prior the site of injection stays the same with magnitude falling with distance (left side). Artefacts appear after the site of injection, in accordance with (Aristovich *et al.*, 2015) (right side). Colours represent different DC polarity.

The shape and negative polarity of the dZ recorded before the site of injection was the same irrespective of the distance from it and the polarity of the current (Figure 3.10). In contrast, the dZ measured with the electrodes placed after the injection site were affected by artefacts, in accordance with experiments (Aristovich *et al.*, 2015).

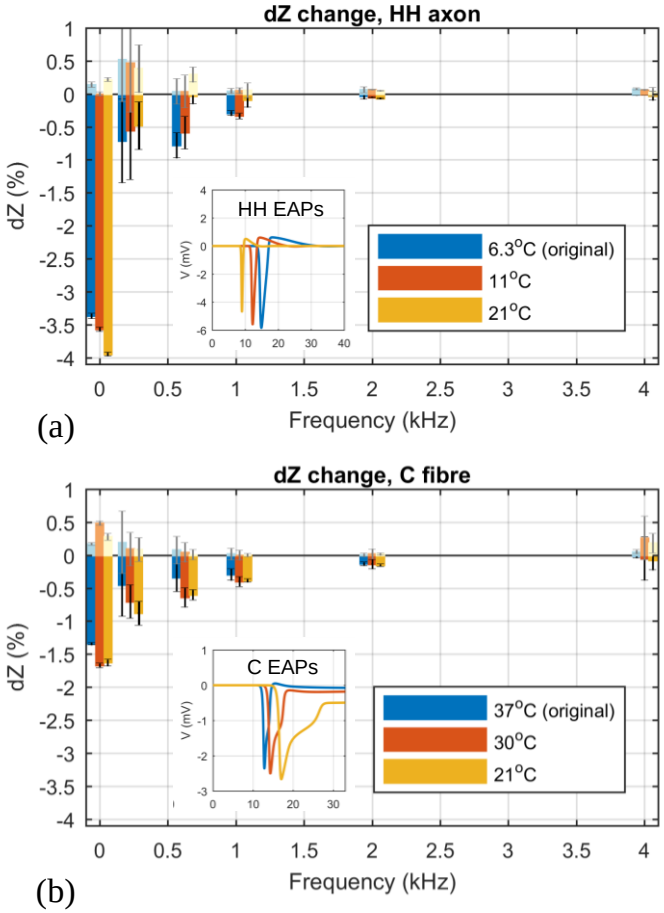

Figure 3.11 Temperature dependence of the negative and positive dZ in the HH model (a) and the C fibre model (b).
For the HH model, dZ were simulated at 6.3 (original temperature), 11 and 21ºC; for the C fibre: at 37 (original temperature), 30 and 21ºC. EAPs recorded at the same temperatures are embedded into the graphs.

As temperature increased, durations and amplitudes of APs decreased, and propagation velocities increased; however, the general behaviour of the dZ with frequency did not significantly differ across temperatures (Figure 3.11a). The only feature found to depend on temperature was a steepness of decrease in the negative dZ with frequency. For instance, dZ decrease was zero above 625 Hz at 21ºC, while at the original temperature, it approached zero only at 2 kHz (Figure 3.11a).

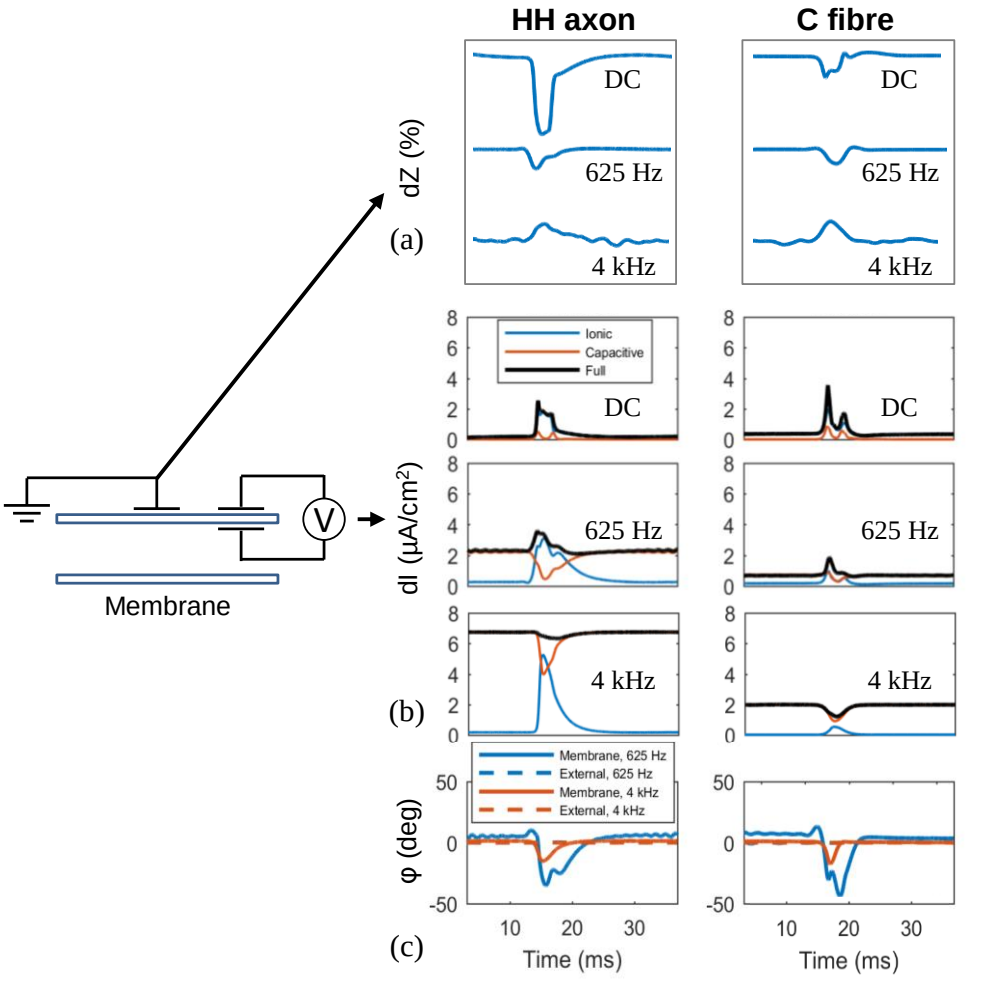

Figure 3.12 dZ, the associated change in the flow of the injected EIT current through the membrane and the change in its phase during depolarization.
(a) dZ simulated at DC, 625 Hz and 4 kHz; (b) Flow of the injected EIT current through ion channels (blue lines), capacitance (red lines) and full current flow (black lines) at DC, 625 Hz and 4 kHz for HH axon and C fibre; (c) Change in the phase of the injected AC current measured internally (i.e. current which has gone through the membrane, full lines) and externally (by the recording electrode, dashed lines) at 625 Hz (blue) and 4 kHz (red) for HH axon and C fibre.

Absolute changes in the EIT current flow through all the pathways of the membrane were found during AP propagation at DC, at 625 Hz and at 4 kHz (Figure 3.12b). At 625 Hz, before depolarization had reached the location of current injection (< 12 *ms*), there was a steady baseline current flow through capacitance (~2.2 $\mu A/cm^2$) and small flows through Na, K and leakage ion channels (~0.3 $\mu A/cm^2$ in total). During AP, there was a switch in the membrane path through which AC flowed: C-current fell significantly (to ~0.4 $\mu A/cm^2$) which was accompanied by increases in flows through ion channels to ~3 $\mu A/cm^2$. Total AC flow through the membrane also increased during

AP from 2.4 to 3.5 $\mu A/cm^2$, equalling 45 % increase. This total increase in the current flow through the membrane explains the observed negative impedance change.

At DC, there was no flow through capacitance at rest, consequently, there was a larger relative increase in the full current flow determining larger dZ (0.2 to 1.8 $\mu A/cm^2$, or 800 %) (Figure 3.12b). At 4 kHz the behaviour of the currents flow was similar to 625 Hz. However, there was a small decrease in the total AC flow through the membrane (6.7 to 6.3 $\mu A/cm^2$, or 6%, Figure 3.12b), which was due to a phase change of the current flowing through the membrane during depolarization (Figure 3.12c). Because of this phase change, the absolute value of the total current change was not equal to the sum of the absolute values of changes of separate currents; therefore, a decrease in the current flow and an increase in the impedance could be seen (Figure 3.8, Figure 3.12). The phase change of the external signal recorded by the recording electrode was negligible (Figure 3.12c) due to high baseline voltage (in accordance with the experimental study (Cole & Curtis, 1939)); it did not allow to account for it in the dZ signal processing (Figure 3.4).

3.3.2 Multi-axon model. Effect of size and interaction

For increased axon numbers up to 8, the relationship between the number of axons and impedance change was close to linear, so that the ratio of dZ with N axons to dZ with 1 axon was close to N (Figure 3.13). Also, the dZ response did not differ after turning off interaction between axons: one-way ANOVA test was accomplished which revealed no significant differences across multi-axonal models with and without interaction at all frequencies.

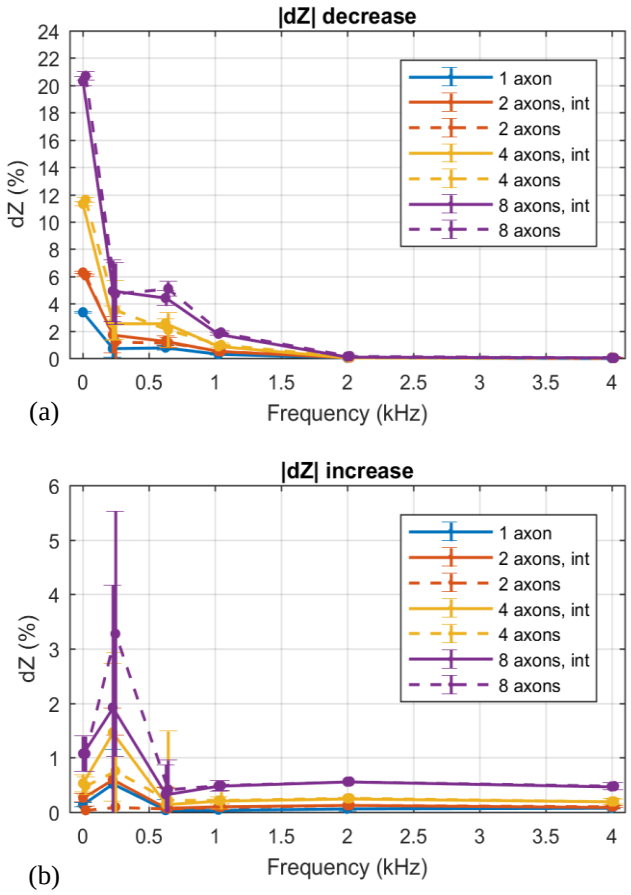

Figure 3.13 Negative (a) and positive (b) dZ for 1-, 2-, 4- and 8-axonal HH models with and without interaction.
Colours represent a model with a different number of axons. Models simulated with the interaction between axons are designated by full lines, without interaction – by dashed lines.

3.3.3 Model of a mammalian C fibre

Compared to the AP of HH axons, the AP of a C fibre was shorter in duration and of a more complex shape, representing various properties of excitation such as depolarizing afterpotentials and hyperpolarizing afterpotentials (Figure 3.5b).

As for the HH axon, the difference in dZ of 3D and 2D axisymmetric models was indistinguishable (Figure 3.6b).

The linear dependence of the C fibre dZ on the measuring currents from 0.6 to 6.3 nA (0.4 to 4 mA/cm^2) could be seen so that the percentage dZ change stayed the same at these currents (Figure 3.7c). At 62.8 nA dZ became nonlinear and dependent on the

polarity. Thus, 6.3 nA was shown to be the maximum current giving correct dZ values; it was therefore confirmed to be within the safe range and suitable for all further modelling.

The impedance response of a C fibre differed from the HH axon. The impedance changes were: -1.34 ± 0.02%, -0.45 ± 0.45%, -0.34 ± 0.21 %, -0.29 ± 0.09%, -0.13 ± 0.03% at DC, 225, 625, 1025 and 2000 Hz respectively; it was zero at higher frequencies (Figure 3.8b). The positive impedance changes comparable to those of the HH fibre were also recorded. They were significantly different from zero at DC, 4, 6, 8 and 10 kHz, with the values of 0.17±0.02%, 0.05±0.03% at DC and 4 kHz and 0.07±0.01% at 6, 8 and 10 kHz (Figure 3.8b).

Apparent positive dZ appeared for the same reasons as for the squid giant axon, where the phase of the current flowing through the membrane changes during an AP. This makes the absolute value of the sum of these currents different from the sum of their absolute values, causing an artefactual reproducible decrease in the total current flow and corresponding increase in the dZ (Figure 3.12).

Large standard errors at low frequencies demonstrated high sensitivity of dZ to the phase of the applied current. The reason was that the characteristic frequency of the C fibre's dZ (~ 500 Hz, higher than of HH axon, Figure 3.7c) was close to these frequencies affecting the precision of demodulation in signal processing (Figure 3.4).

The negative dZ decreased with increasing Δx_R and Δx_I, and the positive change stayed approximately constant, the same way as in HH fibre (Figure 3.9b). High positive dZ was seen at very close distances to the site of injection (Δx_R < 0.01 cm), which could be due to edge effects of the current distribution. The recorded impedance change decreased with increasing electrodes diameter and did not change with their width (Figure 3.9c). Equivalently to the HH case, the dZ artefacts appear only if the recording takes place after the site of current injection, in agreement with (Aristovich *et al.*, 2015) (Figure 3.10).

Frequency responses of the dZ at different temperatures did not significantly differ (Figure 3.11b), the same as for the HH model. For this model, steepness of the dZ-frequency curve was found to be independent of temperature.

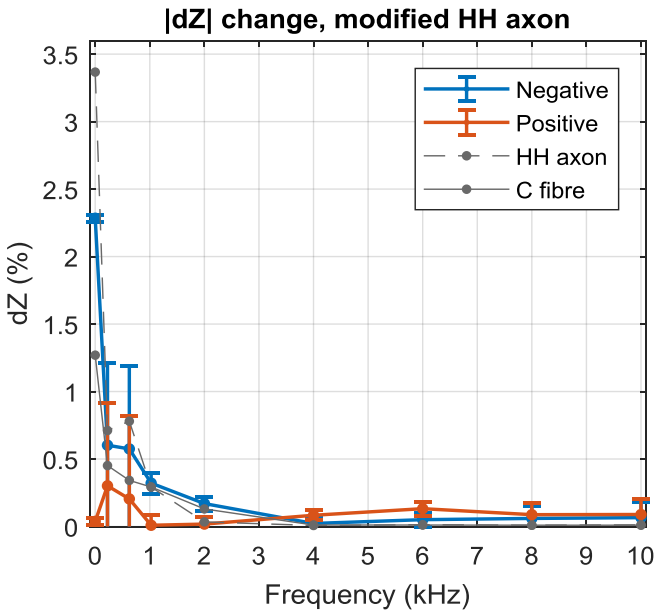

Figure 3.14 dZ of a spatially modified HH axon with the geometrical dimensions as in the C fibre model and ion channels of the HH model.
For comparison, negative dZ of the initial HH and C fibre models are depicted by grey lines (also presented with standard deviations in Figure 3.8).

The impedance response of the model of a spatially modified HH axon which had the same geometric dimensions as the C fibre model (including the size of the electrodes and the volume conductor, see section 3.2.4), was significantly different from the C fibre model and became closer to the HH model of the squid giant axon (Figure 3.14). The negative dZ fell about 8-fold from DC to 1 kHz, its values were: -2.28 ± 0.03%, -0.6 ± 0.6%, -0.57 ± 0.59%, -0.30 ± 0.08%, -0.17 ± 0.05% at DC, 225, 625, 1025 and 2000 Hz respectively and zero at other frequencies. Significant impedance increases equalling 0.08 ± 0.04% and 0.13 ± 0.05% were also observed at 4 and 6 kHz.

3.3.4 Comparison with experimental data

The values of the negative dZ obtained in the crab nerve experiments (4–6ºC) at 125-1025 Hz (Oh *et al.*, 2011; Aristovich *et al.*, 2015) together with those at DC (Holder, 1992; Boone, 1995; Gilad *et al.*, 2009) have the same general frequency dependence as the ones simulated in this chapter with all models. For example, in (Oh

et al., 2011) authors obtained 0.25 to 0.06% negative changes at 125 to 825 Hz recorded on 15 nerves; in (Aristovich *et al.*, 2015) negative dZ were from 0.05 to 0.02% at 225 to 1025 Hz respectively on 12 crab walking leg nerves. At DC, dZ equalling from 0.2 – 1 % were obtained (Holder, 1992; Boone, 1995; Gilad *et al.*, 2009). No studies are available to confirm positive changes at high frequencies, – they are to be carried out in future.

The dependence of dZ on the distance between electrodes (Δx_R, Δx_I) predicted by the models developed here agreed with the experimental values for Δx_I (Boone, 1995; Gilad *et al.*, 2009; Oh *et al.*, 2011) but differed from the ones for Δx_R (Holder, 1992; Gilad *et al.*, 2009). In the latter studies, authors claimed that Δx_R should be not less than 2 space constants so that the applied current does not modify it. However, simulations in the current study showed the inverse – as long as the current is small enough, the AP is not modified by it even at the small distances from the site of injection (Figure 3.10).

3.4 Discussion

3.4.1 Summary of results

1) For both the HH and C fibre models, a negative apparent dZ was maximal at DC and steadily decreased at higher frequencies (Figure 3.8); this was supported by the available experimental data (Holder, 1992; Boone, 1995; Gilad *et al.*, 2009; Oh *et al.*, 2011; Aristovich *et al.*, 2015). The rate of the decrease was lower in the C fibre model which could be explained by its smaller size and complex ion channels kinetics. In addition, in both models, this rate was lower than the one predicted by the previously developed Liston's passive model where no change is expected at above 1 kHz (Liston *et al.*, 2012). Small positive dZ were also observed at high frequencies and DC (Figure 3.8).

2) The dZ expressed in percent did not depend on the amplitude of applied current in the safe range, the upper bound of which equalled 7.5 μA for HH axon and 6.3 nA for a C fibre.

3) In a 3D model with multiple interacting axons, the dZ increase was near-linear with the number of fibres at all frequencies. The interaction between fibres did not significantly affect the dZ (Figure 3.13).

4) dZ generally decreased with increasing distances between the recording and injecting electrodes (Δx_R) and between injecting electrodes ($\Delta x_{I,}$). It corresponded to the experimental values for Δx_I (Boone, 1995; Gilad *et al.*, 2009; Oh *et al.*, 2011) but differed from the ones for Δx_R (Holder, 1992; Gilad *et al.*, 2009) where it was claimed that it had to be higher than two space constants of the nerve not to modify the AP. However, modelling showed that AP is not modified at much closer distances if the recording electrode lies before the site of current injection (Figure 3.10). The dZ decreased significantly with increasing electrodes diameter and almost did not change with increasing electrodes width (Figure 3.9).

5) The absolute dZ magnitude did not significantly differ with temperature in both HH and C fibre models; steepness of decrease of the negative dZ with frequency increased with temperature for the HH model (Figure 3.11).

6) The dZ measured during membrane excitation was found to originate from an increase in total current through the membrane which, in turn, was caused by an increase in current flow through sodium and subsequent increase through potassium ion channels. A small impedance increase at DC could be explained by the inactivation phase of sodium channels as well as by redistribution of the applied current under the recording electrode; at AC, it was due to a phase change during AP at high frequencies (Figure 3.12c).

7) Simulations confirmed previous experimental findings: the highest negative impedance change was observed at DC and decreased with frequency in both HH and C fibre models. The models also confirmed that to measure maximal dZ, the injecting electrodes should be as close as possible. However, contrary to the

previous studies, findings suggest reduction of the distance between the recording and injecting electrodes: if the current is low enough, it will neither modify the AP nor cause an artefact (Figure 3.10).

3.4.2 Answers to the stated questions

1. How does the impedance change vary with experimental parameters?

a) AC amplitude and frequency;

The maximum current level for the HH axon at which dZ were linear with it was 7.5 µA at DC (Figure 3.7a); although slightly higher currents did not induce AP, the impedance response became nonlinear and started to depend on the direction of the current, which is not suitable for experimental measurements. The safe range significantly widened with frequency (Figure 3.7b). For a C fibre, the safe limit of the current not affecting the fibre was much smaller – 6.3 nA (Figure 3.7c). Such a small current could be explained by very small electrodes needed to maintain a high current density.

The HH axon model with the initial electrode position (Figure 3.1) showed that the maximum dZ decrease was observed at DC and decreased with frequency, so that it was about 10 times smaller at 1025 Hz and approached zero at 4 kHz and above (Figure 3.8). Small significant impedance increases were also observed at DC and higher than 4 kHz. The complex mammalian C fibre model also showed a similar dZ behaviour with the negative dZ decreasing with frequency; however, the steepness of this decrease was slower – about 2 times from DC to 1025 Hz compared to the 10 times for HH model and 8 times for spatially modified HH model (Figure 3.8, Figure 3.14). Positive dZ with the same frequency dependence were also observed.

b) size and position of the electrodes;

Location of the electrodes was found to play a critical role in the dZ determination. For both HH and C fibre models, negative dZ decreased with increasing Δx_R and Δx_I (Figure 3.9a, b). Positive dZ were approximately constant across frequencies except

for the C fibre one becoming artefactual at very small Δx_R. For both models, the dZ decreased with increasing electrodes diameter and stayed constant with increasing their width (Figure 3.9c).

c) number of fibres and interaction between them

The HH model with up to 8 axons demonstrated that the number of fibres had no effect on the dependence of dZ on frequency and influenced only the magnitude of the dZ. The dZ was shown to be approximately equal to a single-axon dZ multiplied by a number of axons (Figure 3.13).

With one-way ANOVA test, the interaction between fibres was shown not to be critical for evaluating the absolute dZ in the HH model. It did not affect the general trend of the impedance dependence on frequency and its effect did not rise with the number of fibres (Figure 3.13). For a C fibre model, the magnitude of its EAP on the surface is 3 times smaller than the one of the HH axon (Figure 3.5) meaning that the effect on the adjacent fibres will also be considerably smaller even if they are closely packed. Thus, the interaction is expected to have no significance for dZ simulation in this model.

d) Model complexity

The complexity of the model significantly affected magnitudes of simulated dZ but did not influence its overall behaviour with frequency. The slope of the dZ decrease of the complex fibre was smaller compared to the HH axon as well as the modified HH axon with the size reduced to the C fibre's one. Therefore, it can be inferred that the kinetics of complex ion channels play a vital role in dZ determination. In addition, when the two models were simulated at the same temperature (21ºC), the slopes remained at similar levels.

2. Does this agree with previous studies?

a) Does the model confirm the experimental recordings?

The described behaviour of the impedance decrease with frequency is in agreement with the obtained experimental data for the unmyelinated crab nerve (Holder, 1992; Boone, 1995; Gilad *et al.*, 2009; Oh *et al.*, 2011; Aristovich *et al.*, 2015).

Absolute values obtained for the whole thousands-of-fibres crab nerve were not many times higher than the ones modelled here due to several reasons. First, fibres in the real nerve do not fire simultaneously which causes dispersion weakening the compound action potential formed by APs of separate fibres; that consequently decreases the amplitude of the impedance change. Also, to obtain visible impedance changes of a single fibre, the modelled electrodes were 1) extremely small ($1.6 \cdot 10^{-4}$ mm^2 surface for a C fibre) to inject low current with a high current density; 2) located very close to the fibre ($5 \cdot 10^{-3}$ mm) to increase the amplitude of the recorded EAP. It strongly increased the obtained absolute dZ compared to the experimental ones where the surface of the smallest used electrodes was up to 0.5 mm^2 (Aristovich *et al.*, 2015). Finally, real nerves have plenty of connective tissue with conductivity lower than extracellular fluid modelled in this study.

However, the model reached its original purpose which was to validate general dZ behaviour with EIT parameters, find the optimal parameters to obtain the largest response and to investigate into a biophysical explanation of impedance changes. Also, because the dependence of the negative dZ on frequency did not change with the number of fibres, predictions on frequency obtained for a single fibre can be used for a real nerve experiments which is a significant result of the current work.

b) Does it offer a biophysical explanation?

The analysis of the membrane currents in both models has shown that the nature of the externally recorded apparent impedance change could be presented as a superposition of two effects: change in the current amplitude flowing through different membrane channels and change of its phase accompanying excitation.

The significant apparent positive impedance changes were simulated at DC and at high frequencies. Those at DC appear straight after the negative change and may have

been due to the inactivation phase of the sodium ion channels which causes a small decrease in the full current flow in respect to the resting state following depolarization (Figure 3.12b); this effect becomes negligible at AC. These changes show the real increase in the membrane impedance because the resistance of the sodium channels during the phase of inactivation decreases compared to the resting state. Redistribution of the current flowing under the external electrode induced by the ion channels' activity might also affect the impedance measurements and cause an increase in the apparent dZ and decrease in the full current flowing through the membrane (Figure 3.12b), according to the equation (3.2) where the current was assumed to be constant.

The apparent positive dZ at high frequencies were found to be associated with the change in the phase of the injected current flowing through the membrane (Figure 3.12). AC phase alters during AP at all frequencies, but due to the same time of occurrence with the negative change and because the negative change is much larger at low frequencies, significant positive dZ related to a phase change can be observed only at high frequencies where negative changes are absent. These changes do not reflect the rise of real membrane impedance consisting of the active (resistive) and reactive (capacitive) components; conversely, they show an artefactual dZ increase appearing due to the summation of sine waves in divergent phases corresponding to the flow of AC current through ion channels and capacitance.

Although the impedance increase is artefactual, it is reproducible and constant across high frequencies, which could allow it to be used for EIT nerve imaging. Using high-frequency currents will allow accurate extraction of impedance changes even with high characteristic frequencies.

c) Does it differ from the previous modelling?

The active models developed in this chapter generally support findings obtained with the passive model created for the same purpose (Liston *et al.*, 2012). However, comparison of the active models demonstrated that the rate of the dZ decrease with frequency may be different depending on the ion channels present in the membrane, which can be of high importance in choosing the optimal AC frequency for imaging the particular nerve with fast neural EIT. Also, the active models predict the existence

of positive dZ at DC and high frequencies which are due to be experimentally validated.

3. Which model options are recommended for further modelling studies?

The models predicted similar general dependence of dZ on frequency, which was supported by experimental data (Figure 3.8). In addition, apparent positive impedance changes at higher frequencies (Figure 3.8), dependence of dZ on dimensions of the models (Figure 3.9) and the biophysical nature of the observed dZ (Figure 3.12) were also consistent across the models. However, there were differences in the temporal and spatial properties of the APs (Figure 3.5), the slope of the decrease of dZ with frequency (Figure 3.8) and the maximum injected current not causing artefacts (Figure 3.7). Therefore, as distinctions exist, and because the mammalian C fibre model was experimentally validated, it must be currently preferred over the HH model for any future developments of a full model of the autonomic nerve. The paradigm used to build the multiple-fibre HH model (Figure 3.13) could also be used.

3.4.3 Technical issues

The main technical problem faced during simulations was the lack of computational resources due to the highly nonlinear nature of the equations to be solved simultaneously on a large FEM mesh. For example, the complex C fibre model took about a day to compute at a single AC frequency on a 16-core workstation. Simulations of HH models with multiple fibres in three-dimensional space were also very slow: the 8-axonal model took approximately 2 days to be computed. This time is expected to rise dramatically with the number of fibres and with added complex ion channels. To develop a full model, thousands of such interacting fibres are needed making the brute force approach to be inadequate.

There are two possible ways to overcome this limitation. The first is to simplify the model so that complex ion channels' dynamics and spatial structure of each separate fibre is not taken into account. This could for example be achieved by the development of a bidomain model (Altman & Plonsey, 1988; Sadleir, 2010; Yin *et al.*, 2013) where

groups of fibres are treated as a uniformly distributed medium so that the membrane, extracellular and intracellular spaces occupy the same volume and are described by the same set of equations. However, the lumped bidomain approach has several shortcomings which are vital for accurate simulation of the activity of the whole nerve. First, it does not take into account the discrete fibre geometry which becomes important when fibres possess different properties or fire non-synchronously (Clark & Plonsey, 1971); second, during external stimulation, fibres lying close to the nerve periphery must reach the threshold faster than the deeper ones, which is not fulfilled in the lumped model (Altman & Plonsey, 1990); finally, the fibres are usually not uniformly distributed in the nerve as bidomain model implies.

The second approach for acceleration is the search for technical solutions to run the precise model with separate fibres more rapidly. These solutions may include the use of GPU or more efficient parallelizing involving the division of the model into several parts.

3.5 Conclusion

In this chapter, full 3D FEM models of single and multiple interacting nerve fibres were developed. The activity of the fibres was modelled using either the HH model of squid giant axon or the mammalian C fibre model. With these models, impedance changes during AP propagation were simulated under various external conditions. The simulated negative dZ were in agreement with available experimental data; positive dZ were obtained at higher frequencies. The model allows for an optimized method of EIT for unmyelinated nerves by predicting the necessary parameters of the injected current and the optimal size and position of the electrodes. By studying membrane currents during EIT current injection, the model provided a biophysical explanation of the simulated impedance changes which is of high importance for understanding the nature of observed experimental results.

Chapter 4
FEM model of a myelinated fibre

4.1 Introduction

4.1.1 Overview

The previous chapter covered the implementation of the novel approach for modelling unmyelinated fibres bi-directionally coupled with external space. The models allowed simulation of impedance changes during neuronal activity and were successfully applied for prediction of the optimal parameters of fast neural EIT providing the largest possible dZ in unmyelinated fibres. The current chapter extends the developed approach to model a mammalian myelinated fibre in order to optimise EIT for this fibre type as well as to interpret the previously obtained experimental data and to better understand the physiological origin of the observed dZ.

The existing models of myelinated fibres are discussed in section 2.3.3. Although some of the models are very spatially accurate (Halter & Clark, 1991; McIntyre *et al.*, 2002) or possess ion channels simulating realistic mammalian nodal and internodal APs (Bostock *et al.*, 1991; Howells *et al.*, 2012), none of them allows full coupling of the fibre's internal activity with external space in both directions as well as estimation of dZ during neuronal activity. The model created in this chapter includes experimentally validated ion channels, simulates realistic behaviour of the human thickly myelinated fibre (Howells *et al.*, 2012) and enables continuous measurement of its impedance during AP propagation.

4.1.2 Purpose

The general purpose of the study described in this chapter was to create an accurate FEM model of a myelinated fibre coupled with extracellular space and predict the dZ during AP propagation under various stimulation paradigms. Specific questions to be answered here were:

1. How does the impedance change depend on the following experimental parameters:
    a. Amplitude and frequency of the injected current;
    b. Signal processing specifications;
    c. size and position of the electrodes.
2. Does this agree with the previous studies?
    a. Does the model validate recent experimental recordings?
    b. Does it offer an explanation on the origin of the dZ?
    c. Does it provide results different from the recent model of unmyelinated fibres presented in Chapter 3 and the passive model (Liston *et al.*, 2012)?
3. What recommendations can be given for optimization of imaging myelinated fibres using fast neural EIT?

The results will improve the understanding of the measured impedance changes and lead to optimization the parameters of EIT for imaging in myelinated nerves, which will facilitate the development of a full nerve model with myelinated and unmyelinated fibres.

4.1.3 Experimental design

The work was divided into the following steps.

1) An accurate one-dimensional FEM double-cable model of a mammalian sensory fibre was developed. It contained ten ion channels based on the experimentally validated space-clamped model (Howells *et al.*, 2012): four at

the node and six at the internode. Realistic morphology of the fibre (Berthold & Rydmark, 1983) was implemented similarly to the one used in (McIntyre *et al.*, 2002). To match the experimental data, several geometrical (Table 4.1) and electrical (Table 4.2) parameters were modified in the new FEM model. With these changes, the conduction velocity of the fibre and the shape of membrane potential at the nodes and internodes in resting state and during excitation, matched the experimentally validated space-clamped model (Howells *et al.*, 2012).

2) The completed 1D model was incorporated into a 3D-equivalent 2D axisymmetric paradigm to form a full coupled model of the fibre with the external space, similarly to the fully coupled C fibre model developed in Chapter 3. An AP was induced at the distal end of the fibre and its propagation was simulated intra- and extra-cellularly. Two external ring electrodes were used to apply an electrical current and an additional equal electrode was to record the axonal activity with respect to ground (Figure 4.1). The effects of varying experimental parameters on measured dZ were studied and the optimal parameters were established.

3) The dZ simulated in the developed model were compared with the available experimental data on myelinated nerves.

4.2 Methods

4.2.1 Double cable FEM model of a mammalian myelinated fibre

The simulated myelinated fibre consisted of three types of sections: nodes, paranodes and internodes. This structure partly replicated the one observed by Berthold and Rydmark (Berthold & Rydmark, 1983), where authors described nodal (N), myelin sheath attachment (MYSA), fluted (FLUT) and stereotyped internodal

(STIN) segments. Compared to this full structure, the FLUT segment of the fibre modelled in this study was combined with the STIN. It is in accordance with (Stephanova & Bostock, 1995) where the FLUT region was also omitted and with the MRG model (McIntyre *et al.*, 2002) where FLUT region's properties were exactly the same as of the STIN internodal section.

The approach used for development of the model was the finite element method (FEM) which has not been used for simulation of myelinated fibres before. Previously developed compartmental models (Stephanova & Bostock, 1995; McIntyre *et al.*, 2002) utilized various forms of the finite-difference approach (FDM): the fibre was also divided into smaller parts, but these parts were modelled as passive resistors so that the necessary equations were solved only in the points connecting them; such an approach is used in NEURON software (Hines & Carnevale, 1997). However, if the purpose is to obtain a solution continuously along the fibre as well as to couple it with an external space in 3D (or, equivalently, 2D axisymmetric) in both directions, the FEM approach is desirable which utilizes nonlinear shape functions approximating the solution of the 2-nd order PDEs at any point in space (Zienkiewicz *et al.*, 1977). In addition, usage of FEM involves discretization of the spatial domain into unstructured parts thus allowing to solve models with variously shaped geometries. The model was built in COMSOL Multiphysics software in conjunction with Matlab, which allowed automatic solving of any partial differential equations using FEM.

A double-cable paradigm was used to simulate the spatial structure of the fibre (Figure 2.15). In this paradigm, the axoplasm and the periaxonal space between the axon and myelin sheath were modelled as two parallel cables, which allowed simulation of rapid propagation of APs in the internodes without representing them as perfect insulators. A double-cable model was previously used to accurately simulate temporal and spatial distribution of APs in mammalian nerve fibres as well as its various properties such as realistic AP shape, conduction velocity, behaviour in the nodes and internodes (Halter & Clark, 1991; Stephanova & Bostock, 1995; McIntyre *et al.*, 2002). The geometrical parameters of the modelled fibre were taken from an electron microscopy study (Berthold & Rydmark, 1983); they were similar to the ones used in the MRG model (McIntyre *et al.*, 2002). However, several changes had to be

made due to the transition from the previously used compartmental model to FEM (Table 4.1).

Table 4.1
GEOMETRICAL PARAMETERS OF THE MYELINATED FIBRE MODEL

Segment	Parameter	Value
Node	Length	1 µm
	Diameter	5.5 µm
	Mesh	2 el.
MYSA	Length	3 µm
	Diameter	12.7 µm
	Mesh	2 el., $l_2 = 2l_n$*
	Periaxonal space width	0.02 nm
	N of myelin lamellae	150
	Myelin thickness	2·1.65 µm
STIN	Length	1 µm
	Diameter	12.7 µm
	Mesh	10 el., symmetric, exponential**
	Periaxonal space width	0.2 nm
	N of myelin lamellae	150
	Myelin thickness	2·1.65 µm
Fibre	Length	15 cm
	Full diameter with myelin	16 µm
	Propagation velocity	65 m/s

* Size of the element adjacent to the node is 2 times smaller
** Exponential decrease towards the ends of the region, size of the largest central element is 100x size the smallest end elements

Electrical parameters from the realistic space-clamped model of the human sensory fibre (Howells *et al.*, 2012) were modified for the nodal and internodal APs as well as conduction velocity (CV) of the resultant FEM model to correspond to this space-clamped model and experimental results (Table 4.2). Nodal channels were represented by combined transient and persistent sodium (*Na*) needed for nerve excitation and regulation of subthreshold excitability; fast and slow potassium (K_{sn}, K_{fn}), Leakage (Lk_n) and pump (P_n) mainly responsible for membrane potential stabilization. At the internode there were slow and fast potassium (K_{si}, K_{fi}), hyperpolarization-activated *h-channel*, leakage (Lk_i) and pump (P_i) whose main functions were to stabilize resting

ionic fluxes as well as to regulate repetitive firing and pace-making (Christian & Togo, 1995; Lüthi & McCormick, 1998; McAlexander & Undem, 2000; Kiss, 2008).

The equations used for simulation of various segments of the fibre were directly derived from the double-cable circuit presented in Figure 2.15 using Ohm's and Kirchhoff's laws. They are discussed in the section 2.3.3 in terms of geometry dependent electrical parameters (2.16)–(2.18). Switching to geometry independent specific resistivities and capacitances, these equations transform as follows. At the nodes:

$$\frac{r_n}{2\rho_i}\left(\frac{\partial^2 V_{ax}}{\partial x^2}+\frac{\partial^2 V_m}{\partial x^2}\right)=c_n\frac{dV_{ax}}{dt}+\sum_{node} I_{ion}(V_{ax})\,; \qquad \sum_{node} I_{ion}(V_{ax})=I_{Na}+I_{K_{sn}}+I_{K_{fn}}+I_{Lk_n}+I_{P_n} \tag{4.1}$$

$$V_m=0 \tag{4.2}$$

where V_{ax} and V_m are transmembrane and transmyelin potentials, $[mV]$; c_n is specific nodal capacitance, $[\mu F/cm^2]$; r_n is the radius of the axon at the node, $[cm]$; ρ_i is the resistivity of the axoplasm, $[k\Omega{\cdot}cm]$; $I_{ion}(V_{ax})$ – ionic currents at the nodal area $[\mu A/cm^2]$, which are represented by ion channels from (Howells *et al.*, 2012). Due to absence of myelin sheath at the node, the transmyelin potential there equals zero.

At the internodal axolemma and across the myelin:

$$\frac{r_{ax}}{2\rho_i}\left(\frac{\partial^2 V_{ax}}{\partial x^2}+\frac{\partial^2 V_m}{\partial x^2}\right)=c_{ax}\frac{dV_{ax}}{dt}+\sum_{MYSA/STIN} I_{ion}(V_{ax})\,; \qquad \sum_{MYSA/STIN} I_{ion}(V_{ax})=I_{K_{si}}+I_{K_{fi}}+I_h+I_{Lk_i}+I_{P_i} \tag{4.3}$$

$$\frac{1}{\rho_i}\frac{S_{ax}}{L_m}\left(\frac{\partial^2 V_{ax}}{\partial x^2}+\frac{\partial^2 V_m}{\partial x^2}\right)+\frac{1}{\rho_{pax}}\frac{S_{pax}}{L_m}\frac{\partial^2 V_m}{\partial x^2}=c_m\frac{dV_m}{dt}+\frac{V_m}{\rho_m} \tag{4.4}$$

In the equations, c_{ax} and c_m are specific capacitances of the axon and myelin sheath, $[\mu F/cm^2]$; ρ_{pax} is the resistivity of the periaxonal space, $[k\Omega{\cdot}cm]$; r_{ax} is the radius of the

axon, [cm]; $S_{ax} = \pi r_{ax}^2$ and $S_{pax} = \pi(r_{ax} + h)^2 - \pi r_{ax}^3$ are the cross-sectional areas of the axon and peri-axonal space at MYSA and STIN segments in [cm^2], where h is the width of the periaxonal space at these regions [cm]; L_m is the full circumference length of the myelin sheath, [cm], its calculation can be found below; ρ_i is the resistivity of the axoplasm, [$kOhm{\cdot}cm$]; ρ_m is the resistivity of the myelin, [$kOhm{\cdot}cm^2$]; $I_{ion}(V_{ax})$ – internodal ionic currents, [$\mu A/cm^2$] (Howells *et al.*, 2012).

Full circumferential length of the myelin sheath was found as the sum of the monotonically rising N = 150 circles of myelin lamellae (Table 4.1):

$$\begin{gathered} L_m = 2 \cdot 2\pi \sum_{i=1}^{150} r_i = 2\pi \cdot 150\left(r_{ax} + r_{full} + h\right), because \\ \sum_{i=1}^{150} r_i = \begin{pmatrix} (r_{ax} + h) + (r_{ax} + h + h_m) + \ldots \\ + (r_{ax} + h + (150 - 1) \cdot h_m) \end{pmatrix} \\ = 150\left((r_{ax} + h) + \frac{149}{2} h_m\right) \end{gathered} \tag{4.5}$$

where factor 2 was added as the fibre contained 2 membranes per lamella. The radii of the circles rose from $r_1 = r_{ax}+h$ to $r_{150} = d_{full}/2 = 8\ \mu m$; h_m is a distance between lamellae: $h_m = (r_{150} - r_1)/150$ (Table 4.1); h is a width of the periaxonal space (Table 4.1).

Ionic currents at the nodes were as follows (Howells *et al.*, 2012):

$$\begin{gathered} I_{Na} = \frac{P_{Na} \frac{VF^2}{RT}\left(m^3 h + P_{NaP} m_p^3\right)\begin{pmatrix} S_{Na}\left([Na]_0 - [Na]_i e^{\frac{VF}{RT}}\right) + \\ + (1 - S_{Na})\left([K]_0 - [K]_i e^{\frac{VF}{RT}}\right) \end{pmatrix}}{1 - e^{\frac{VF}{RT}}} \\ I_{K_{sn}} = \bar{g}_{K_{sn}} s\left(V - V_{K_s}\right) \\ I_{K_{fn}} = \bar{g}_{K_{fn}} n^4 \left(V - V_{K_f}\right) \\ I_{Lk_n} = \bar{g}_{Lk_n}\left(V - V_{rest,n}\right) \end{gathered} \tag{4.6}$$

At the internodes:

$$\begin{aligned} I_{K_{si}} &= \bar{g}_{K_{si}} s_i \left(V - V_{K_s}\right) \\ I_{K_{fi}} &= \bar{g}_{K_{fi}} n_i^4 \left(V - V_{K_f}\right) \\ I_h &= \bar{g}_h q (V - V_h) \\ I_{Lk_i} &= \bar{g}_{Lk_i} \left(V - V_{rest,i}\right) \end{aligned} \tag{4.7}$$

Reversal potentials were calculated as:

$$V_x = \frac{ln\left(\frac{[K]_0 + S_x[Na]_0 - S_x[K]_0}{[K]_i + S_x[Na]_i - S_x[K]_i}\right)}{F/RT}, x = Na, K_s, K_f, h \tag{4.8}$$

In the equations, F – Faraday's constant, [$\mu A \cdot ms/mM$], P_{Na} – permeability of *Na* channels, [cm^3/ms]; P_{NaP} – percent of persistent *Na* channels; $[Na]_{0,i}$ and $[K]_{0,i}$ are sodium and potassium concentrations outside and inside the axon, [mM]; R – gas constant, [$pJ/mM \cdot K$]; T – temperature, [K]; S_x– selectivity of *Na, K, h* channels; $\bar{g}_{K_{sn,i}}, \bar{g}_{K_{fn,i}}, \bar{g}_{Lk_{n,i}}, \bar{g}_h$ – maximal conductances of potassium slow and fast channels, leakage and h-channel at the node and internode, [$1/(k\Omega \cdot cm^2)$]; V_{K_s}, V_{K_f}, V_h–reversal potentials of corresponding ion channels explained by (4.8), [mV]; $V_{rest,\, n/i}$ – nodal and internodal resting potentials, [mV]; m, m_p, h, s, n, s_i, n_i, q – gating variables explained by corresponding gating equations of the form (4.9) and similarly, for all other gating variables.

$$\frac{dm}{dt} = \alpha_m(V_{ax}) \cdot (1 - m) - \beta_m(V_{ax}) \cdot m \tag{4.9}$$

Coefficients $\alpha_x = \alpha_x(V_{ax})$ and $\beta_x = \beta_x(V_{ax})$ can be found in (Howells *et al.*, 2012). Initial values were found by solving (4.9) for m (and other gating variables) when $dm/dt = 0$ which designates stabilization of a gating variable in time. All the

electrical parameters of the modelled fibre included in the equations above are presented in the Table 4.2.

To accurately simulate the activity of the myelinated fibre using the FEM, the mesh must be carefully chosen across the segments of the fibre. So, the element size close to the segments' edges should have been sufficiently small so that the approximating FEM shape functions could accurately simulate transitions of the variables between these segments.

The sizes of the elements were chosen based on the convergence analysis study (Shapeev & Lin, 2009). As a result of this approach, the largest element size was determined so that if it is further decreased, the solution would remain constant. The nodal segment consisted of 2 equal elements, MYSA segments – of 2 elements with the element adjacent to the node being 2 times smaller than another one, STIN – of 10 elements symmetrically distributed around the centre of the segment so that element size exponentially decreased towards the edges, with the smallest elements being 100 times smaller than the largest element in the centre (Figure 4.1b, Table 4.1). As a result, the

Table 4.2
ELECTRICAL PARAMETERS OF THE MYELINATED FIBRE MODEL

Parameter	Value
C_n	1 μF/cm^2
C_{ax}	1 μF/cm^2
C_m	1.9 pF/cm^2
ρ_i	70 Ω·cm
ρ_{pax}	70 Ω·cm
ρ_m	2.8 MΩ·cm^2
$[K]_0$	4.5 mM
$[K]_i$	155 mM
$[Na]_0$	144.2 mM
$[Na]_i$	9 mM
V_h	-54.85 mV
$V_{Ks,f}$	-94.5 mV
V_{Na}	45.6 mV
$V_{rest,n}$	-80.3 mV
$V_{rest,i}$	-81.3 mV
T	310 K
P_{Na}	$2.27\cdot10^{-5}$ cm^3/ms
P_{NaP}	1.07
S_{Na}	0.9
S_K	0
S_h	0.097
$\bar{g}_{K_{sn}}$	109.47 mS/cm^2
$\bar{g}_{K_{fn}}$	87.58 mS/cm^2
$\bar{g}_{Lk_n}$	9.78 mS/cm^2
I_{P_n}	-170.64 μA/cm^2
$\bar{g}_{K_{si}}$	$5.81\cdot10^{-3}$ mS/cm^2
$\bar{g}_{K_{fi}}$	0.69 mS/cm^2
$\bar{g}_h$	$1.37\cdot10^{-2}$ mS/cm^2
$\bar{g}_{Lk_i}$	$1.22\cdot10^{-2}$ mS/cm^2
I_{P_i}	-0.018 μA/cm^2
S_{ax}	$1.27\cdot10^{-6}$ cm^2
$S_{pax,\ stin}$	$7.98\cdot10^{-11}$ cm^2
$S_{pax,\ mysa}$	$7.98\cdot10^{-12}$ cm^2
L_m	1.35 cm

smallest element in the STIN which was adjacent to MYSA was approximately 2 times larger than the large element in MYSA.

For validation of the developed FEM model, the experimentally validated space-clamped model (Howells *et al.*, 2012) was reconstructed in MATLAB so that the simulated APs at the node and internode could be matched to the new FEM model via adjustment of its electrical and longitudinal parameters. Also, the conduction velocity (65 m/s) was matched with the experimental datasets that report myelinated sensory fibres of similar size where it was shown to be 50-90 m/s (Boyd & Kalu, 1979; Waxman, 1980; Harper & Lawson, 1985; Castelfranco & Hartline, 2016).

To compare the excitability of the model to previously modelled (McIntyre *et al.*, 2002; Howells *et al.*, 2012) and experimental values (Yang *et al.*, 2000), the threshold tracking technique called threshold electrotonus was used. The fibre was subjected to 100 ms duration subthreshold depolarizing conditioning stimuli with the amplitude equalling 40% of threshold (defined by 1 ms pulse stimulation); 1 ms test intracellular stimuli were applied to the node each 5 ms in steps ~2% of threshold to trace the threshold during and after the long conditioning pulses.

Since the behaviour of the model depended on multiple electrical and geometrical parameters, sensitivity of the model to these parameters must have been investigated. As a result, variance-based sensitivity analysis was performed (Homma & Saltelli, 1996). It was accomplished by variation of the main model parameters by +/- 20% and calculation of the corresponding variance in the measured nodal and internodal APs (Figure 4.3a, b) at each time point, as in (Tigerholm *et al.*, 2014). The varied parameters included conductances and capacitances of the axonal membrane and myelin sheath as well as main electrical and geometrical parameters (Table 4.4). To quantify the effect of each parameter on the different phases of the recorded transmembrane potentials during rest and excitation, the total cumulative impact of each parameter into formation of nodal and internodal recordings was found over the whole period of 250 ms simulations.

4.2.2 FEM model coupled with external space

Extracellular space was added to the 1D model to simultaneously simulate AP propagation, injection of the current and recording of the resultant electric field using external electrodes.

The most commonly used approach for simulation of an active fibre and a surrounding space together includes two or three consecutive steps: first, the electric field is simulated using FEM; second, the resultant interpolated voltages are applied to the fibre; third, if necessary, the electric field originating from the fibre is recorded via external electrodes (Schiefer *et al.*, 2008; Wang *et al.*, 2018; Lubba *et al.*, 2019; Pelot *et al.*, 2019). This approach was not suitable for our purpose due to complex interaction of injected current with nonlinear ion channels: double-sided coupling was necessary so that the external space can affect the fibre while the fibre can affect the external space.

The model utilizing this coupling-feedback system approach was developed for the unmyelinated fibre in the previous chapter where its detailed description is presented; the same approach was applied to the myelinated model in the current chapter. As in the case of the study in Chapter 3, a 4-electrode impedance measurement paradigm was simulated, which reproduced the setup implemented in a series of experiments of recording impedance changes in unmyelinated crab leg nerves using a linear electrode array (Holder, 1992; Gilad *et al.*, 2009; Oh *et al.*, 2011; Aristovich *et al.*, 2015). The setup of the model also closely replicated the ones used for *in vivo* imaging of myelinated fibres inside rat sciatic nerve (Aristovich *et al.*, 2018) and sheep's recurrent laryngeal nerve (Chapman *et al.*, 2019). As in the latter study, AC in the model was applied through two ring external electrodes placed longitudinally along the nerve. Identically to both experiments, APs were induced at the end of the axon by bipolar stimulation and voltages were measured by the electrode placed before the injecting ones with respect to ground (Figure 4.1).

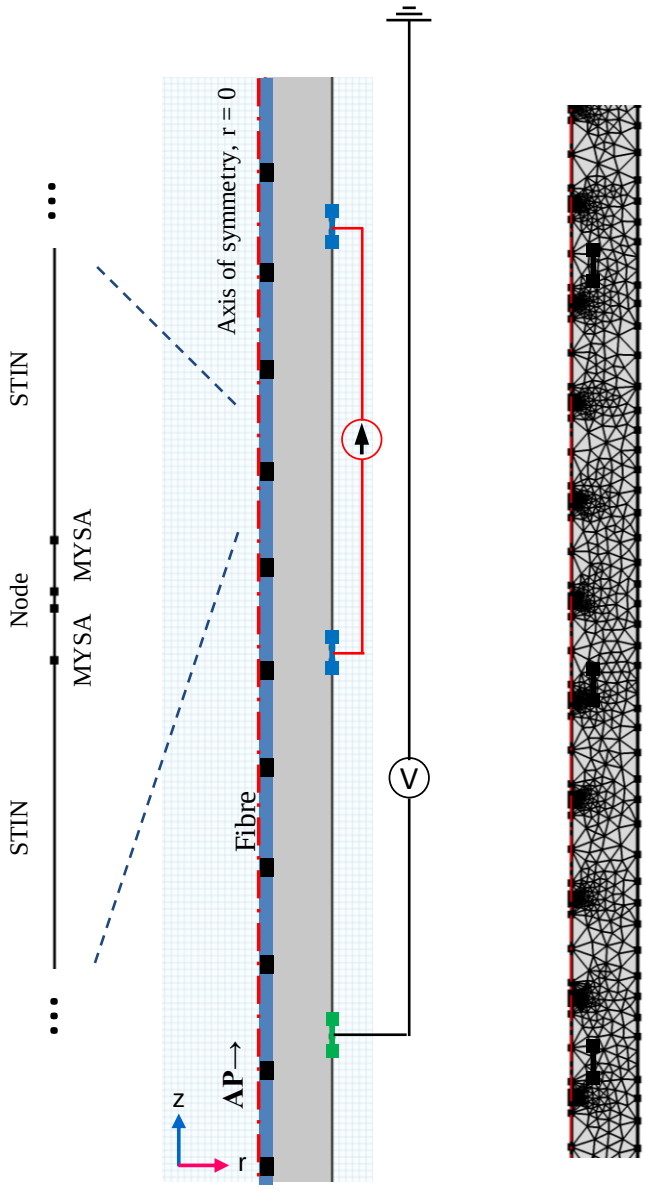

Figure 4.1 Geometrical structure and FEM mesh of the developed myelinated fibre model.
(a) The 2D axisymmetric geometry of the model. The fibre is depicted by a blue line with black nodal and MYSA regions, the axis of symmetry is shown by the red dash-dotted line. The AP was induced from the end of the fibre; DC or AC were applied through two external electrodes (blue) placed 5.6 cm and 6.2 cm from the axon's end; the electric field was recorded by an external electrode (green) placed before the injecting ones, 5 cm from the proximal end of the fibre (Table 4.3). A magnified image of the fibre in the region around the node is shown on the left; its correspondence to the 2D axisymmetric model is depicted by the blue dashed lines;
(b) Triangular FEM mesh of the model combined with the nonregular mesh of the fibre. Elements' sizes are provided in the section 4.2.1 and Table 4.1.

The external space was modelled as a cylinder (rectangle in 2D axisymmetric space) (Figure 4.1a) with the constant electrical conductivity of an extracellular

medium equalling 10 *mS/cm* (Elia & Lamberti, 2013). External ring-shaped electrodes of 0.1 cm width and 0.6 cm diameter located on the boundary of the cylinder were used for current injection and activity recording; the recording electrode was placed 5 cm from the AP initiation point; the injecting ones were at 5.6 and 6.2 cm (Figure 4.1a). 2-D axisymmetric paradigm, which for unmyelinated fibre was shown to provide the same results as the corresponding 3D model (Chapter 3), was used to accelerate computations. The fibre was 1-dimensional, which included intracellular, extracellular and periaxonal spaces as well as myelin. The model was grounded at the distal end only so that the current cannot propagate along the fibre in the backward direction which causes artefacts in dZ measurements (Aristovich *et al.*, 2015).

The equations for simulation of the external space were similar to the model developed in Chapter 3. However, their complexity increased due to non-uniformity of the fibre, which required different constants depending on the segment simulated.

First, volume conduction in the extracellular space was simulated with the Laplace's equation (2.22). Then, the main fibre equations (4.1), (4.3) and (4.4) were transformed by addition of external stimulation for each compartment represented by the activating function (2.24); these equations can also be obtained by applying Kirchhoff's laws to the double-cable circuit in Figure 2.15.

$$\begin{aligned}
&\frac{r_n}{2\rho_i}\left(\frac{\partial^2 V_{ax}}{\partial x^2}+\frac{\partial^2 V_m}{\partial x^2}+\frac{\partial^2 V_e}{\partial x^2}\right)=C_n\frac{dV_{ax}}{dt}+\sum_{node} I_{ion}(V_{ax});\\
&\frac{r_{ax}}{2\rho_i}\left(\frac{\partial^2 V_{ax}}{\partial x^2}+\frac{\partial^2 V_m}{\partial x^2}+\frac{\partial^2 V_e}{\partial x^2}\right)=C_{ax}\frac{dV_{ax}}{dt}+\sum_{MYSA/STIN} I_{ion}(V_{ax});\\
&\frac{1}{\rho_i}\frac{S_{ax}}{L_m}\left(\frac{\partial^2 V_{ax}}{\partial x^2}+\frac{\partial^2 V_m}{\partial x^2}+\frac{\partial^2 V_e}{\partial x^2}\right)+\frac{1}{\rho_{pax}}\frac{S_{pax}}{L_m}\left(\frac{\partial^2 V_m}{\partial x^2}+\frac{\partial^2 V_e}{\partial x^2}\right)=\\
&=C_m\frac{dV_m}{dt}+\frac{V_m}{\rho_m}
\end{aligned} \tag{4.10}$$

The constant sinusoidal current was applied to the external injecting electrodes (3.3). The boundary conditions were the same as for the unmyelinated fibre described in Chapter 3 in (3.9)–(3.10), the initial condition for external space was the same as for the unmyelinated models (Chapter 3): V_e = 0; the initial conditions for the fibre

were obtained by setting $dX/dt = 0$ for a gating variable X, as explained under equation (4.9). The flux of the transmembrane current from the nodal or myelin segments (MYSA and STIN) was modelled the same way as through homogeneous unmyelinated fibre (3.10):

$$\begin{aligned} I_n|_\Gamma &= \sigma_e \nabla V_e \cdot \boldsymbol{n} = C_n \frac{dV_{ax}}{dt} + \sum_{node} I_{ion}(V_{ax}) \text{, on } \Gamma_{node} \\ I_m|_\Gamma &= \sigma_e \nabla V_e \cdot \boldsymbol{n} = C_m \frac{dV_m}{dt} + \frac{V_m}{\rho_m} \text{, on } \Gamma_{myelin} \end{aligned} \tag{4.11}$$

The scheme of operation of the developed coupled model repeated the one in Chapter 3 (Figure 3.2) and included two simultaneous simulations – with and without the injected current. Simulation of electric field generated by the fibre when no current was injected (V_e^0) was done via additional 1D and 2D-axisymmetric geometries; their difference with the electric field simulated with the injected current (V_e) was applied to the nerve fibre (V_e-V_e^0) at each time step. Finally, the resultant transmembrane current was coupled from the fibre to the main geometry.

A triangular mesh, containing 41,000 elements, was constructed in the axisymmetric model so that the fibre formed a continuous mesh within the volume. This means that the lengths of the sides of the triangles adjacent to the fibre were equal to the sizes of the mesh elements in the fibre (Figure 4.2b, Table 4.1).

In the developed models, equations representing the fibre (4.1)–(4.9) together with the ones simulating external space and its coupling with the fibre (2.22), (4.10), (4.11) were solved simultaneously for each time step with respect to V_{ax}, V_m and V_e. For this, an adaptive backward differentiation formula (BDF) was utilized in conjunction with a parallel sparse direct solver (PARDISO) to solve linear equations in the spatial domain (Schenk & Gärtner, 2004). Convergence was tested by tracing deviation of the relative norm of the residual against the specified tolerance, the same way as for the unmyelinated fibre model discussed in Chapter 3. The tolerance for the myelinated fibre model developed in this Chapter was set to 0.0001.

Using the voltages recorded during the simulations, changes in the impedance of the system (dZ) were calculated. Details on the simulations setup and signal processing

are given in the next section. The COMSOL model files for the complete myelinated fibre model are provided in the EIT-lab GitHub repository at https://github.com/EIT-team/Myelinated-fibre-model.

4.2.3 Simulation setup and signal processing

Application of electric current and recording of external voltage was continuously performed in all simulations. Each simulation lasted 100 milliseconds and the AP was initiated at t = 50 ms to let the transmembrane and transmyelin potentials stabilize (Figure 4.3). The recording sampling rate was 20 kHz when DC and low-frequency AC (225, 625, 1025, 2000 Hz) were applied; it was 100 kHz at all other AC frequencies.

The first step was to study how the impedance of the system changes depending on the amplitude and frequency of the applied currents. For that, the maximum amplitudes of DC and 6 kHz AC current were found at which proportionality was maintained, as expected from the Ohm's law. This revealed the optimal amplitude, which was used in all subsequent simulations; higher currents would modify physiology of the nerve causing artefacts in dZ measurements while too small currents may become comparable to the noise brought by modelling errors or instrumentation (Holder, 2004*a*). Thus, simulations were performed at 1.3 – 50.2 µA at DC and similarly at 6 kHz in the range of 1.3 – 1256 µA.

Using the chosen amplitude, DC and AC at a range of frequencies (225 Hz, 625 Hz, 1025 Hz, 2, 4, 6, 8, 10, 12 and 15 kHz) were sequentially applied through the injecting electrodes and the voltages were recorded via the recording electrode with respect to ground (Figure 4.1). The dZ was measured in terms of the recorded voltage, the same as in the model of the unmyelinated fibre (3.1), (3.2).

Signal processing for extraction of impedance changes from the recorded voltages was accomplished for two scenarios (Figure 4.2). In the first case, it included the following (Figure 4.2a). When AC was applied, the two sequential simulations in phase (0, $\pi/4$, $\pi/2$, $7\pi/8$, $5\pi/8$, $19\pi/20$) and in antiphase ($-\pi$, $-3\pi/4$, $-\pi/2$, $-\pi/8$, $-3\pi/8$, $-\pi/20$) locked to the time of AP initiation were carried out at each frequency. This was

done for validation of the obtained dZ and removal of the artefacts appearing due to coherence of AC with the AP. The resultant signals were 1) subtracted, which led to cancellation of the AP and doubling of the dZ; 2) band-pass filtered around the carrier frequency with the 1st order Butterworth filter in forward and inverse directions, to eliminate the AP artefacts left after subtraction; 3) demodulated, using the absolute of Hilbert transform and 4) normalized in respect to baseline, to obtain normalised dZ in percent. In the simpler DC case, the signals simulated with the reversed polarity of the current were subtracted and normalised.

dZ measurements in the case when AC was applied, were also performed when subtraction (*step 1*) of the signal processing was omitted (Figure 4.2b, case 2). In this case, phase and antiphase recordings were not subtracted, and the original signal containing extracellular AP was band-pass filtered and demodulated. This was done in order to check the feasibility of real-time imaging in experimental conditions: in the case 2 only one recording was necessary to obtain a dZ while subtraction demanded in- and anti-phase measurements to be performed.

In contrast to the previous modelling (Chapter 3) and experimental studies (Aristovich *et al.*, 2018; Chapman *et al.*, 2019) where constant bandwidths were used across all injected AC frequencies, they were varied in this study to find the optimal one at each frequency. Since the durations of simulated APs were short (< 1 *ms*) (Figure 4.3) and in order to have sufficient time resolution of the obtained dZ signal – high bandwidths were better to be used during the band-pass filtering step of signal processing.

In fact, dZ measured at DC possesses the full natural frequency band, which reflects the real apparent dZ; it could be reached at a given AC frequency if time resolution is sufficient and a full dZ bandwidth is taken into account when processing the signal at this frequency. On the other hand, it is not always possible to choose bandwidths covering the characteristic frequency of the real dZ (0-8 kHz, Figure 4.7). The first reason for this is that the carrier frequency has to be high in order to support this high bandwidth. Second, if recordings with in- and anti-phase currents were not subtracted and the frequency of the carrier is sufficient, necessary bandwidth would start to overlap with the characteristic frequency band of the AP (0–3 kHz, Figure 4.7), which brings artefacts into measurements (Figure 4.9a). Finally, as the membrane consists of

parallel resistances and capacitance, the dZ will decrease with the frequency of the measuring current. All of these factors contribute to the measured dZ, so that optimal values of AC carrier frequency and bandwidth must be found.

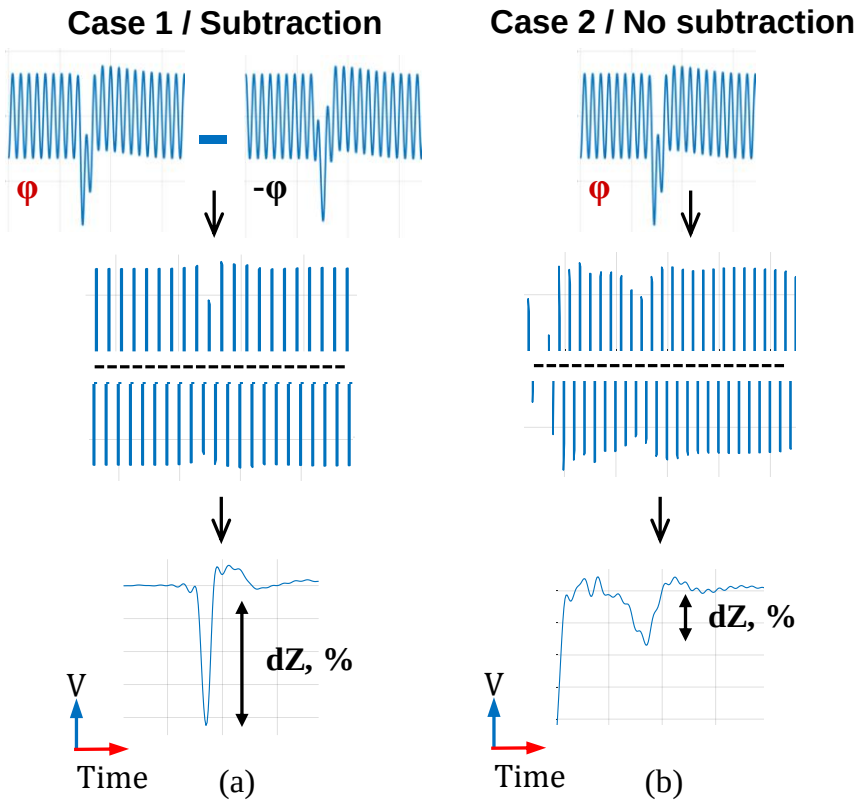

Figure 4.2 Signal processing to extract the dZ in the created myelinated fibre model.
It was performed for two cases: (a) with and (b) without subtraction of signals simulated with the in-phase and anti-phase injected AC (presented at the top of the figure). After this step, the signal was band-pass filtered (top and bottom parts of the resultant sine wave are in the middle of the figure), demodulated and normalized (at the bottom of the figure). The 2nd case without subtraction was implemented to test the level of reduction in the dZ amplitude if the second anti-phase recording was not performed so that the feasibility of real-time imaging could be studied.

At each frequency starting from and higher than 625 Hz, dZ was obtained at a range of bandwidths from 500 Hz up to (*f* – *500*) Hz with 100 Hz steps, where *f* is the frequency of the applied AC. This was repeated for each phase-antiphase pair and the optimal bandwidth was determined as the one that maximizes the value Δ = *(dZ – 3 standard deviations of dZ)*. Three standard deviations of dZ (obtained by measuring at different phases of injected AC) were chosen because: 1) the magnitude of the obtained dZ increases with bandwidth due to presence of the high frequency components in it;

2) the standard deviation of dZ also increases because the artefact is phase dependent and the AP frequency band (0–3 kHz, as seen from the power spectral density of the modelled AP in Figure 4.7) starts to overlap with the chosen bandwidth. The above procedure was repeated in situations when subtraction of in-phase and anti-phase signals (*step 1* of the signal processing) was omitted (Figure 4.2b), which resulted in the errors becoming much larger: even very small overlap in the bandwidth and the AP frequency band brings huge errors to measurements. Therefore, this overlap should be minimized by decreasing the utilized bandwidths that then leads a reduction in the recorded dZ.

Table 4.3
GEOMETRICAL PARAMETERS OF THE COUPLED MODEL

Parameter	Value
Diameter of the electrodes / surrounding volume, D_{el}	0.2 cm*; 0.2 – 2 cm
Width of the electrodes, H_{el}	0.02 cm; 0.01 – 0.1 cm
Distance between recording and injecting electrodes, Δx_R	0.6 cm; 0.1 – 5 cm
Distance between injecting electrodes, Δx_I	0.6 cm; 0.1 – 5 cm

* First number in each row is the value used by default; range of values shows a variation of the parameter (see Figure 4.10).

Further, the locations and sizes of the electrodes were varied to study their effect on the recorded dZ, as has previously been done for the unmyelinated model in Chapter 3. The varied parameters included the electrodes (and surrounding volume) diameter D_{el}, electrodes width H_{el}, distance between recording and injecting electrodes (Δx_R) and distance between injecting electrodes (Δx_I) (Table 4.3). Variation was done at DC and 6 kHz with the optimal bandwidth found during the study (Figure 4.8).

Finally, to understand the origin of the measured dZ, membrane conductances, the flow of applied currents through the membrane and the extracellular space were studied. The gradient field of the current was plotted at DC so that its direction could be seen in any point of the external space. It was done in two time points – when negative and positive dZ reached maximum (50.7 and 51.5 ms, Figure 4.6a, Figure 4.9a). Conductances and membrane currents were measured along 2 cm of the fibre under the electrodes at 4.8 – 6.8 cm from the point of AP initiation.

4.3 Results

4.3.1 Double cable FEM model of a mammalian myelinated fibre

The developed one-dimensional FEM model was validated against the existing experimentally validated space-clamped model (Howells *et al.*, 2012) so that the shape and amplitude of APs at the node and internode in these models matched each other (Figure 4.3). Conduction velocity in the model equalled to 65 *m/s* which is in the experimental range for the myelinated fibre of similar properties (Boyd & Kalu, 1979; Waxman, 1980; Harper & Lawson, 1985; Castelfranco & Hartline, 2016). The duration of the AP at the node was equal to approximately 1 ms, while depolarization at the internode lasted around 20 ms; the amplitudes at the node and internode were ~110 mV and 5 mV respectively (Figure 4.3). APs at various segments of the fibre were similar to the results obtained in the previous modelling studies (Stephanova & Bostock, 1995; McIntyre *et al.*, 2002; Lubba *et al.*, 2019). Also, nodal and extracellular APs (Figure 4.3a, d) were in agreement with the experiments (Bostock *et al.*, 1991; David *et al.*, 1995); no experimental data is available for transmyelin potentials and internodal values of transaxonal potentials. The spatial length of the AP was ~12 cm (Figure 4.3e) which was similar to the values obtained in (Stephanova & Bostock, 1995; Stephanova, 2001).

The model's threshold electrotonus was similar to the ones obtained in recent modelling and experimental studies (Yang *et al.*, 2000; McIntyre *et al.*, 2002; Howells *et al.*, 2012). It included transient threshold changes following the start (40 to 49% threshold reduction at 50-70 ms) and the end of the stimulus (-1 to -10% reduction at 150-170 ms) (Figure 4.4).

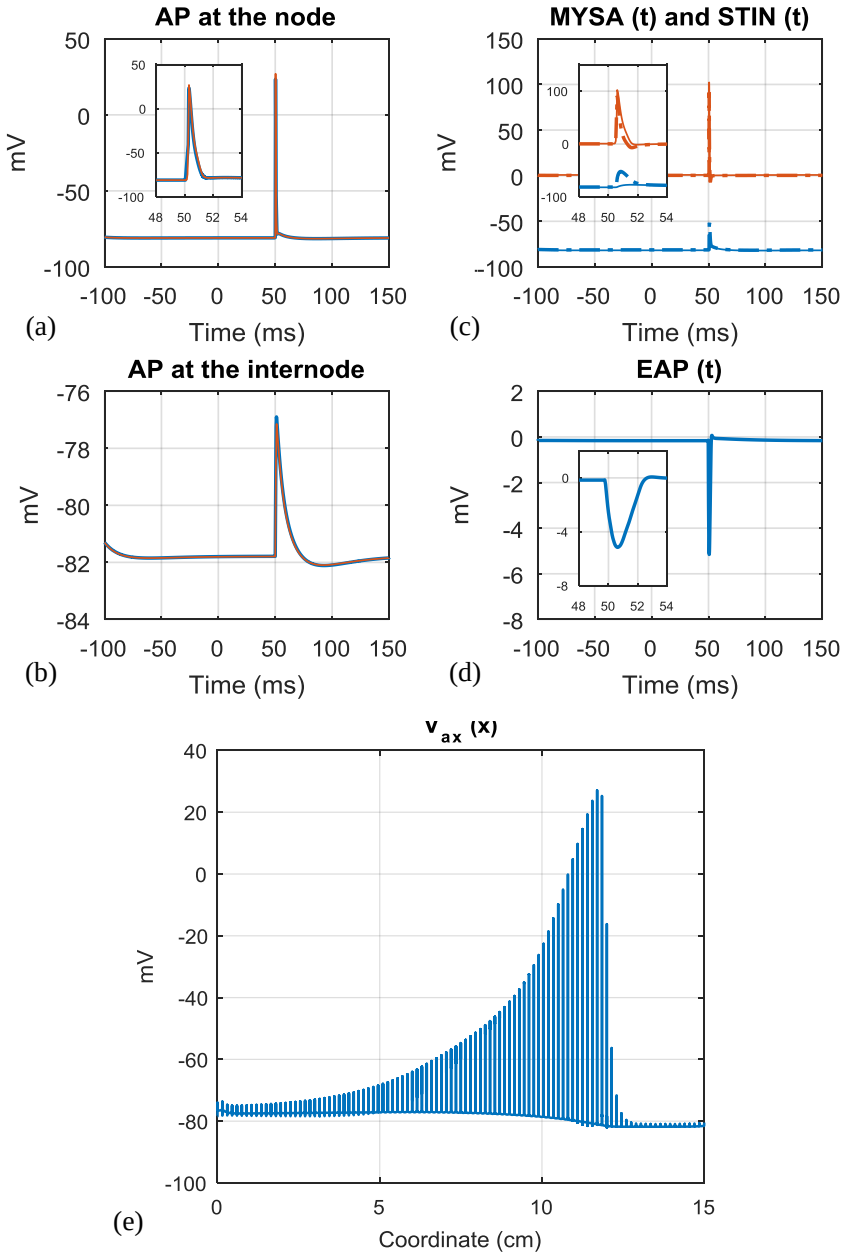

Figure 4.3 Action potentials in time (a)-(d) and along the length (e) simulated with the developed model and compared to the validated space clamped model.
250 ms long simulations are presented to show variations in resting potential preceding and following the AP. Magnified plots of 6 ms durations are embedded into (a), (c), (d) to better reveal the shapes of the depicted signals.
(a) Transmembrane potentials measured at the centre of the nodal region simulated with the developed FEM model (red lines) in comparison with the validated space-clamped model (Howells *et al.*, 2012) (blue lines).
(b) Transaxonal potential measured at the centre of internodal region (red) compared with the validated model (blue);
(c) Transaxonal (blue) and transmyelin (red) potentials at the MYSA (dashed lines) and STIN (solid lines) regions;
(d) AP recorded with the external electrode in respect to ground, EAP (t);
(e) Transaxonal potential along the fibre length, V_{ax} (x).

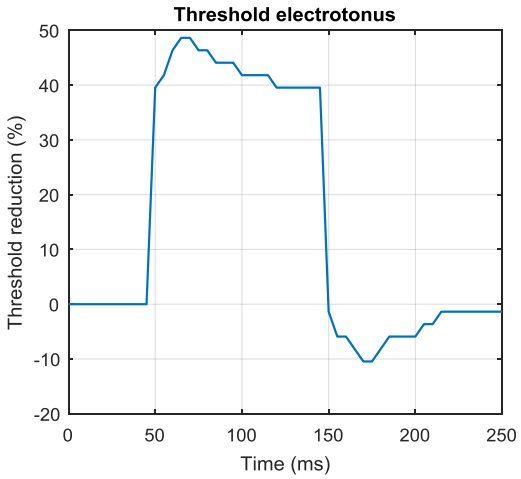

Figure 4.4 Excitability of the fibre measured with threshold electrotonus.
It was simulated in two steps: 1) a long 100-ms conditioning stimulus with the 40% of threshold amplitude was applied; 2) threshold for AP initiation was found by application of 1-ms long stimuli to the node every 5 ms during and after the conditioning stimulus. The graph is not smooth because short 1-ms threshold determining stimuli were applied in steps of approx. 2% of threshold (~25 pA).

The sensitivity analysis showed that the modelled nodal and internodal APs were most sensitive to permeability of the sodium channels P_{Na}, slow nodal and fast internodal potassium conductances $\bar{g}_{K_{sn}}$ and $\bar{g}_{K_{fi}}$, nodal pump I_{P_n}, axoplasm and myelin resistivities ρ_i and ρ_m, and diameter of the axon d_{ax} (Table 4.4, Figure 4.5). Conversely, the APs were insensitive to internodal leakage conductance $\bar{g}_{Lk_i}$, resistivity and width of periaxonal space ρ_{pax}, h and h_{mysa} as well as the diameter of the node d_n with the contribution to the variance in nodal or internodal APs less than 0.01%.

All the phases of the recordings including rest, depolarization and hyperpolarization were found to be

Table 4.4
SENSITIVITY ANALYSIS

Parameter	Nodal AP, %	Internodal AP, %
C_n	1.98	0.02
C_{ax}	0.19	2.92
C_m	1.39	0.01
ρ_i	17.06	0.32
ρ_{pax}	0.06	< 0.01
ρ_m	21.49	1.51
h	0.01	< 0.01
h_{mysa}	0.02	< 0.01
d_n	< 0.01	< 0.01
d_{ax}	38.23	2.66
d_m	0.02	< 0.01
P_{Na}	15.73	19.05
$\bar{g}_{K_{sn}}$	1.62	17.41
$\bar{g}_{K_{fn}}$	0.15	0.63
$\bar{g}_{Lk_n}$	0.03	0.03
I_{P_n}	1.03	12.89
$\bar{g}_{K_{si}}$	0.01	0.08
$\bar{g}_{K_{fi}}$	0.89	38.96
$\bar{g}_h$	0.05	1.98
$\bar{g}_{Lk_i}$	< 0.01	0.06
I_{P_i}	0.04	1.48

influenced by multiple parameters (Figure 4.5). At the same time, the diameter of the axon d_{ax} had the major contribution to the variance during short stages of the AP (Figure 4.5, right). This was because d_{ax} was explicitly and implicitly (through S_{ax}, S_{pax} and L_m) present in the main model equations (4.1)–(4.5) and thus significantly affected the simulated signals. Specifically, variation in d_{ax} (together with ρ_i and ρ_m) strongly influenced the conduction velocity which led to a time-shift of the AP signals recorded at the same point on the fibre and therefore to an increase in the computed variance.

The accomplished first order sensitivity analysis did not take into account interactions between different variables – by variation of two or more parameters simultaneously, the effect may be different from the sum of the effects of consecutive variations of these parameters. To study the effect of interaction on the variance, a total effect sensitivity analysis (Homma & Saltelli, 1996) would need to be carried out in the future.

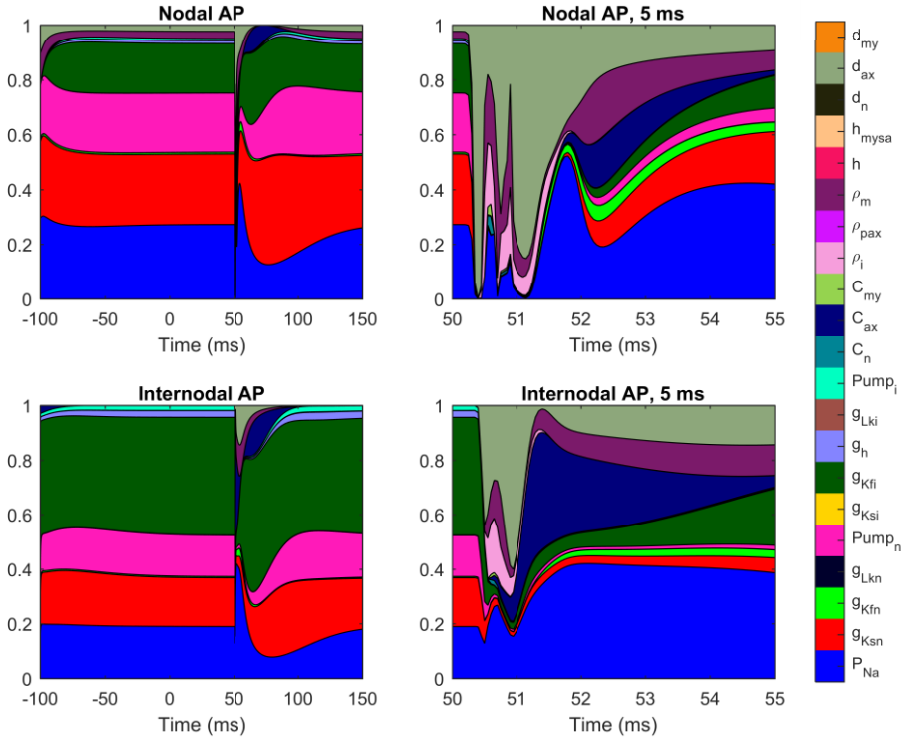

Figure 4.5 First order sensitivity analysis in respect to the main parameters of the model. The shaded areas are normalized variances of the nodal (top) and internodal (bottom) APs at each time point corresponding to the parameters varied by +/- 20%. The list of the varied parameters together with the corresponding colours is presented on the right of the graph and in the Table 4.4. Whole simulations (0-250 ms, as in Figure 4.3a, b) are presented on the left, and the magnified AP part (50-55 ms) – on the right.

4.3.2 Full model of a myelinated fibre coupled with external space

1. Optimal current amplitude

The simulated dZ were linear with the injected direct currents from 1.3 – 12.6 µA: the shape and percentage dZ stayed the same in this range (Figure 4.6a). dZ became nonlinear at higher currents which change the normal behaviour of the membrane; for example, it can be seen at 50.2 µA (Figure 4.6a). The upper safe range limit increased at higher frequencies: for example, at 6 kHz dZ linearity remained up to 125 µA (Figure 4.6b). Thus, the membrane was not affected by currents of up to 12.6 µA at all frequencies, therefore this amplitude was chosen for all further simulations.

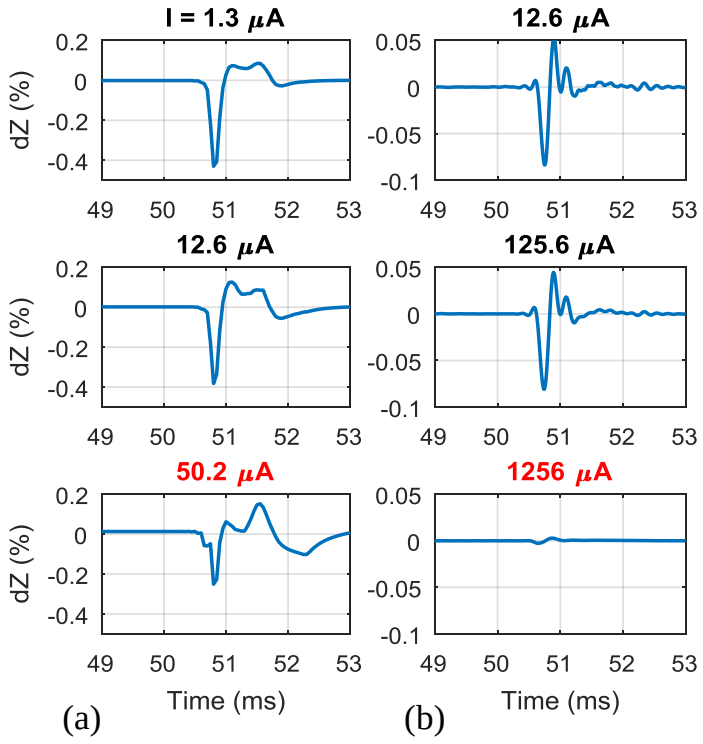

Figure 4.6 dZ of the modelled myelinated fibre at different current amplitudes measured at (a) DC; (b) 6 kHz.
Currents at which dZ become nonlinear are shown with titles highlighted in red. Time markers during simulation: AP excitation – 50 ms from the start; AP passes under the recording electrode – 50.8 ms; AP reaches the end of the fibres in 2.3 ms after initiation.

2. Optimal current bandwidth and frequency

The power spectral density of dZ included the significant band of up to 7-8 kHz (Figure 4.7). Therefore, the filtering bandwidth used during signal processing for subsequent demodulation (section 4.2.3) could not be significantly less than 2 kHz that restricted the lower limit of the carrier frequencies.

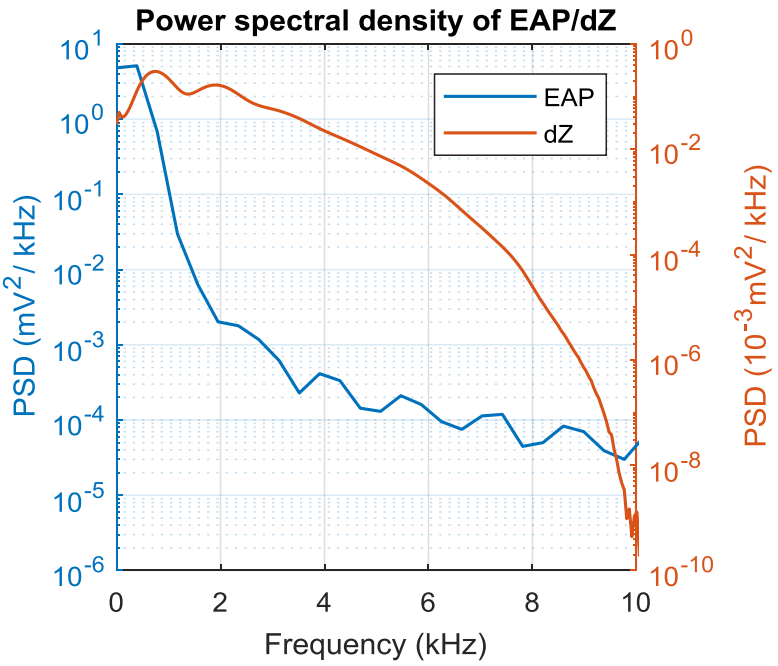

Figure 4.7 Power spectral density (PSD) estimate of the simulated EAP (Figure 4.3d) and dZ at DC (Figure 4.9a).
PSD of dZ simulated at DC demonstrates the frequency band of a natural dZ; it could be reached at AC if a perfect carrier frequency and bandwidth are chosen (see text).

When signal processing involved the subtraction of in-phase and anti-phase recordings, the optimal bandwidths to obtain the largest signal were found to increase with the carrier frequency from around 500 Hz at 4 kHz AC to 4.5 kHz at 6 kHz AC, 7.5 kHz at 8 kHz AC, 8.1 kHz at 10 kHz AC, 9 kHz at 12 kHz AC and 10.6 kHz at 15 kHz AC (Figure 4.8, Table 4.5).

When no AP subtraction has been performed, significant dZ could only be recorded above 6 kHz (Figure 4.8, Figure 4.9). The optimal bandwidth increased from 0.9 kHz at 6 kHz AC to 1.1 kHz at 8 kHz AC, 2.1 kHz at 10 kHz AC and 3.9 kHz at 12 kHz AC; but it decreased to 1.8 kHz at 15 kHz AC (Figure 4.8, Table 4.5).

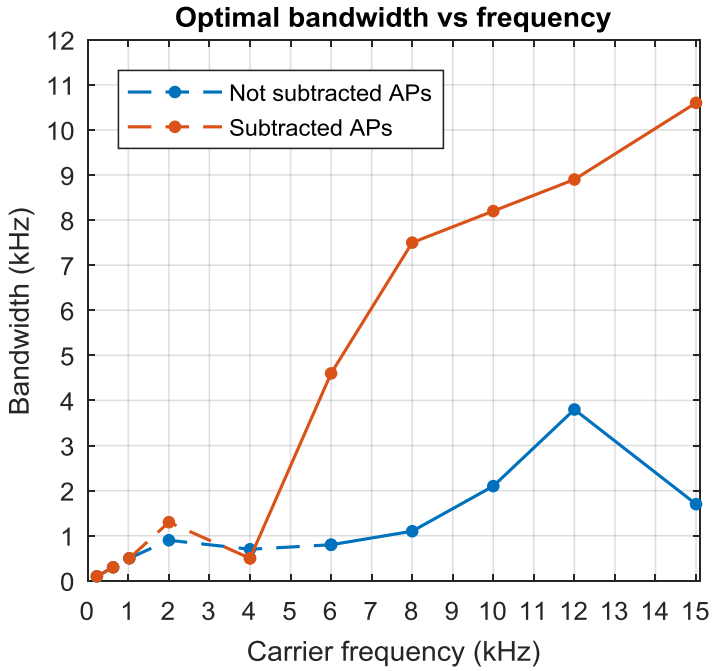

Figure 4.8 Optimal bandwidths providing the highest reliable dZ signal for each injected AC frequency.
It was calculated when the value (dZ – 3 standard deviations) reached a maximum. The case when phase-antiphase subtraction was performed as a 1st step of signal processing is shown in red, the alternative case is depicted in blue. Dashed lines show that no reliable impedance changes could be obtained at < 4 kHz for the subtraction case or < 6 kHz for the case when no subtraction was accomplished.

For the initially chosen geometrical parameters (Table 4.3), significant negative dZs simulated at optimal bandwidths when subtraction was performed were ($\cdot 10^{-2}$): -45±4% at DC, -0.7±0.3%, -9.6±1.5%, -11.4±0.9%, -8.0±0.9%, -6.3±0.4%, -5.4±0.6% at 4, 6, 8, 10, 12 and 15 kHz (Table 4.5). Significant dZ increases were also observed ($\cdot 10^{-2}$): 6±4% at DC and 4.2±1.5%, 4.5±0.9%, 1.8±0.9%, 1.3±0.4%, 1.3±0.6% at 6, 8, 10, 12 and 15 kHz (Figure 4.9b). When subtraction was not performed, significant dZ decreases were ($\cdot 10^{-2}$): -1.9±0.9%, -1.9±0.4%, -3.1±0.6%, -4.4±0.6%, -2.3±0.4% at 6, 8, 10, 12 and 15 kHz; dZ increases were observed to be significantly different from zero at 10, 12 and 15 kHz with the values of 0.8±0.6%, 1.4±0.6%, 0.6±0.4% $\cdot 10^{-2}$ respectively (Figure 4.9c, Table 4.5). The analysis without subtraction was not available at DC as this requires different polarities of current.

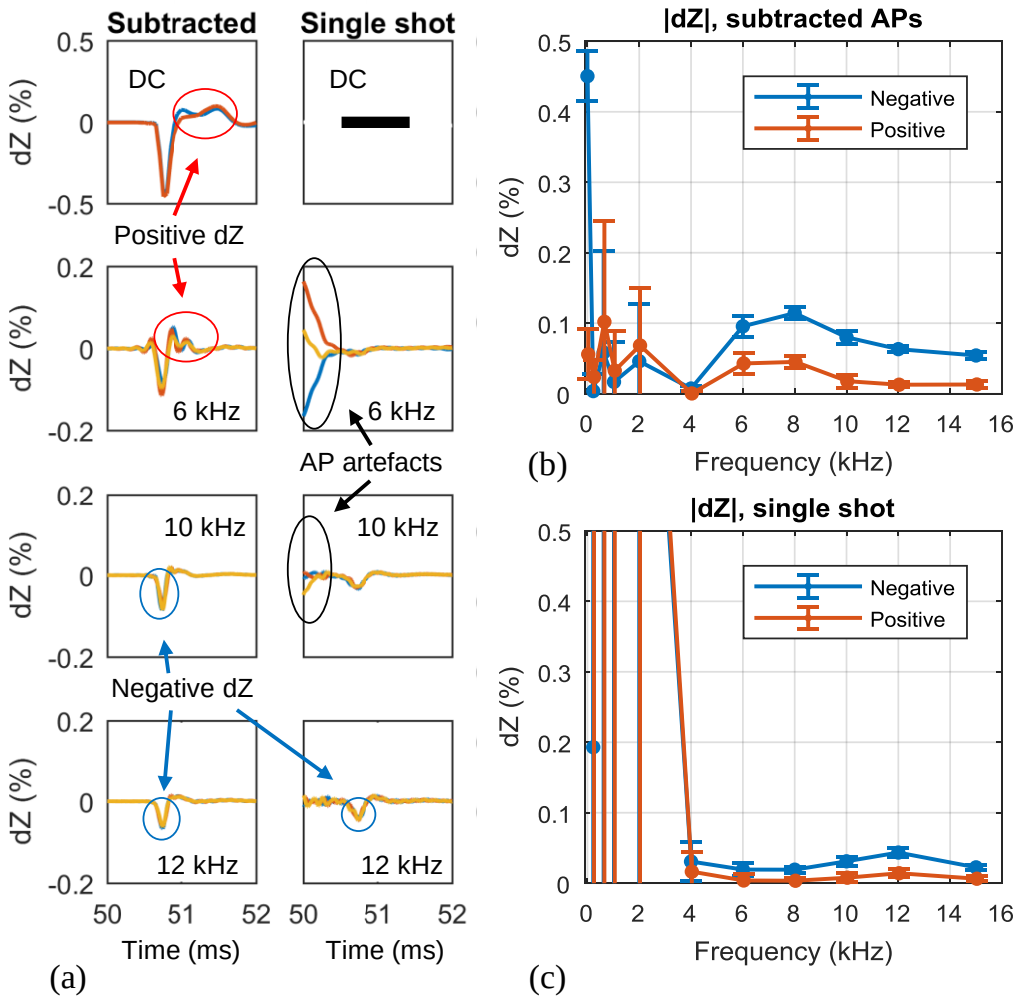

Figure 4.9 Dependence of the dZ of myelinated fibre on frequency of the applied current.
(a) Examples of dZ at DC, 6, 10 and 12 kHz for the subtraction and single shot cases of signal processing (Figure 4.2). It was not possible to measure dZ at DC without AP subtraction. Lines of different colours represent dZ recorded at different phases or different polarity (for DC) of the injected current. Examples of negative dZ are highlighted by blues circles, positive ones – by red circles; the artefacts arising from APs in a single shot case are highlighted by black circles;
(b) Absolute dZ vs. frequency at optimal bandwidths (Figure 4.8) for the case when in- and anti-phase AP were subtracted during signal processing;
(c) Absolute dZ vs. frequency at optimal bandwidths when no subtraction was performed.
Blue lines designate impedance decrease (negative change), red – impedance increase (positive change). Error bars are standard deviations calculated for the dZ simulated at different phases of the current (AC) and at different polarities (DC). Instability in (c) below 4 kHz is observed as it is impossible to demodulate dZ from the carrier frequency significantly lower than the characteristic frequency band of the dZ itself (Figure 4.7).

3. Influence of the size and position of the electrodes

At both DC and 6 kHz, when distances between injecting (Δx_I) and the recording and injecting electrodes (Δx_R) were increased, the positive and negative dZ decreased (Figure 4.10a, b).

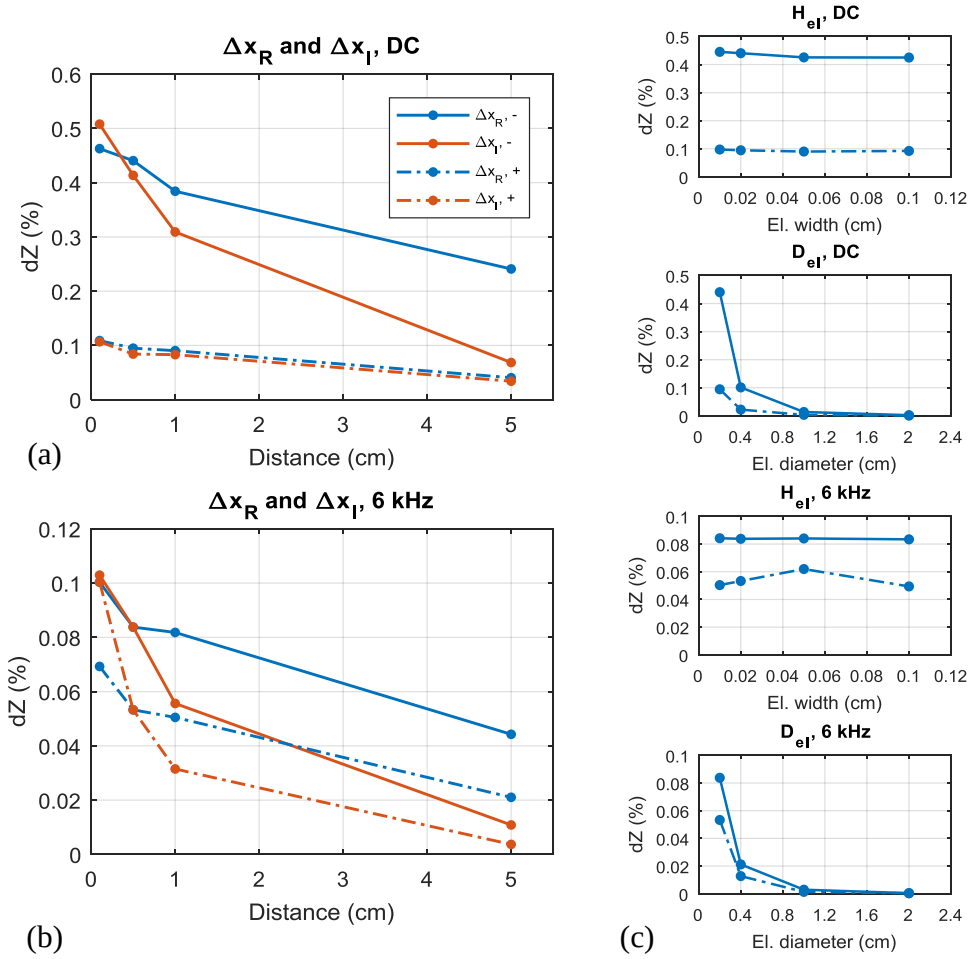

Figure 4.10 Dependence of absolute dZ onsize and position of electrodes in the developed model of the myelinated fibre. dZs were obtained with subtraction of APs (Figure 4.2, case 1).
(a), (b) Dependence of dZ on distance between the recording and injection electrodes (Δx_R) and between injecting electrodes (Δx_I) at (a) DC and (b) 6 kHz with bandwidth = 4.6 kHz (optimal for 6 kHz AC, Figure 4.8). dZ vs Δx_R is depicted with blue lines, Δx_I – with red lines. Negative dZ are shown by full lines, positive – by dashed lines.
(c) Dependence of dZ on width (H_{el}) and diameter (D_{el}) of the electrodes. Top two graphs are for DC, bottom graphs – for 6 kHz AC. Negative dZs are shown by solid lines, positive – by dashed lines.

At DC, the maximum negative dZ of -0.47% and -0.5% was simulated at Δx_R = 0.1 cm and Δx_I = 0.1 cm; the maximum positive dZ was about 0.1% at Δx_I or Δx_R = 0.1

cm. At 6 kHz, the negative maximum values were -0.1% at 0.1 cm Δx_I or Δx_R, the positive ones were 0.07% and 0.1% at the same electrodes' locations. The absolute dZ values significantly decreased with increasing diameters (D_{el}) of the electrodes up to 2.0 cm but stayed close to constant when increasing their widths (H_{el}) up to 0.1 cm (Figure 4.10c).

4. Biophysical origin of the recorded dZ

During the propagation of AP, the overall membrane conductance increased significantly (Figure 4.11a): the main contribution was made at the node where it increased from 0.025 to 0.57 S/cm^2 (~23 times). The total increase was approximately the same: compared to the nodal values, the contribution of the internodal axolemma and myelin was negligible. This conductance increase could explain the dZ decrease which was being measured externally and occurred at the same time (seen in Figure 4.6 and Figure 4.9a). The total change in conductance induced by the injected EIT direct current (Figure 4.11b) was approximately -2.1 *mS/cm^2*, which was less than 0.5% of the overall change in conductance during an AP. It can therefore be inferred that the injected current did not significantly interfere with the membrane and affect the dZ measurements.

As the largest conductance change during AP was at the nodal regions (Figure 4.11a), the flow of the nodal currents (Figure 4.11c), as well as the injected EIT current through nodes (Figure 4.11d) were studied. The main contributors to the nodal currents were the ionic currents whose absolute values rose from ~0 to 18 mA/cm^2 (Figure 4.11c). The flow of the applied DC through nodes (Figure 4.11d) increased synchronously with dZ decrease (Figure 4.6, Figure 4.9a); it was followed by a decrease in the flow in respect to baseline seen during dZ increase (Figure 4.11d). Thus, less current passed through the nodal membrane during an impedance increase when compared to the resting state.

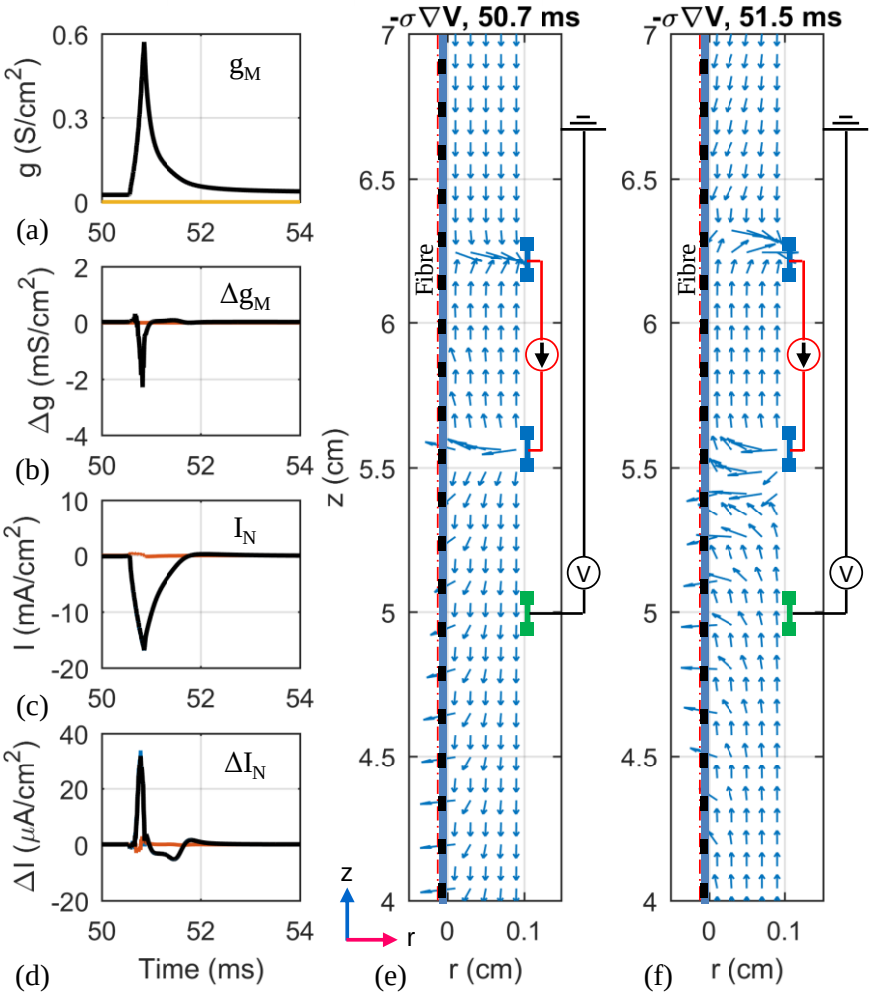

Figure 4.11 Membrane conductances, flow of the ionic currents and distribution of the externally applied current in the simulations performed with the developed myelinated fibre model.
(a) Conductance of the fibre during an AP when DC was applied. Nodal values are depicted by the blue line, internodal (MYSA + STIN) – by red, myelin – by yellow and total values – by black thick lines;
(b) Change in conductance induced by the applied DC, $\Delta g_M = g_{DC}-g_0$; colour legend is the same as in (a);
(c) Membrane current flow at the node measured at DC. Blue line denotes the sum of ionic currents, red line – capacitive current, black line – total current;
(d) Change in membrane current flow induced by the applied DC through the node, $\Delta I_N = I_{DC}-I_0$; colour legend is the same as in (c);
(e) Distribution of the current flow ($\mathbf{j} = -\sigma\nabla V$) at the time when the negative component of dZ was maximal (50.7 ms, Figure 4.6a, Figure 4.9a). Arrows designate the direction of the flux at each point of the extracellular volume (Figure 4.1). The gradient current field is normalized;
(f) Distribution of the current flow ($\mathbf{j} = -\sigma\nabla V$) at the time when the positive component of dZ is maximal (51.5 ms, Figure 4.6a, Figure 4.9a).

The gradient field of the current constructed at the time when the dZ decrease and increase reached maximum (50.7 and 51.5 ms from the start of simulation, as seen in

Figure 4.9a) showed that the direction of the current flow at the position where recording electrode was located (5 cm), was different during the dZ decrease and during its increase (Figure 4.11e, f). Voltage measured by the recording electrode (with respect to ground) was modulated by the impedance only providing the current was constant ($V=Z/I$, eq. (3.1)–(3.2)); however, the current redistributed in the external space during different phases of AP propagation (Figure 4.11e, f) thus affecting the dZ.

Table 4.5

MAIN MYELINATED MODEL SIMULATION RESULTS

Signal processing	Carrier frequency	Optimal bandwidth	dZ* decrease (mean ± s.d.)	dZ* increase (mean ± s.d.)
In- / anti-phase subtraction	DC	-	-0.45±0.04%	0.06±0.04%
	4 kHz	500 Hz	$-(0.7\pm0.3)\cdot10^{-2}$%	-
	6 kHz	4.5 kHz	$-(9.6\pm1.5)\cdot10^{-2}$%	$(4.2\pm1.5)\cdot10^{-2}$%
	8 kHz	7.5 kHz	$-(11.4\pm0.9)\cdot10^{-2}$%	$(4.5\pm0.9)\cdot10^{-2}$%
	10 kHz	8.1 kHz	$-(8.0\pm0.9)\cdot10^{-2}$%	$(1.8\pm0.9)\cdot10^{-2}$%
	12 kHz	9 kHz	$-(6.3\pm0.4)\cdot10^{-2}$%	$(1.3\pm0.4)\cdot10^{-2}$%
	15 kHz	10.6 kHz	$-(5.4\pm0.6)\cdot10^{-2}$%	$(1.3\pm0.6)\cdot10^{-2}$%
No subtraction ("single shot")	DC	-	-	-
	4 kHz	-	-	-
	6 kHz	0.9 kHz	$-(1.9\pm0.9)\cdot10^{-2}$%	-
	8 kHz	1.1 kHz	$-(1.9\pm0.4)\cdot10^{-2}$%	-
	10 kHz	2.1 kHz	$-(3.1\pm0.6)\cdot10^{-2}$%	$(0.8\pm0.6)\cdot10^{-2}$%
	12 kHz	3.9 kHz	$-(4.4\pm0.6)\cdot10^{-2}$%	$(1.4\pm0.6)\cdot10^{-2}$%
	15 kHz	1.8 kHz	$-(2.3\pm0.4)\cdot10^{-2}$%	$(0.6\pm0.4)\cdot10^{-2}$%

*Only dZ significantly different from zero are shown

The injected EIT current flow through the nodes (Figure 4.11d) matched estimates from the gradient field (Figure 4.11e, f): the direction of current flow changed at the area where the recording electrode was located (green on Figure 4.11e and f) and it was accompanied by a decrease in the current flow through this area. Thus, the positive dZ was not a natural increase in membrane impedance but was observed due to redistribution of the applied current flow resulting from the membrane activity.

4.3.3 Comparison with experimental data

The negative dZs simulated using high-frequency AC currents were in a good agreement with data recorded from the sciatic nerve of the rat (Figure 4.9b, c) (Aristovich *et al.*, 2018). In that work, dZ SNR was studied at 6, 8, 10, 11 and 15 kHz; also, the phase of the applied AC current was randomized, so it could be compared to the case when in phase and anti-phase recordings were subtracted (Figure 4.9a). The maximum SNR = 8 was found to be at 6 kHz, it decreased to 2.2 at 8 kHz, but increased again to 4 at 10 kHz, 7.1 at 11 kHz and 5.4 at 15 kHz. Taking into consideration the root-mean-square experimental noise which was constant at 6, 11 and 15 kHz (0.5±0.01 μV) and at 8 and 10 kHz (2.5±0.1 μV) (Aristovich *et al.*, 2018), it is seen that the pure signal was the largest at 10 kHz. In spite of general agreement, the differences between the experimental and simulated results can be explained by: 1) the whole nerve was used instead of a single fibre which changes the compound AP latency due to dispersion in nerve and 2) in the experimental results, a bandwidth of 3 kHz was used for all frequencies, which this current study has revealed is not the optimal parameter setting to use (Figure 4.8). Additionally, positive changes have not been recorded experimentally in myelinated nerves likely because of their small magnitudes which makes it difficult to obtain adequate SNR due to the noise and dispersion absent in single-fibre simulations (Schulte-Mattler *et al.*, 2001; Aristovich *et al.*, 2018).

A number of studies of dZ measurements in unmyelinated nerves of the crab exist, testing dZ at DC (Holder, 1992; Boone, 1995; Gilad *et al.*, 2009) and at up to 1025 Hz AC (Oh *et al.*, 2011; Aristovich *et al.*, 2015) which are supported by the simulations in unmyelinated fibres (Chapter 3). In those experimental studies, the impedance changes were the largest at DC and decreased with AC frequency, which partly agrees with the simulations (Figure 4.9) – while the dZ was the largest at DC, it was impossible to measure it at AC frequencies lower than 4 kHz because of the high characteristic frequency of the AP of the modelled myelinated fibre (Figure 4.7). The dZ did not decrease with frequency from 4 to 15 kHz as the optimal bandwidths for

each frequency were used instead of constant bandwidth utilized in all the studies listed above.

The distances between electrodes have been experimentally studied in unmyelinated nerves only; they agree with the simulated results for the distance between injecting electrodes (Δx_I) (Boone, 1995; Gilad *et al.*, 2009; Oh *et al.*, 2011) but differ from the ones for the distance between recording and injecting electrodes (Δx_R) (Holder, 1992; Gilad *et al.*, 2009) (Figure 4.10). The dZ dependence on the size and locations of the electrodes obtained in the study presented in this chapter is in a full agreement with the ones simulated with the C fibre model described in Chapter 3 (Figure 3.9).

The threshold electrotonus of the developed model (Figure 4.4) closely corresponds to the one obtained in the caudal nerve of the rat (Yang *et al.*, 2000) as well as the recent validated models of myelinated fibres (McIntyre *et al.*, 2002; Howells *et al.*, 2012).

4.4 Discussion

4.4.1 Summary of results

1) The developed one-dimensional FEM model of a myelinated fibre was validated against an experimentally validated space-clamped model (Howells *et al.*, 2012) and agreed with experimental data on AP shape at the node and internode as well as on propagation velocity and threshold electrotonus (Boyd & Kalu, 1979; Waxman, 1980; Harper & Lawson, 1985; Yang *et al.*, 2000; Castelfranco & Hartline, 2016).

2) The simulated dZ did not depend on the amplitude of the applied current below 12.6 μA at all frequencies.

3) The dZ simulated with the developed bi-directionally coupled FEM model were maximal at DC and were different for the two implemented cases of signal

processing, with and without subtraction (Figure 4.2). In both cases, dZ could not be simulated at frequencies lower than 4 kHz due to the high characteristic frequency of the AP and dZ (Figure 4.7). When subtraction of in- and antiphase signals was performed, optimal bandwidths for obtaining the largest dZ were increasing with frequency from 500 Hz at 4 kHz AC to 10.6 kHz at 15 kHz AC (Figure 4.8); magnitudes of dZ decrease reached maximum value equalling -0.11% at 8 kHz (Figure 4.9b). In case when the signal was band-pass filtered without preliminary subtraction, the optimal bandwidth increased from 0.9 to 3.9 kHz at 6 to 12 kHz AC and decreased to 1.8 kHz at 15 kHz AC (Figure 4.8); the maximum dZ decrease was -0.04% at 12 kHz in this case (Figure 4.9b). Small dZ increases resembling the same behaviour with frequency were also recorded (Figure 4.9). These simulations partly agreed with recent experimental results (Holder, 1992; Boone, 1995; Gilad *et al.*, 2009; Oh *et al.*, 2011; Aristovich *et al.*, 2018) as well as with the results obtained for unmyelinated C fibre in Chapter 3.

4) The simulated dZ decreased with the distance between the injecting electrodes ($\Delta x_{I,}$) and between recording and injecting electrodes (Δx_R) (Figure 4.10a, b). For $\Delta x_{I,}$, it was in accordance with experiments carried out on unmyelinated fibres (Boone, 1995; Gilad *et al.*, 2009; Oh *et al.*, 2011), but the dependence was different for Δx_R. The dZ decreased significantly with diameters of the used electrodes and stayed constant with their widths (Figure 4.10c). These results agreed with the unmyelinated fibres model (Chapter 3).

5) The origin of the negative dZ recorded during neural activity was the significant increase in the membrane conductance associated with this activity (Figure 4.11a). The impedance increase following the decrease at all frequencies (Figure 4.6, Figure 4.9a) appeared due to redistribution of the injected current at the area of recording (Figure 4.11e, f). In this case, the recorded voltage reflected not only the change in impedance but also a change in the direction of the current flow induced by the membrane activity.

4.4.2 Answers to the stated questions

1. How does the impedance change depend on the experimental parameters?

a) Amplitude and frequency of the injected current;

The maximum current at which dZ was linear with it was 12.6 μA when DC was applied; the limit significantly increased at AC equalling approximately 125 μA at 6 kHz (Figure 4.6). The linearity of the dZ with the injected current is important for the measured voltage to signify impedance change and not depend on the current itself. As a result, 12.6 μA was chosen as a safe current which did not affect neuronal excitability and was used in all simulations at all frequencies.

The largest dZ was simulated at DC; at AC, the optimal frequency providing the largest dZ depended on the way of signal processing (Figure 4.9). In the case when subtraction of in-phase and anti-phase signal was performed (Figure 4.2), the largest dZ was observed at 8 kHz, in the other case, the optimal frequency was 12 kHz but the dZ was ~3 times smaller. These values were obtained using the optimal bandwidths for each frequency (Figure 4.8).

b) Signal processing specifications

Two signal processing scenarios was studied: 1) when two signals with the current in-phase and in antiphase were recorded and then subtracted before band-pass filtering and demodulation; 2) "single-shot" measurement, when the raw recorded signal was band-pass filtered around the carrier frequency and demodulated (Figure 4.2). The first scenario resulted in higher dZ because the AP was subtracted and therefore the artefacts associated with it were minimized (Figure 4.9). For this case, the optimal parameters were 8 kHz AC with 7.5 kHz bandwidth (Figure 4.8, Figure 4.9): there was minimal AP artefact and the large bandwidth allowed to extract full frequency band of the dZ (Figure 4.7). The second case when subtraction was not performed was studied because it could provide the means for real-time imaging as there was no need to record twice, in phase and in antiphase, to obtain a dZ. In this case, the possible bandwidth was limited because the AP was present (Figure 4.7) causing artefacts in the

measurements. Thus, the optimal parameters were to use 3.9 kHz bandwidth at 12 kHz AC (Figure 4.8, Figure 4.9).

The reason for the increase in the optimal bandwidth with the measuring AC frequency is that the dZ has significant frequency components at up to ~8 kHz that are resolved with higher temporal resolution and therefore, bandwidth. In the case when there was no subtraction, the optimal bandwidth at 15 kHz AC was smaller than the one at 12 kHz AC (Figure 4.8) because the natural dZ of the fibre decreased with frequency (since the membrane is a parallel resistance and capacitance) while standard deviation increased with it. This increase was due to a small high-frequency noise (~19 kHz) brought by modelling errors; this noise was the same in different simulations and was eliminated during phase-antiphase subtraction. Although this noise is absent in experiments, the "single shot" model case could provide a general trend showing an increase in the optimal bandwidths' values with the carrier frequency up to 12 kHz (Figure 4.8), which is important for optimizing signal processing for fast neural EIT.

c) Size and position of the electrodes

With increasing distance between the electrodes, the decrease in dZs was observed (Figure 4.10a, b); dZ decreased significantly with increasing electrodes diameter and was not affected by their widths (Figure 4.10c). These results were in agreement with the ones for unmyelinated fibres presented in Chapter 3.

2. Does this agree with the previous studies?

a) Does the model validate recent experimental recordings?

The modelled frequency dependence of the dZ decrease is in general agreement with the experimental data on the sciatic nerve of the rat (Aristovich *et al.*, 2018). Although the model was developed for a single fibre, the results were comparable as dZs were shown to have a close-to-linear behaviour with the increasing number of fibres (Chapter 3).

Also, as real nerves consist of thousands of fibres, there is an effect of temporal dispersion (Schulte-Mattler *et al.*, 2001) – increase in the latency of the compound AP which occurs due to variability of fibres' conduction velocities. This affects the dZ

latency in the same way, so theoretically AC frequencies lower than 4 kHz may be used for dZ recordings. However, dispersion in myelinated fibres is weak (~30% reduction over a meter nerve) (Olney *et al.*, 1987); therefore this effect is not expected to strongly influence the results obtained in simulations.

Impedance changes obtained in the experimental studies on unmyelinated nerves (Holder, 1992; Boone, 1995; Gilad *et al.*, 2009; Oh *et al.*, 2011; Aristovich *et al.*, 2015) were different from the simulations: significantly lower AC frequencies were needed to record reliable dZ whose amplitudes monotonically decreased with frequency. This is partly because the characteristic frequency of AP in unmyelinated fibres is significantly smaller than in the myelinated ones allowing it to be processed using slower carriers. Also, constant bandwidths were used in the experiments that also affected the dZ-frequency dependence.

b) Does it offer an explanation on the origin of the dZ?

By analysing the flow of the external injected current as well as the membrane currents and conductances during negative and positive phases of the dZs (observed at 50.7 ms and 51.5 ms, Figure 4.6a, Figure 4.9a), the model provided insight on their biophysical origin (Figure 4.11). In line with expectations, the dZ decrease was due to the opening of ion channels and the significant increase in conductance (Figure 4.11a). Conversely, an increase in the dZ was shown to be associated with the change in the flow of the injected current around the recording electrode. This change was due to dynamics of ion channels' opening along the fibre during different phases of AP inducing the current in the external space near the recording electrode to change the direction according to the path of least resistance (Figure 4.11e, f). Therefore, the dZ obtained by demodulation of the recorded voltage was inaccurate as it started to depend on the changed current. This conclusion was also supported by measuring the change in the injected current flow through the nodes: it increased during the negative dZ phase but decreased during the positive dZ phase (Figure 4.11d).

Thus, the recorded apparent dZ increase did not reflect a real increase in impedance as it was contaminated by the change in the current. However, this apparent increase was reproducible and so may be used in EIT imaging.

c) Does it provide results different from the model of unmyelinated fibres presented in Chapter 3 and the passive model (Liston et al., 2012)?

The dZ in the model of unmyelinated fibres (Chapter 3) differed from the ones simulated in the current study in two ways. First, the current model showed that dZ could not be measured in a myelinated fibre using any AC frequency. As the dZ frequency band of a modelled myelinated fibre covered a 1–8 kHz range (Figure 4.7), high AC measuring frequencies of >4 kHz were necessary for dZ extraction via demodulation (Section 4.2.3). Second, apart from being the largest at DC, the simulated dZ did not monotonically decrease with frequency. This was because the optimal bandwidths used during band-pass filtering of the recorded signal were determined at each carrier frequency (Figure 4.2, Figure 4.8) that allowed finding the optimal frequency at which the largest possible dZ could be extracted. On the other hand, these models agreed on the dZ dependence on the sizes and locations of the used electrodes as well as on the presence of the apparent positive dZ changes.

The findings simulated with the passive model (Liston *et al.*, 2012) did also not match the current one: it included different dependence of the dZ on frequency as well as inability of this model to predict finer properties such as the dZ increase.

3. What recommendations can be given for optimization of imaging myelinated fibres using fast neural EIT?

The main recommendation is to use higher bandwidths for higher carrier frequencies, which have not been previously utilised experimentally. However, since the natural dZ signal decreases with frequency, an optimal combination of AC frequency and bandwidth must be found for each particular nerve. In this study, it was 8 kHz AC with 7.5 kHz bandwidth when subtraction of in- and antiphase signals was performed (Table 4.5, Figure 4.8) and this was in agreement with the existing experimental data (Aristovich *et al.*, 2018). Also, the same as for the unmyelinated model discussed in Chapter 3, the smallest possible electrodes should be used and the distance between them should be minimized.

4.4.3 Technical issues

The main technical problem, as in the case of the unmyelinated fibre model (Chapter 3), was high computational requirements and therefore long simulation times. Even the use of 2D axisymmetric simplification could not significantly improve the computing speed, which was around 1-2 hours for a single simulation; more than a hundred of those were necessary to test the model with different parameters and obtain necessary statistics. The reason for such low-speed simulations was that the spatial structure of the fibre was strongly heterogenous while the FEM approach operates with continuous solution approximation along its length. This results in poor convergence at the boundary points connecting nodes with internodes due to sharp transition in potentials in those points (Figure 4.3e). To address this issue, the non-uniform mesh was created, where element size decreased towards the boundary (Table 4.1, Figure 4.1). Such a mesh included very small elements in the nodal and adjacent regions and was repeated in the external domain for coupling (Figure 4.1b) which also significantly increased the time of computation.

Acceleration of the simulations is thus critical. It may, for example, be reached by exclusion of active ion channels at the internodes as in MRG model (McIntyre *et al.*, 2002), or by switching back from FEM to compartmental model that, however, may degrade the accuracy of simulations coupled with the external space (*Section 4.2.1*).

Due to non-perfect convergence discussed above, the solution of the developed model was contaminated with a small ~19 kHz noise which introduced errors in high-frequency "single-shot" simulations. However, this noise was the same at different phases of the injected current and so clearly eliminated in phase-antiphase subtraction case.

4.5 Conclusion

An accurate FEM model of a myelinated fibre bi-directionally coupled with external space was developed using the experimentally validated space-clamped

model of a human sensory fibre. The created model allowed simulation of dZ during an AP propagation and this facilitated determination of the optimal parameters for imaging myelinated fibres with EIT.

The dZ decrease simulated with the model was in agreement with experimental data. The model also predicted a small apparent dZ increase and was able to provide an explanation to its biophysical origin. The performed simulations allowed finding the optimal bandwidths at each AC frequency for enhancing the efficiency of dZ measurements. Also, optimal currents, as well as sizes and locations of the used electrodes, were determined.

Chapter 5
Effect of dispersion in nerve on impedance change

5.1 Introduction

5.1.1 Overview

One of the main objectives of fast neural EIT is to image physiological spontaneous activity in autonomic nerves. This can be valuable for a new area of bioelectronic medicine aimed at neuromodulation of internal organs supplied by these nerves.

The previous two chapters investigated the optimal EIT parameters for a single or a small number of simultaneously firing unmyelinated and myelinated fibres. However, main autonomic nerves such as the cervical vagus nerve comprise thousands of small fibres. More than two-thirds of those are unmyelinated in mammals (De Neef *et al.*, 1982; Asala & Bower, 1986; Prechtl & Powley, 1987; Soltanpour & Santer, 1996) and humans (Shimizu *et al.*, 2011; Verlinden *et al.*, 2016) and have slow conduction velocities (CV) of about ~0.5-2 *m/s* (Coleridge & Coleridge, 1984). As the fibres are not identical, their CV also differ that causes dispersion of APs along the nerve during propagation (Chapter 2.2.5). Consequently, it is challenging to record a signal of sufficient amplitude when moving away from a point of stimulation, and this effect is proportionately greater for unmyelinated fibres than faster conducting fibres. For example, in rat sciatic nerve, significant dZ could only be recorded in fast fibres with low dispersion more than 5 cm from the onset site (Aristovich *et al.*, 2018). Impedance measurements in the walking leg nerve of the crab which are unmyelinated

(Boone, 1995) also demonstrated high dispersion with the possibility of CAP recording only up to 1.6 cm from the stimulus. In addition, only fast fibres were possible to be imaged with fast neural EIT in the rat sciatic nerve experiment (Aristovich *et al.*, 2018) while the activity of C fibres was not visible.

In spite of this issue, there is potential for EIT to image unmyelinated fibres at greater distances than the CAP. The reason is that extracellular action potentials (EAPs) of individual fibres may be expected to disperse sooner than the related impedance changes because they are usually biphasic or triphasic (Harper & Lawson, 1985; Gold *et al.*, 2006; Agudelo-Toro & Neef, 2013; Ghitani *et al.*, 2017) (Figure 2.10) and so cancel when separated by dispersion. This effect may be expected to be much less for dZ which are mainly monophasic (Faulkner *et al.*, 2018*b*; Aristovich *et al.*, 2018); in principle, therefore, dZ should decrease slower than CAP.

In this chapter, we have explored the possibility of recording dZ further than CAP by developing 3D FEM computational models comprising 50 fibres with HH (Hodgkin & Huxley, 1952) or C nociceptor (Tigerholm *et al.*, 2014) ion channels with normally distributed sizes and propagation velocities. These models were bi-directionally coupled with the external space that allowed injection of electric current via external electrodes and simultaneous external recording at various distances down the nerve. Simplified statistical models matching the accurate ones were developed to accelerate computations and allow dZ simulations of complex nerves with > 10k axons.

5.1.2 Purpose

The purpose of the study presented in this chapter was to investigate the dZ behaviour in complex compound nerves relative to CAP. A specific interest was to test the hypothesis that impedance changes can be recorded further down the nerve from the site of its stimulation than the CAP.

Specific questions addressed were:

1. Is it possible to record dZ further than CAP?
2. Are there differences between models in the effect of dispersion on dZ?

3. What is the largest distance from the site of stimulation at which dZ can be recorded ?
    a. for nerves consisting of Aα, Aβ, Aδ and C fibres;
    b. for realistic nerves such as the right vagus and sciatic nerves of the rat.

5.1.3 Experimental design

The study was accomplished by development of 3D fully coupled models of nerve comprising 50 active fibres with normally distributed CVs: giant axons of the squid (Hodgkin & Huxley, 1952) or mammalian C nociceptors (Tigerholm *et al.*, 2014). These models were based on previously developed accurate active models of single fibres coupled with external space (Chapter 3). They utilized the finite element method (FEM) approach and were built in COMSOL Multiphysics software (COMSOL Inc, USA) in conjunction with MATLAB using LiveLink for MATLAB interface. Due to the different size of the axons involved, diameters of the nerve models and circumferential electrode rings were 2.4 and 0.01 cm for the HH and C fibre models, respectively. The width of the electrode rings was adjusted accordingly to 100 and 5μm (Table 5.1). Although a diameter of 2.4 cm HH nerve exceeds the human or mammalian anatomical range, it is computationally efficient and is a useful basis to answer the questions about dispersion stated above.

Realistic EIT experimental conditions were simulated in which a linear electrode array was used for dZ measurements (Oh *et al.*, 2011; Aristovich *et al.*, 2015). This enabled calculation of APs and dZs by external electrodes along the nerve in order to explore if the initial hypothesis was supported. The detailed models were complemented with simplified statistical models which allowed dZ of much larger nerves with >10k axons to be simulated without extensive computation; these were still in good agreement with the 3D FEM models. Statistical models were based on the histological studies which provided morphological properties of fibres and their CVs. Measurements with FEM models were accomplished using direct current; alternating current was added in the statistical models. The reason was that simulations at DC demanded significantly smaller time to compute: 8 hours per single simulation

vs 20 hours for the 225 Hz AC case; this time increased with increasing frequency because of the appearance of transient effects and their interaction with the active membrane. Also, modelling of unmyelinated fibres performed in Chapter 3 showed that the dZ reached maximum at DC and no differences in biophysical origin of dZ recorded using AC or DC were observed.

5.2 Methods

5.2.1 Accurate FEM models

1. Model setup

The developed models included 50 one-dimensional active nerve fibres and a 3D extracellular space bi-directionally coupled together. The coupling feedback system allowed simultaneous recording of intracellular action potentials and extracellular field created by the membrane currents and the injected current (Figure 3.3 in Chapter 3). The fibres were simulated as cables with active voltage-dependent experimentally validated ion channels using either Hodgkin-Huxley model of the giant axon of the squid or mammalian C fibre with 10 active ion channels and voltage-dependent ions' concentrations (Tigerholm *et al.*, 2014).

The interaction between fibres was omitted as it was shown to not significantly affect the measurements (Chapter 3). The external space was represented as a cylinder with a uniform electrical conductivity equalling 10 *mS/cm* (Elia & Lamberti, 2013). EIT current was injected and the resultant voltage was recorded by means of external electrodes (Table 5.1). The mesh of HH and C fibre models comprised 1.6M and 530k tetrahedral elements, respectively.

The main equations and electrical parameters of the models were the same as for the single fibre and can be found in Chapter 2 and Chapter 3. In short, the external field was simulated with volume conduction Laplace's equation (2.22); the current was injected as a constant flux through the ring electrodes (3.3). Stimulation of the fibres was implemented via the inclusion of an activating function into the main equations of

the nerve fibres – the HH model (3.11) and the C fibre model (3.12). Membrane currents flowing out of the fibres to the external space were represented as a normal flux through the boundaries of the modelled axons (2.23).

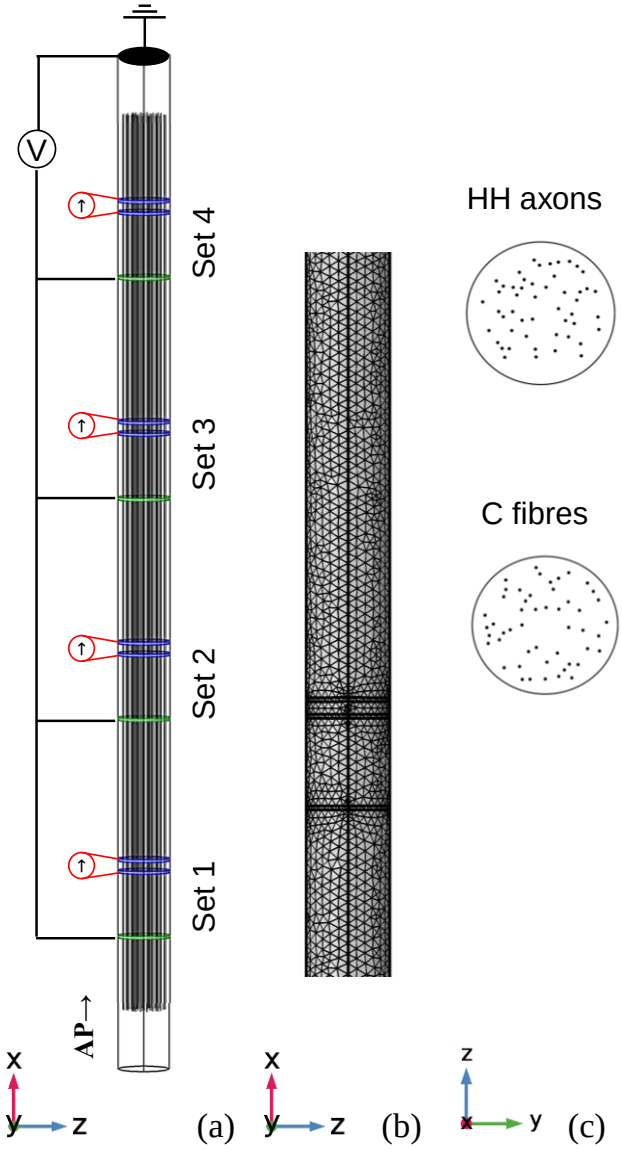

Figure 5.1 Geometrical structure and FEM mesh of the developed 50-fibre FEM models.
(a) 3D geometry of the 50-fibre models with normally distributed CVs (Table 5.2). The AP was induced at the end simultaneously for all the fibres; the current was injected via two external electrodes (blue) and the electric field was recorded by an external electrode (green) located before the injecting ones with respect to ground. Four sets of electrodes were used to record dZ accompanying AP propagation (Table 5.1).
(b) Example of tetrahedral FEM mesh used in the models;
(c) Cross-section view of the uniform distribution of the fibres used in the models.

Table 5.1
MAIN PARAMETERS OF THE FEM MODELS WITH 50 FIBRES

Parameter	HH model	C fibre
Fibre diameters	1 mm	1 µm
Diameter of the electrodes / surrounding volume, D_{el}	2.4 cm	0.01 cm
Width of the electrodes, H_{el}	0.1 cm	5 µm
Length of the nerve	60 cm	2 cm
Number of electrodes sets	4	4
Distances of electrodes sets from stimulation point	10, 19, 25, 35 cm	0.4, 0.8, 1, 1.4 cm
Injected EIT current	30 µA	6.3 nA
Distance between recording and injecting electrodes in each set, Δx_R	0.2 cm	0.01 cm
Distance between injecting electrodes in each set, Δx_I	0.5 cm	0.002 cm
Intracellular resistivity	0.05±0.02 kΩ·cm	0.0354±0.01 kΩ·cm
Conduction velocity (5.1)	15±2.8 m/s	0.6±0.07 m/s
Scaling coefficients of single fibre signals for simplified models	16	100

Fibres were uniformly distributed inside the insulated cylinder with the diameter depending on the type of fibres (Table 5.1). The size of the cylinder defined the diameters of the electrodes as well as the amount of the external space (Figure 5.1). Impedance of the electrodes did not affect the measured dZ because a 4-electrode measurement paradigm (Schwan & Ferris, 1968) was used for time-difference single impedance measurements (Holder, 2004*a*).

Dispersion was implemented by normally distributing CV of the fibres by randomizing their intracellular resistivities. Their mean values were taken from the developed validated models: 0.05 kΩ·cm for the model with HH axons, and 0.0354 for the one with C fibres (Table 5.1) (Hodgkin & Huxley, 1952; Tigerholm *et al.*, 2014). Standard deviations (0.02 kΩ·cm for the HH axons and 0.01 kΩ·cm for C fibres) were chosen to have a significant visible dispersion along the modelled lengths of the nerves (60 cm for HH and 2 cm for C fibre, Table 5.1) and so that it is similar to experimental recordings (Gasser, 1950; Boyd & Kalu, 1979) (Table 5.2).

For each model, four sets of electrodes were placed along the nerve; each set consisted of two injecting ones through which the constant small direct current not

affecting the membrane was applied: 30 µA (40 µA/cm^2) for HH and 6.3 nA (4 mA/cm^2) for C-fibre nerves; the recording electrode was used for measuring the resultant external voltage in respect to ground (Figure 5.1). Impedance changes recorded at DC have been shown to have the largest values and the same physiological nature as the AC ones (Chapter 3), so they provided a good starting point for simulations. Electrodes had diameters of 2.4 cm and 0.01 cm and widths of 0.1 cm and 5 µm for models with HH and C fibres respectively (Table 5.1). This large electrode diameter for the HH axons was chosen to accommodate all giant squid axons (d = 1 mm) inside it and so that the packing density would be similar to the nerve with C fibres (Figure 5.1).

The location of the recording electrode in each set was at 10, 19, 25, 35 cm from the activation point for the HH nerve and 0.4, 0.8, 1, 1.4 cm for C fibre nerve; distances between recording and injecting electrodes (Δx_R) for HH and C fibre cases were 0.2 and 0.01 cm; distances between injecting electrodes (Δx_R) were 0.002 and 0.5 cm respectively (Table 5.1). The action potentials were initiated simultaneously at the end of the nerve.

The COMSOL model files saved in Matlab format are provided in the EIT-lab GitHub repository at https://github.com/EIT-team/Dispersion-modelling.

2. Signal processing

Two simulations with and without current injection were done for each location of the electrode sets. Each simulation lasted 40 *ms* for HH and 30 *ms* for C fibre models. Overall, 4 electrodes locations · 2 states = 8 simulations were done for each type of the nerve. The process of dZ extraction repeated the one utilized in the single fibre models described in Chapter 3 (Figure 3.4a). In case of DC injection which was performed in the current study, it included a) subtraction of the signals with and without the injected current to eliminate action potentials but preserve impedance change and b) subtraction of the mean baseline voltage in order to express the impedance change in terms of absolute voltage change in µV. If percentage values were needed, normalization of the obtained absolute dZ was done.

dZ were expressed in μV because the constant current was applied and the phase shift between the current and the measured voltage is close to zero (Cole & Curtis, 1939), as seen in the equation (3.1). Thus, changes in voltage traces in Figure 3.4a, Figure 5.4 and Figure 5.5 are referred to as dZ as they signify impedance changes and can be directly compared with dZ expressed in percent (3.2).

The negative integral areas under the CAPs and dZ curves recorded by each electrode set were calculated to compare the effect of their cancellation due to dispersion. Because the absolute values of these areas had different orders of magnitude and in order to compare their behaviour, they were normalized in respect to the ones at the shortest computed distances (Table 5.1): 10 cm for HH and 0.4 cm for C fibre models.

5.2.2 Simplified statistical models of 50-fibre nerves

Since 50-fibre fully coupled FEM models were very computationally intensive, a simplification was developed in order to obtain necessary statistics for calculation of the desired area under the CAP and dZ curves. CAP and dZ signals were obtained at the same distances from stimulation point as in the developed FEM model (Table 5.1) by summarizing 50 units of AP and dZ signals simulated on a single fibre in Chapter 3 (Figure 5.4) with each fibre possessing a constant normally distributed CV (Figure 5.2). Single fibre dZ signals measured at DC and at AC currents (1 kHz for HH and 2 kHz for C fibre) were used for simulations. To increase the absolute magnitude of impedance changes measured at AC, the EIT current used for obtaining them was 10 times larger than at DC, due to the increase in safe range values (Chapter 3). Because dZ is linear with respect to the amplitude of the injected EIT current (Holder, 2004*a*; Gilad *et al.*, 2009), the absolute μV amplitudes of the single fibre signals were linearly corrected to the same current level as in the FEM model. Before summation, these signals were scaled in amplitude due to the difference in electrode diameters used for single fibre and 50-fibre simulations and therefore different distances from the electrode to the fibre. The recorded amplitude reduction due to the increase in distance to the fibre was proportional to $1/r^2$, according to Coulomb's law, therefore the used

single fibre signals were decreased $(d_{50}/d_1)^2$ times where d_{50} is the diameter of the electrodes used in 50-fibre models (2.4 and 0.01 cm, Table 5.1) and d_1 are the diameters used for single fibre models which equalled 0.6 cm and 10 μm for HH and C fibre model respectively (Chapter 3). Thus, the single fibre signals inserted into the developed simplified 50-fibre model were decreased 100 times in the case of C fibres and 16 times for HH axons (Table 5.1).

Parameters of the distribution of velocities were chosen so that they correspond to the distribution of axoplasm resistivities in the FEM model (Table 5.1). Based on the cable structure of nerve fibre, the CV can be expressed as the ratio of the length constant of the fibre to its time constant (Johnston & Wu, 1995):

$$v = \frac{\lambda}{\tau} = \frac{\sqrt{r_m/r_i}}{r_m C_m} = \frac{\sqrt{0.25 \cdot d_{ax} \cdot \rho_m/\rho_i}}{\rho_m c_m} \sim \frac{1}{\sqrt{\rho_i}} \quad (5.1)$$

where λ [m] and τ [s] are length and time constants of the nerve, r_m [Ω·cm] and r_i [Ω/cm] – membrane and axial resistances; C_m [F/cm] – membrane capacitance; ρ_m [Ω·cm^2], ρ_i [Ω·cm] and c_m [F/cm^2] are a membrane and intracellular resistivities and specific membrane capacitance; d_{ax} [cm] is the diameter of the axon.

Thus, CV is inversely proportional to the square root of intracellular resistivity. Given that mean values are 15 m/s for HH model and ~0.6 m/s for C fibre model, S.D. obtained from (5.1) were 2.8 and 0.07 m/s for these fibre types respectively (Table 5.1).

Source code for 50-fibre statistical models is available at https://github.com/EIT-team/Dispersion-modelling.

5.2.3 Statistical modelling of dZ in complex nerves

As it was impossible to implement computationally-heavy accurate 3D FEM models for realistic nerves containing thousands of fibres, simplified statistical models containing up to 100k different fibre types were developed. The implemented approach was based on the inverse proportionality of the recorded impedance changes to the

cross-sectional area of the measured nerves. This is because the intracellular resistivity of fibres is lower than the external one, therefore, when ion channels open, the injected current flows to the area with lower resistivity and a small decrease in the dZ of the system "nerve + external space" is observed. Approximating the nerve fibre as a cylinder with a constant diameter, its resistance can be written as:

$$R_{in} = \frac{\rho_{in} \cdot L_n}{S_n} \sim \frac{1}{d^2} \tag{5.2}$$

where ρ is the axoplasm resistivity [$\Omega \cdot cm$], L_n [cm], S_n [cm^2] and d [cm] are length, cross-sectional area and diameter of the nerve. So, the resistance of the nerve is inversely proportional to cross-sectional area meaning that the recorded Z has the same dependence.

Table 5.2
PARAMETERS OF THE STATISTICAL MODELS

Parameter	**Aα**	**Aβ**	**Aδ**	**C**
Velocity	90±8 m/s	65±9 m/s	20±3 m/s	$2d^{0.5}$
Fibre diameter	16.5 μm	12 μm	4 μm	0.8±0.2 μm
Size of the nerve	Area = 0.1 mm^2 Diameter = 357 μm			
Number of fibres	300	500	4800	76000
Area occupied by fibres	60 %			
Single dZ latency	0.5 ms	0.8 ms	1 ms	2 ms
Scaling coefficients	$k_{conn} = 26.1$; $k_{el} = 1270$; $k_{\Sigma} \approx 3.3 \cdot 10^4$			

Simple statistical models were developed to find the maximal distances at which impedance changes may be theoretically measured. This was accomplished for four types of nerves consisting of a single type of fibres: Aα, Aβ, Aδ and C as well as for realistic sciatic and right vagus nerves of the rat (Table 5.2). CAPs were not simulated in these models as the main interest was to study how dZ disperses with the distance from the onset site.

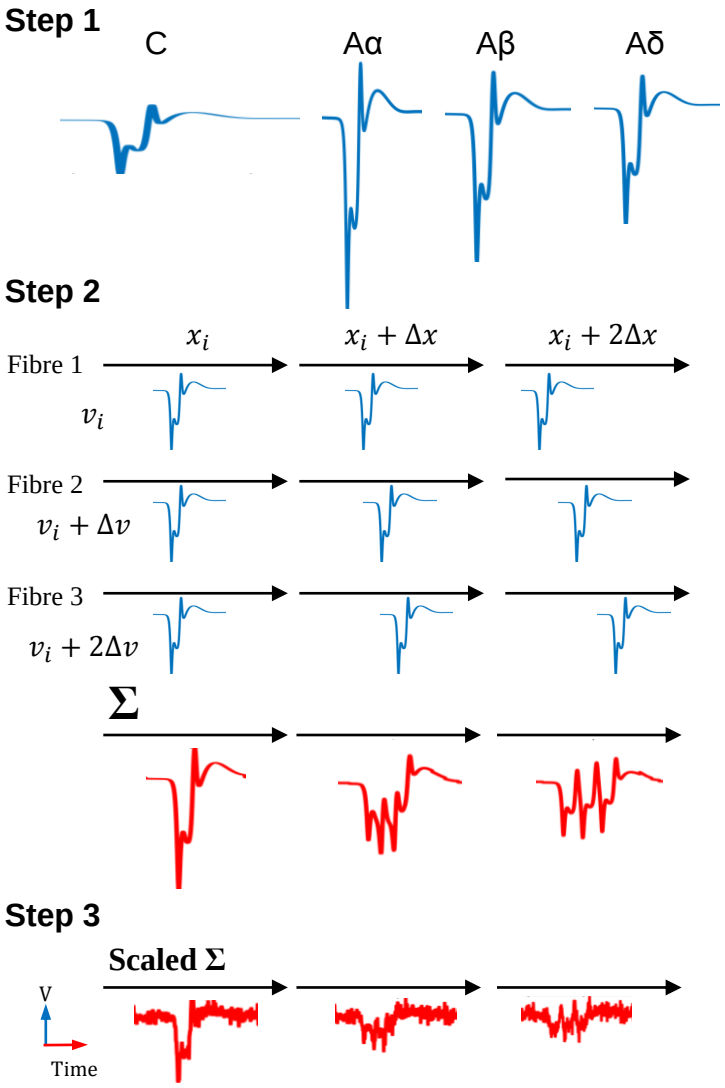

Figure 5.2 Schematic representation of dZ dispersion in the developed model. The same is applicable to APs (Figure 2.12).
The models were implemented in three steps: 1) modification of the dZs of each fibre in accordance with their cross-sectional area (5.2) and AP latencies; 2) summarizing the AP or dZ of single fibres having constant but different normally distributed CVs; 3) scaling of the resultant signals in accordance with the nerve diameter and conductivity of connective tissue (5.5) and adding the experimental noise.
This picture demonstrates on a simple three-fibre example, how the compound dZ (red) is formed from the dZ of single fibres (blue) with slightly different CVs. In each fibre, the AP propagates with constant velocity v_i; the compound dZ is equal to the sum of dZ_i in all single fibres. It is seen that the amplitude of compound dZ decreases with distance. The shape of dZ used this picture was obtained from simulations for realistic single C fibre presented in Chapter 3; it was inserted into the developed statistical multiple-fibre models with velocity distribution taken from the literature (Table 5.2).

These models were implemented in the same way as the simplified 50-fibre models (*Section 5.2.2*). In the models, the compound dZ at DC and at 2 kHz were computed as a sum of modified dZ of all single fibres at different distances from the stimulation

point (Figure 5.2). CVs in each fibre were assumed to be constant and normally distributed; the values for normal distributions were taken from the experimental data found in the literature discussed in the text (Table 5.2, Table 5.3). Modifications of the previously simulated dZ of a single realistic mammalian C fibre depended on the fibre type (Figure 5.2): the dZ latency for fast fibres linearly decreased in accordance to the latency of their APs (Table 5.2); the dZ amplitude increased proportionally to their cross-sectional area (5.2) (Figure 5.2). Conduction velocity (mean and S.D.) and latency data for Aα, Aβ and Aδ fibres was taken from (Boyd & Kalu, 1979) for motor and cutaneous nerves of the cat. Data for C fibres was obtained from diameters distribution (Gasser, 1950) and experimentally found equation (5.3) (Rushton, 1951) presented below:

$$v_{unmyel} = 2 \cdot \sqrt{d_{fibre}} \tag{5.3}$$

where v_{unmyel} $[m/s]$ is the conduction velocity of unmyelinated fibre and d_{fibre} $[\mu m]$ is its diameter.

A number of fibres in each type of nerve was chosen so that they fit into the 0.1 mm^2 rat vagus nerve (Soltanpour & Santer, 1996) given that around 60% of nerve cross-sectional area is occupied by fibres (Birren & Wall, 1956) (Table 5.2). The numbers were (Figure 5.5): 300, 500, 4800 and 78000 fibres for Aα, Aβ, Aδ and C fibres respectively.

All the parameters for realistic nerves (Table 5.3) were based on morphometric data for sciatic (Schmalbruch, 1986) and vagus nerves of the rat (Soltanpour & Santer, 1996) and the experimentally found CV vs diameter dependencies for unmyelinated C fibre (5.3) (Gasser, 1950; Rushton, 1951), as well as myelinated Aβ and small Aδ fibres (5.4) (Boyd & Kalu, 1979):

$$v_{myel} = 4.6 \cdot d_{fibre} \tag{5.4}$$

where v_{myel} $[m/s]$ is the CV of a myelinated fibre and d_{fibre} $[\mu m]$ is its diameter.

Because some of the parameters in the model of a single C fibre (Chapter 3) differed from the realistic nerve model, the dZ taken from it had to be scaled before fitting it into the models with multiple axons. There were two main differences: first, extracellular space in a single fibre model was simulated as a highly conductive saline solution, while in reality it consists of more resistive connective tissue; second, the diameter of the recording electrode was small (10 μm) so that it could fit only one fibre. Thus, the scaling coefficients k_{conn} and k_{el} were introduced to account for these discrepancies; the dZ obtained after summation of all single dZ across all fibres (Figure 5.2) was scaled by dividing it by the product of these coefficients (5.5). The connective tissue was assumed to consist of 3% endoneurium, 3% perineurium and 94% epineurium with resistivities 1.211, 1.211 and 47.8 kΩ·cm respectively (Choi *et al.*, 2001). The weighted average of these values equalling 2.6 kΩ·cm was used which was around k_{conn} = 26 times smaller than 0.1 kΩ·cm previously used for saline (Chapter 3). To account for larger distance from measuring electrode to the fibres, and because the electric field is inversely proportional to the squared distance from the object, the scaling coefficient was chosen to be equal to $k_{el} = (r_1/r_0)^2$ where r_1 and r_0 are new and previous distances to the fibre respectively equalling to electrode radii. In the single fibre model discussed in Chapter 3 electrode diameter was 10 μm; the complex nerves had diameters equalling 357 μm for the right rat vagus nerve and a single fibre type nerves (Table 5.2): the number of fibres in them were chosen to match this diameter. The diameter was 700 μm for rat sciatic nerve (Table 5.3) (Schmalbruch, 1986). Thus, k_{el} was equal ~1270 and 4900 for these nerves respectively.

The resultant scaling coefficient was (Table 5.2, Table 5.3):

$$k_{\Sigma} = k_{conn} \cdot k_{el} = \frac{\rho_{sal}}{\rho_{conn}} \cdot \left(\frac{d_{nerve}}{d_{el,1}}\right)^2 \tag{5.5}$$

where ρ_{sal} and ρ_{conn} [$k\Omega{\cdot}cm$] are resistivities of the saline and connective tissue composed of epineurium, endoneurium and perineurium, $d_{el,1}$ and d_{nerve} [μm] are the diameters of the electrodes in the single fibre simulations and the simulated nerve respectively. For scaling, the final compound dZs found in step 2 of the model (Figure 5.2) were divided by the resultant coefficient k_{Σ} (Table 5.2).

Table 5.3
PARAMETERS OF THE RIGHT VAGUS AND SCIATIC NERVES OF THE RAT

Parameter	Right vagus nerve	Sciatic nerve
Nerve diameter	357 µm	700 µm
Fibre composition	7000 Aδ 40000 C	7800 Aβ 19000 C
Fibre diameters	Aδ: 2.68±1.75 µm C: 0.76±0.28 µm	Aβ: 6±3 µm C: 0.76±0.2 µm
Scaling coefficient, k_Σ	~$3.3\cdot10^4$	~$1.3\cdot10^5$

Each nerve was simulated with a length of up to 50-cm and the duration of each simulation was 50 *ms*. Using the sequence of the steps explained above, dZ for all nerves were obtained at 2, 4, 10, 20 and 50 cm from the stimulation site. Experimentally observed root mean square (RMS) noise of 0.5 µV (Aristovich *et al.*, 2018) was added to the resultant compound dZ as the last step (Figure 5.2). Then, a signal-to-noise ratio was computed as a ratio of the amplitude of a pure compound dZ signal to the standard deviation of the added noise. Ten random models with the parameters specified above were computed for statistics. The maximum distance at which dZ can be theoretically measured and possibly imaged was calculated. The dZ signal was considered measurable if SNR was more than 1 (≥ 0 dB); the dZ was possible to be imaged if SNR ≥ 4 (>= 12 dB) (Gilad & Holder, 2009). All the results were compared with the available experimental data using SNR and maximum distances of signals' detection.

Source code for statistical models of complex nerves is available at https://github.com/EIT-team/Dispersion-modelling.

5.3 Results

5.3.1 Hodgkin-Huxley axons model

The amplitudes of the CAPs simulated with the realistic 3D FEM model (Figure 5.1) decreased with the distance from the AP initiation point (i.p., Figure 5.3): they

were ~ 7 mV at 10 cm, 6 mV at 19 cm, 4.5 mV at 25 cm and 3 mV at 35 cm from the stimulation point. Duration of the negative phase of the compound AP increased from 4 to 5, 6 and 7 ms along the same distances respectively (Figure 5.3a). dZ had the same behaviour. It decreased from -3.5% (-7 μV) at 10 cm, to 2.9% (-5.8 μV) at 19 cm, 2.5% (5 μV) at 25 cm and 1.8% (3.5 μV) at 35 cm from stimulus while duration of its negative phase increased from 9 to 11, 12 and 15 ms at the same distances (Figure 5.3a). The area under the CAP fell to about 62% of the one at 10 cm from the location of nerve stimulation. In contrast, the area under dZ signal curves was close to constant at these distances (Figure 5.3c).

Necessary statistics (standard deviations) in the calculated areas were obtained with the computation of 100 simplified statistical models with 50 fibres and the same CV distributions as in the FEM model. The CAP and dZ at DC in these models were close to the ones obtained with the accurate FEM model (Figure 5.4b, Figure 5.3a); they also allowed computation of dZ dispersion recorded at AC (1 kHz in HH case) current. The areas under the CAP computed with these models were (in respect to the ones at 10 cm, Figure 5.3d): 83.1±2.9% at 19 cm, 75.6±3.8% at 25 cm and 67.9±4.3% at 35 cm. dZ measured at AC at the same distances were also decreasing with distance: 84.4±2.7%, 77.5±3.3% and 71.5±3.3% with respect to the dZ at 10 cm from the stimulus. The area under the dZ curves measured at DC was constant and independent on the distance from AP initiation point (i.p.) (red line in Figure 5.3d, left). These values are in close agreement with the results obtained using the accurate FEM model.

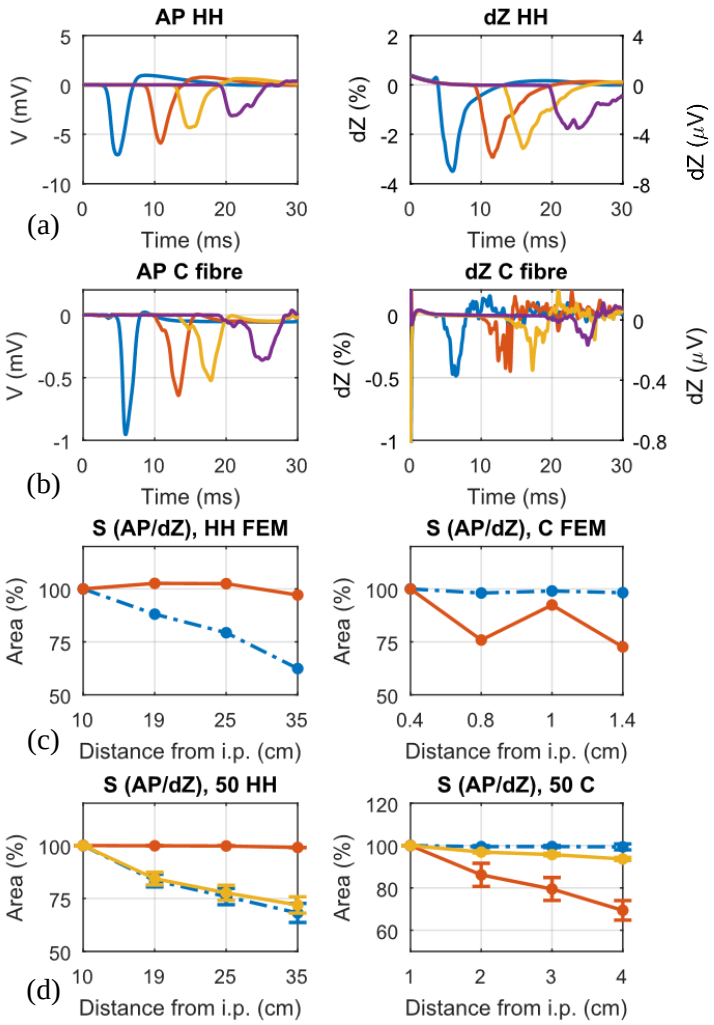

Figure 5.3 Compound AP and dZ of nerves comprising 50 HH axons (left) or C fibres (right) measured at various distances from stimulation using the 3D FEM model (a)-(c) and 100 simplified models (d). dZ are depicted in per cent and in μV for comparison with the simplified model.
(a)-(b) FEM models of HH axon and C fibre;
(c) Normalised integral areas under the CAPs (blue dashed lines) and dZ (red solid lines) vs distance-from AP initiation point (i.p.), FEM model;
(d) Areas under CAP and dZ curves obtained using the simplified 50-fibre models. Blue dashed and red solid lines designate areas under CAPs and dZ measured at DC; yellow lines designate dZ measured with AC current: 1 kHz for HH, 2 kHz for C fibre model. Standard deviations are computed on the basis of 100 random models with the same CV distributions (Table 5.1, eq. (5.1))

5.3.2 C fibres model

At first glance, the FEM model containing 50 C fibres behaved similarly to the one with HH axons: CAP amplitude and compound dZ decreased while their durations increased further from the site of AP initiation (Figure 5.3b).

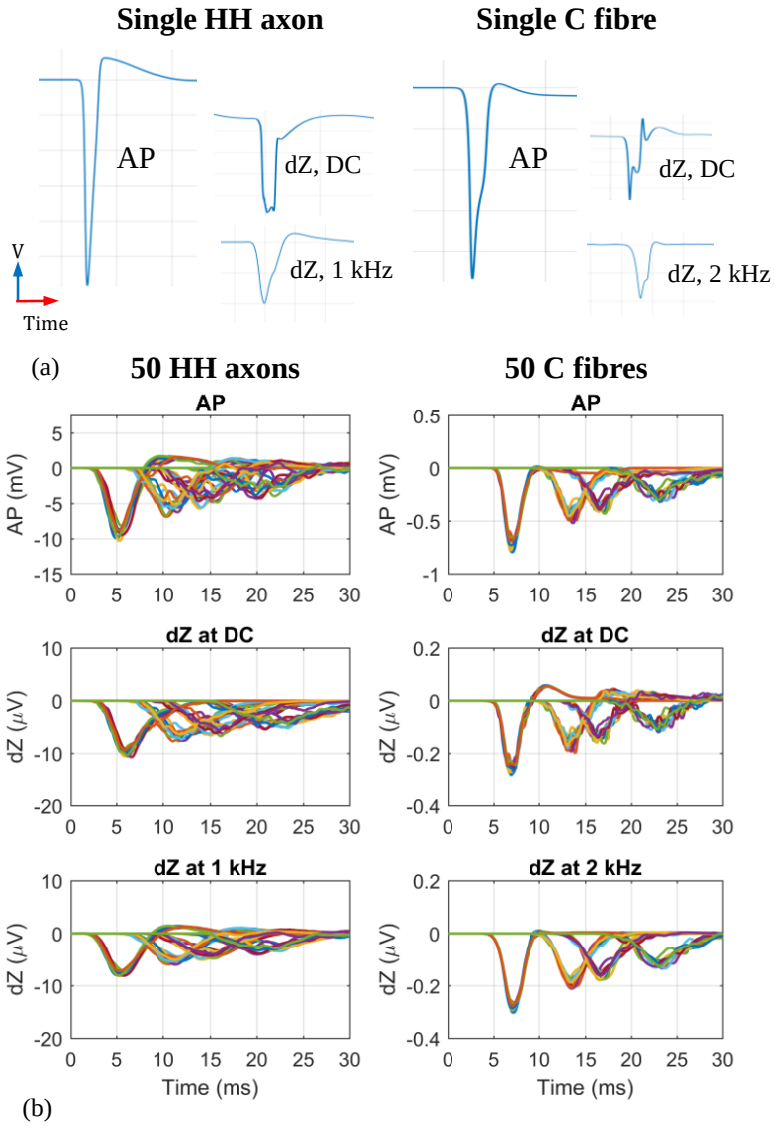

Figure 5.4 Single and compound APs and dZs used in the statistical 50-fibre models for comparison with the FEM models.
(a) Examples of single HH and C fibre APs and dZs used for implementation of the simplified 50-fibre models and for extension to complex nerves. The EIT AC current was 10 times larger than DC to increase the absolute measured dZ. The signals were taken from the models of HH axon and C fibre developed in Chapter 3.
(b) Compound APs and dZs at the same distances as were used in the FEM model (Table 5.1). Lines of different colours represent AP and dZ simulated using different statistical models with the same mean and S.D. parameters (Table 5.2, Table 5.3) to obtain necessary statistics (Figure 5.3d). Velocity distribution of the AP and dZ signals was based on the values of resistivities used in the FEM model (Table 5.1) and their proportionality (5.1). The signals were summarized and scaled due to the increased diameter of the electrode from a single fibre model to 50-fibre model (Table 5.1, details are in the text).

The values of CAP decrease were from 0.95 mV at 0.4 cm to 0.65, 0.5, 0.35 mV at 0.8, 1 and 1.4 cm from the site of stimulus respectively; dZ decreased from -0.5% (-

0.4 μV) to -0.45% (-0.35 μV), -0.44% (-0.34 μV), -0.24% (-0.2 μV) at the same distances. Duration of the negative phases of the dispersed CAP increased from 3 ms at 0.4 cm to 5.5, 7, 9 ms at 0.8, 1 and 1.4 cm from stimulation; dZ durations – 3, 4.5, 6, 7.5 ms (Figure 5.3b).

However, for the C fibre nerve, the dependence of the areas under the compound AP and dZ on the distance from the point of nerve activation were different from the HH nerve (Figure 5.3c). In contrast to the HH model, the area under CAP stayed constant; the area under dZ decreased but fluctuated approximately 80% from the maximum value due to the noise associated with weak convergence of the C fibre FEM model requiring to solve 22 PDEs in parallel (see Discussion).

As for the nerve model with HH axons, a 50-fibre statistical model with C nociceptors was implemented to compute statistics for the obtained values. In the developed model, the CAPs and dZ recorded at DC were in a good agreement to the ones simulated with the FEM model (Figure 5.4b, Figure 5.3b). This made it possible to implement 100 of these models with the same CV distributions as well as to add impedance change measured with an AC current (2 kHz) which was impossible to do with the computationally-heavy FEM model. The same as in the FEM model, areas under the CAP in respect to the area measured at 0.4 cm were practically constant (blue dashed line at Figure 5.3d) at 99.5±0.4%, 99.5±0.5% and 99.3±1.4% at 0.8, 1 and 1.4 cm from the stimulus. In contrast to the HH model, dZ measured at DC decreased with distance from 86±5.3%, to 79.2±5.1% and 68.8±4.0% at the same locations. Compound dZ measured with AC current decreased slower than the one at DC: 97±0.4%, 95.8±0.6%, 93.7±0.8% at the same sites in respect to the dZ measured at 0.4 cm.

5.3.3 Models of mixed diameter fibre nerves

Due to the computational heaviness of the developed 50-fibre FEM models, the simplified statistical models of realistic nerves consisting of nerve fibres of a single type or mixed types were implemented. The parameters utilized for the development

of these models were found experimentally in various studies discussed in the Methods section 5.2.3 (Table 5.2, Table 5.3).

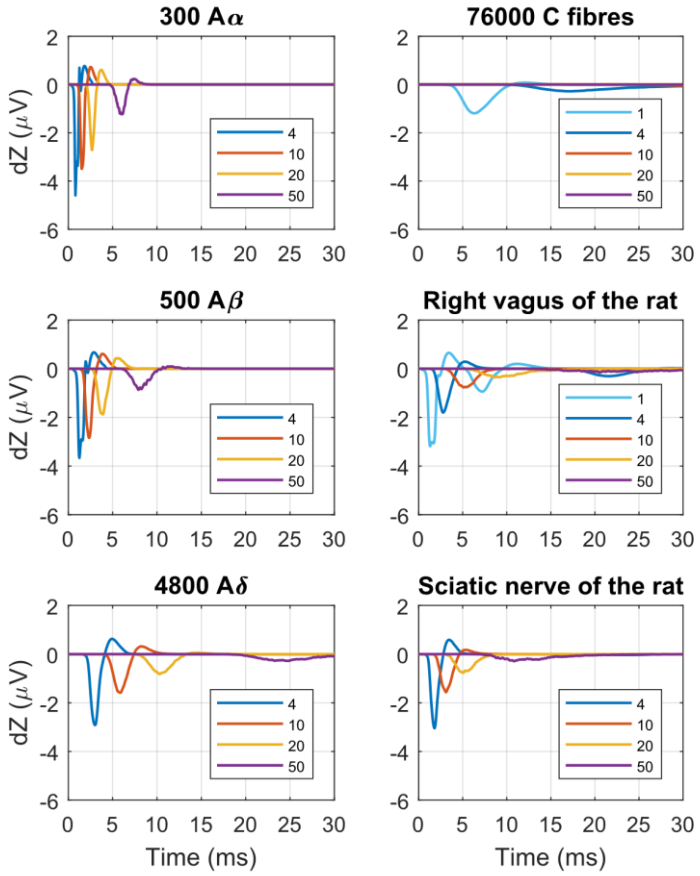

Figure 5.5 Compound dZ simulated for nerves with multiple Aα, Aβ, Aδ or C fibres (Table 5.2) and with realistic rat sciatic and right vagus nerves (Table 5.3).
Compound dZ were formed of single dZ of a C fibre (Figure 5.2) recorded at DC and scaled in time and amplitude depending on the fibre's AP latency and cross-sectional area. The number of fibres in single type models were chosen to fit into a 0.1 mm^2 nerve which approximately equals the size of the rat vagus nerve (Table 5.2). For detailed explanations, see *Methods 5.2.3.*
dZ were computed at different distances from stimulation point: 1, 4, 10, 20 and 50 cm (1 cm was omitted for simplicity in A fibres and sciatic nerve); the colour legend is embedded into the graphs. The average experimental white noise with RMS of 0.5 μV (Aristovich *et al.*, 2018) was added to the recordings after the simulations (Figure 5.2); it was omitted in the figure to improve its readability.

Signal-to-noise ratio decreased with distance from stimulation for all nerves, but the maximum distances at which dZ could be measured were larger for nerves with larger and faster fibres. dZ of 0.1 mm nerves consisting of Aα and Aβ fibres were visible at up to at 50 cm from the stimulus (Figure 5.5) with SNR at DC equalling to 2.7±0.2 and 1.8±0.1 respectively at this location (Figure 5.6). Aδ fibres had sufficient

SNR = 1.6±0.03 at 20 cm from initiation point but it fell below the noise to 0.6±0.02 at 50 cm. These values were similar for rat sciatic nerve with the SNR falling from 1.6±0.06 at 20 cm to 0.6±0.02 at 50 cm making the signal at this distance undetectable. dZ in the right branch of the vagus nerve of the rat consisting of small Aδ and C fibres was visible at 10 cm (SNR = 1.6±0.05) but was indistinguishable at 20 cm where SNR fell below 1. C fibres dZ was only distinguishable at 1 cm from stimulation point with signal-to-noise equalling to 2.4±0.02 there. SNR obtained with the dZ computed at 2 kHz (Figure 5.4a) were in close agreement with the ones at DC (Figure 5.6, Table 5.4). All these results were in fair agreement with experimental data (*Section 5.3.4*).

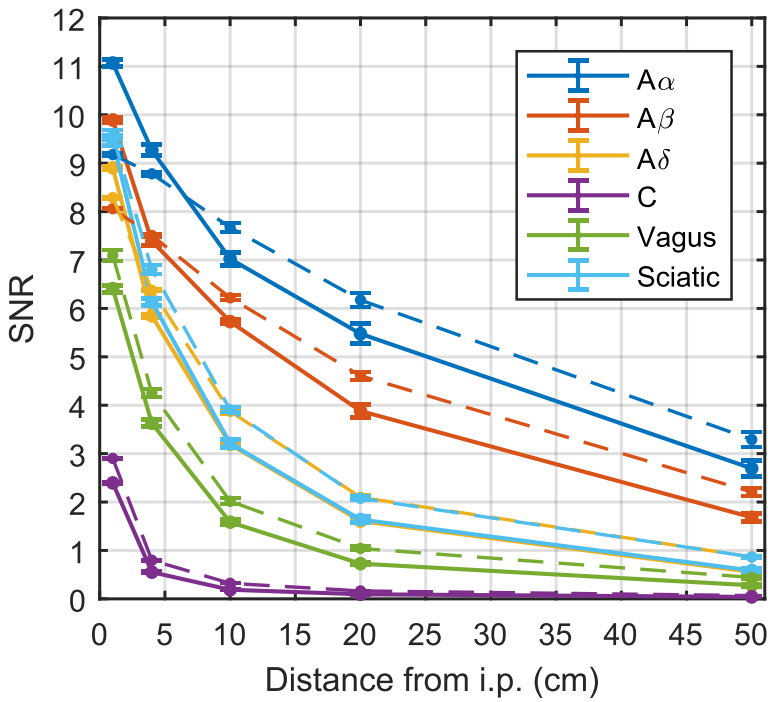

Figure 5.6 Signal to noise ratio (SNR) simulated at various distances from the AP onsite (initiation point, i.p.).
Solid lines represent C fibre dZ recorded at DC, dashed – at 2 kHz (Figure 5.4a). SNR was calculated as a ratio of the pure dZ amplitude to the standard deviation of the noise. Standard deviations of the SNR were computed on the basis of 10 random models for each type of the nerve. The signal was treated undetectable where SNR was below 1. Colour labels are embedded in the figure.

The theoretically maximum distances of dZ measurement where SNR fell below 1 were (Figure 5.6): > 50 cm for Aα and Aβ fibres, ~40 cm for Aδ fibres and the sciatic nerve of the rat, ~15 cm for the rat vagus and about 3 cm for C fibres (Table 5.4).

These distances are at the limit of visibility because, at low values of SNR, a lot of averaging will be necessary to distinguish the sought-for signal from the unwanted noise.

Table 5.4
MIXED DIAMETER FIBRE NERVES MAIN RESULTS

Nerve type	Max. distance*	SNR at DC** (mean ± s.d.)				
		1 cm*	4 cm	10 cm	20 cm	50 cm
Aα	> 50 cm	11.1±0.1	9.2±0.2	7.0±0.2	5.5±0.2	2.7±0.2
Aβ	> 50 cm	9.9±0.1	7.5±0.1	5.7±0.1	4.0±0.1	1.8±0.1
Aδ	40 cm	8.9±0.06	5.9±0.05	3.2±0.05	1.6±0.03	0.6±0.02
C	3 cm	2.4±0.02	0.6±0.01	0.2±0.003	0.1±0.003	< 0.1
Right vagus	15 cm	6.4±0.1	3.7±0.08	1.6±0.05	0.7±0.04	0.3±0.02
Sciatic nerve	40 cm	9.5±0.09	6.2±0.07	3.2±0.06	1.6±0.06	0.6±0.02

* Maximal distance of dZ recording from the onset site
** Calculated as a ratio of the dZ amplitude to the standard deviation of the noise

As was found in (Gilad & Holder, 2009), dZ could be reliably imaged when SNR > 4 which significantly decreases the possible distances to 35 cm for Aα and Aβ fibres, ~8 cm for Aδ and rat sciatic, 4 cm for rat vagus and < 1 cm for C fibres.

5.3.4 Comparison with experimental data

The maximum distances and SNR simulated for different types of fibres and realistic rat vagus and sciatic nerves are in a good agreement with experimental data in the literature. For example, in the experiment on unmyelinated crab nerve (Boone, 1995), the dZ was shown to be visible at up to 16 mm from the onsite. This was in accordance with the modelling as the maximal distance at which the modelled dZ in C-fibre nerve could be seen was found to be ~3 cm (Table 5.4, Figure 5.6).

Low level of CAP dispersion in Aα and Aβ fibres where they could be seen at up to a meter from stimulation was shown in (Olney *et al.*, 1987; Taylor, 1993; Schulte-Mattler *et al.*, 2001); it corresponds to the found low dispersion in dZ for these types

of fibres. High CAP dispersion in C fibres was experimentally demonstrated in (Freeman, 1972; Chang *et al.*, 2015). In particular, CAP of the vagal C fibres of the mouse was shown to fall > 50% at 4 mm (Chang *et al.*, 2015) which is similar to the results simulated for 50 C fibres where CAP decreased ~ 2-fold at 1.4 cm from the site of stimulation (Figure 5.3a, Figure 5.4b); the 50-fibre dispersion is lower due to smaller number of fibres. In (Freeman, 1972), CAP of mainly unmyelinated olfactory nerve of the cat could be recorded at up to 2.5 mm from the stimulus also confirming the large effect of dispersion in C fibres demonstrated in this study. Although the CAP dispersion for complex nerves was not simulated in this chapter, its shape for C fibre closely matches the one of dZ at 2 kHz (Figure 5.4a) which makes them comparable.

In the recently accomplished EIT imaging of rat sciatic nerve (Aristovich *et al.*, 2018), the highest obtained SNR at ~ 4 cm from the onset (length of the rat sciatic nerve) was equal to 8 after averaging which is in fair agreement with the values simulated in this study (SNR = 6.2±0.1 at 4 cm, Figure 5.6). In the same study, the C fibre response was not visible which also agrees with the results in this chapter. The literature on the dispersion for right vagus nerve of the rat was not available, however, the obtained results can be a reference of what to expect in this nerve as well as in human vagus nerve which is the main aim for neuromodulation of the internal organs it supplies.

5.4 Discussion

5.4.1 Summary of results

1) Accurate coupled FEM models of the nerves comprising 50 HH axons or 50 C fibres and their simplified statistical equivalents showed different behaviour of compound AP and dZ with distance from the site of stimulation. In the HH case, the single APs cancel out with distance due to their biphasicity while the dZ measured at DC do not. The inverse was true for the nerve consisting of C fibres

due to differences in the shapes of the studied signals. The dZ recorded at AC current showed the decrease with distance in both models (Figure 5.3d).

Thus, it was revealed that for compound impedance changes to be seen further from the stimulus than compound action potentials, the shape of these signals must satisfy certain condition: dZ needs to be more monophasic than the CAP, as in the case of HH axons at DC (Figure 5.3a, Figure 5.4a).

2) By extension of the study to real nerves consisting of Aα, Aβ, Aδ or C fibres, the theoretical maximal distances at which dZ could be recorded were obtained. These distances were more than 40 cm for a 0.1 mm nerve consisting of A fibres and only up to ~3 cm for the one with C fibres. These findings agree with experimental data on impedance changes and action potentials dispersion (Olney *et al.*, 1987; Taylor, 1993; Boone, 1995; Schulte-Mattler *et al.*, 2001). SNR for rat sciatic nerve at the distance of its length (4 cm) obtained in this study was close to the experimental one (Aristovich *et al.*, 2018). In the same study, C fibres could not be measured, which also agrees with the results obtained in the current work (Figure 5.5, Figure 5.6). Values for the rat vagus nerve were obtained to serve as an expectation guideline for further studies which need to be carried out with a purpose of its subsequent imaging and selective stimulation.

5.4.2 Answers to the stated questions

1. Is it possible to record dZ further than CAP?

The level of dispersion of CAP and dZ signals highly depended on the shape of these signals for each particular case. In general, if multiple phases are significantly expressed in the compound AP of a nerve, the compound dZ may be measured further from the stimulus than the CAP. Such nerves with largely multiphasic extracellularly recorded CAPs include the ones containing many fast fibres like rat sciatic nerve (Aristovich *et al.*, 2018). CAPs recorded in unmyelinated nerves were monophasic (Gilad *et al.*, 2009; Oh *et al.*, 2011) that is in accordance with the current study.

Multiphase structure of the AP does not have the same significance in the impedance change due to the difference in the origin of these signals. Action potentials represent changes in the flow of the current through the membrane while dZ –changes in its impedance. In particular, a negative phase in the AP signal (or positive phase in the extracellular AP, Figure 5.4a) appears mainly due to opening of the potassium ion channels; however, this induces decrease in the impedance, the same as when Na channels open during the positive AP phase (negative EAP). A positive phase in the dZ may be associated either with phase change in the injected AC current (Chapter 3) or with the change in the flow of the injected current around the recording electrode (Chapter 4); this does not change the shape of the AP.

These findings are relevant for assessing the feasibility of EIT imaging inside long autonomic nerves for development of neuromodulation techniques (Famm *et al.*, 2013); the vagus nerve is a good target for them as it has access to various internal organs (Berthoud & Neuhuber, 2000). For this, SNR of spontaneous activity from internal organs in this nerve should be sufficient at the cervical level.

2. Are there differences between models in the effect of dispersion on dZ?

In terms of dZ and CAP dispersion, HH giant axons of the squid and mammalian C fibres differed significantly. Because the single APs and CAPs of the HH model had larger positive phase than C fibres (Figure 5.4), the AP cancellation in the HH case was quicker than in the C fibre case (Figure 5.3); the inverse was true for dZ. Consequently, it is possible to measure dZ further than CAP in the HH case but not in the C fibre case. This result can be extended to nerves made of any fibre types: the more multiphasic the CAP is, the more the increment in distance for dZ measurement can be reached in respect to CAP measurement.

3. What is the largest distance from the site of stimulation at which dZ can be recorded:

a) for nerves consisting of Aα, Aβ, Aδ and C fibres

As may be expected from the values of the standard deviations of the CV of the simulated fibre types as well as their sizes proportional to the dZ amplitude (Table 5.2, Figure 5.2), the dZ decreases with distance significantly slower for the nerve consisting of large fast Aα or Aβ fibres. These nerves produce signals significantly larger than the noise level even at half a meter from the stimulation point. dZ in Aδ nerve was found to be detectable at up to 35 cm; the effect of dispersion becomes much stronger for C fibre nerve where the reliable signal can be obtained up to 2-3 cm from the stimulus (Figure 5.5, Figure 5.6).

The maximum distance of dZ recording which is where SNR approaches 1 is not equal to the SNR required for dZ imaging. It was shown that for reproducible imaging of fast impedance changes, an SNR of 4 is required (Gilad & Holder, 2009) which substantially decreases the above distances.

b) for the realistic vagus and sciatic nerves of the rat.

The SNR of the dZ in the rat sciatic nerve was shown to decrease to 1 at ~35 cm, in the vagus nerve – at 15 cm; these values defined the maximum distances of dZ measurement for these nerves. The SNR values for the sciatic nerve of the rat showed that only A fibres could be imaged at its length (~4 cm) (Figure 5.6) which was in agreement with the experiment (Aristovich *et al.*, 2018). The same was valid for the vagus nerve: its SNR was higher than the one for C fibres (~6 at 1 cm and 1 at 15 cm, Figure 5.6) because it also contained A fibres. However, the majority of its fast-myelinated fibres direct into the motor recurrent laryngeal nerve (Gacek *et al.*, 1977), they cannot be used as a channel for neuromodulation. Conversely, the autonomic part of the vagus leading to the internal organs is mainly unmyelinated (Agostoni *et al.*, 1957), therefore, it is expected to be hardly measured and therefore imaged further than 2-3 cm from the location of stimulation (Results 5.3.3). Thus, an issue arises for imaging its spontaneous activity originating from different organs at a cervical level

located tens of cm away. One possible way to overcome it may be to record for longer periods of time during changes in state.

5.4.3 Limitations and technical difficulties

One of the limitations of the current study was that only one accurate 3D FEM nerve model was undertaken for each nerve type consisting of only 50 fibres. This was due to the lack of computational resources: the C fibre model demanded a system of 22 nonlinear equations (Chapter 3, *Section* 3.2.4) to be solved at the 10^6 FEM elements at each time step which demanded around 100 Gb of RAM and a week of computations on a 2-CPU machine. However, the developed statistical simplifications were in a close agreement with the accurate models in terms of CAPs and dZ amplitudes (Figure 5.3b and Figure 5.4b) and areas (Figure 5.3c, d). Therefore, they were used for performing necessary statistical analysis.

The extension of the models to different types of nerve fibres and realistic nerves relied on experimentally found distributions of CVs and fibre diameters as well as their relation to each other. These values were based on a limited number of studied nerves and therefore were approximate. Also, the choice of scaling coefficients for the transition from the modelled to experimental conditions was based on limited literature and simple assumptions providing qualitative results which were in a fair agreement with the literature. To obtain such results as well as to predict the behaviour of studied signals on various nerves and experimental conditions was the original purpose of the study described in this chapter.

5.5 Conclusion

Due to variability in CVs of fibres composing nerves, it is challenging to record compound activity externally at a distance from a point of stimulation. The effect of dispersion is especially strong in unmyelinated fibres whose CAPs cannot be reliably recorded starting from a few centimetres from initiation. The accurate 50-fibre 3D

FEM and statistical multi-fibre models developed in the study presented in this chapter demonstrated that, for the nerves containing fibres with non-monophasic APs, like HH axons, the evoked impedance changes could be measured and possibly imaged with EIT, at greater distances than CAPs could be recorded. The reason is mainly that the bi-phasic AP of these fibres cancel out when desynchronised while the dZ do not. If taken together with the proportionality of the dZ to nerve cross-sectional area, this enables estimation of the maximal distances at which impedance changes could be measured as well as the SNR expected at these distances. The model predictions are in agreement with the available experimental data.

Chapter 6
Discussion and future work

6.1 Summary of studies

The general purpose of the work presented in this thesis was to study how the variation of experimental parameters affects dZ measurements in nerve fibres and, as a result, to determine the optimal parameters of performing fast neural EIT in nerves. This was accomplished by the development of accurate *in silico* models of unmyelinated and myelinated fibres which were additionally used to validate previously obtained experimental data and to address dispersion – a fundamental limitation of measuring dZ in nerves.

In Chapter 3, 3D FEM models of single and multiple unmyelinated Hodgkin-Huxley axons and the more complex mammalian C fibre were developed. A novel approach designed for bi-directional coupling of the models with external space served as a basis for all further studies carried out in this thesis. The created models were used to confirm the data obtained in previously performed experiments and to simulate fast neural dZ under various external conditions. In all models, negative dZ was the largest at DC and monotonically decreased with frequency approaching zero at around 2 kHz, in accordance with previous experiments (Boone, 1995; Gilad *et al.*, 2009; Oh *et al.*, 2011; Aristovich *et al.*, 2015). Small positive dZs simulated at 2-6 kHz were found to be due to a small phase shift of the measured voltage. Minimization of the distance between the electrodes and their size was found to be necessary for maximization of the measured dZ signals. Multiple fibre models showed that interaction between fibres did not have a substantial effect on dZ which nearly-linearly grew with the number of

fibres. The slope of dZ dependence on frequency simulated with the C fibre model was found to be smaller than that of the standard and spatially modified HH models leading to the conclusion that the complex ion channels play a critical part in the determination of impedance changes.

Chapter 4 covers the extension of the previously developed modelling approach for the creation of a FEM model of a mammalian myelinated fibre. The developed model was the first able to accurately simulate coupling of a myelinated fibre with extracellular space in both directions using the finite element approach. Similar to Chapter 3, this model helped to find the optimal parameters that maximize the measured dZ for further optimisation of fast neural EIT in myelinated fibres. The same as for the case of unmyelinated fibres, the largest dZ was simulated at DC when the distance between the electrodes was minimized. However, due to a high characteristic frequency of the dZ, only AC frequencies above 4 kHz could be used for measurements, in agreement with the recent experimental data (Aristovich *et al.*, 2018). Subtraction of in-phase and in antiphase signals during signal processing raised the dZ magnitudes by approximately two to three times in comparison to the single shot case. Optimal bandwidths for obtaining the maximal dZ were found to increase with the frequency of the applied current in both subtraction and single-shot cases, - optimal frequencies for imaging were found to be 8 kHz and 12 kHz with bandwidths of 7.5 kHz and 3.9 kHz in these cases respectively. In addition, the biophysical origin of the dZ increase observed at DC was determined to be due to redistribution of the injected current under the recording electrode caused by the activity of ion channels of the fibre during the repolarization phase of the AP.

Dispersion in nerves and its influence on the recorded CAP and dZ was studied in Chapter 5. This work was accomplished by the development of 50-fibre FEM models based on the HH and C fibre models from Chapter 3, and statistical models which allowed simulation of complex nerves consisting of thousands of mixed-type fibres. The effect of dispersion was found to be significantly larger in C fibre nerves than in nerves of any other type due to their slow but widely diverging CV (Table 5.4). Maximum distances from the site of stimulation with SNR sufficient for dZ measurements were found to be above 50 cm for A-fibre nerves but only around 2 cm for C fibre nerves. The value of SNR obtained for the sciatic nerve of the rat at 4 cm

from the onset site was close to the experimental one (Aristovich *et al.*, 2018). The models showed that mainly monophasic dZ could potentially be recorded and imaged further from the point of stimulation than multiphasic CAPs.

6.2 Limitations

The general limitation of the performed studies was computational efficiency. The main contribution to long computational times was brought on by bi-directional coupling of 3D or 2D axisymmetric models with the extracellular space. The approach used for its implementation included simultaneous simulation of two pairs of models containing a fibre or extracellular space when the current was or was not applied (Figure 3.2, Figure 3.3). Each model demanded from a couple of hours (HH model) to a couple of days (myelinated and multiple fibre models) to be computed on a 16-core workstation. Therefore, for the possible future implementation of a complete nerve model containing thousands of axons, acceleration of the models is required which can be implemented either by optimisation of the developed modelling approach or by addition of computational power.

The cable model paradigm (Section 2.3.1) used in all the models was applicable for the studied case of long homogeneous fibres with electrodes located far enough from them (Schnabel & Struijk, 2001). This included the myelinated fibre model whose nodal and internodal segments were connected to a single long cable structure (Figure 2.15). The connection of short nodes to long internodes caused irregularities in the solution in the points of attachment, but these irregularities were kept to a minimum by performing a mesh convergence analysis and using finer mesh elements closer to the node (Figure 4.1).

The used model of C fibre provided significantly more accurate results than the HH model, however, the validation data used for the creation of this model is limited to the AP shape, CV and activity-dependent slowing. The same holds for the mammalian myelinated fibre for validation of which CV, shapes of nodal and internodal APs and threshold electrotonus predictions were used. Additional data including excitability properties of fibres under various external conditions or knowledge of which particular

ion channels are present on the membrane would improve the accuracy of simulations. Comparison with other models (McIntyre *et al.*, 2002; Sundt *et al.*, 2015) would also be valuable for assessment of the factors contributing to the precision of the modelled signals.

Quasi-static conditions were used for simulation of the volume conduction in the external space so that inductive, capacitive and propagation effects were neglected. This was a valid assumption according to studies (Plonsey & Heppner, 1967; Bossetti *et al.*, 2008) which showed that inclusion of these effects does not significantly contribute to the accuracy of the simulations even at frequencies up to 100 kHz.

Also, in all performed studies, extracellular space was simulated as a saline solution. Although inclusion of the resistive connective tissue will change the absolute values of the measured dZ, it should not affect their dependence on the experimental parameters.

The models of mixed nerves developed for studying dispersion in Chapter 5 were based on approximate literature data on fibre compositions of the sciatic and vagus nerves of the rat obtained from a limited number of histological samples. Also, transition from the single C fibre model to experimental conditions with multiple fibres and connective tissue was done by introduction of multipliers which were based on the averaged data of tissue conductivities and the percentage of the nerve area occupied by fibres derived from the literature.

The developed models have not been directly experimentally validated as it is challenging to record from a single or a small number of mammalian nerve fibres with diameters in a micrometre range. Special training and equipment are needed to separate single fibres from the nerve and to record from them without inducing damage. Manufacturing of very small electrodes with micrometre diameters and widths as used in the models is also a non-trivial problem. However, simulations performed with a multiple-fibre model in Chapter 3 demonstrated that the rising of dZ magnitudes with the number of fibres was close to linear so that its dependence on experimental parameters remained the same as in the single fibre model. These results suggested that number of fibres should not strongly affect the nature of variation of dZ with experimental parameters which justified the comparison of the modelling results with the experimental data obtained on the whole nerves. Moreover, a full FEM model

of the nerve consisting of thousands of separate fibres would require an enormous amount of computational resources and time to be computed.

6.3 Future work and outlook

A natural expansion of the developed modelling approach is the creation of an accurate 3D model of the nerve with multiple fibres. Such a full model will include myelinated and unmyelinated fibres as well as the connective tissue to have a histologically accurate representation of any nerve of interest so that it can then be used for direct optimisation of fast neural EIT for the same nerve. The starting point can be the vagus nerve, which is currently the most widely studied nerve for development of a novel area of bioelectronic medicines (Waltz, 2016) as its stimulation was shown to have positive effects for the treatment of various illnesses (Ben-Menachem, 2001; Bonaz *et al.*, 2016; Gold *et al.*, 2016; Koopman *et al.*, 2016). The complete accurate model of the vagus nerve will help to find precise optimal parameters for visualisation of its activity in the cross-section with fast neural EIT and aid in adding selectivity to its stimulation.

However, because even single-fibre simulations were very computationally intensive and time consuming, significant acceleration of the models is required which can be implemented in several ways. The first approach is to optimise the developed models so that they require less computational power and therefore less time to compute. This may include division of the models by parts for more effective parallelization, or simplification of the models by eliminating those ion channels playing a non-critical role in dZ generation. Optimisation of a multifibre model can be accomplished by using a set of single fibre simulations with fibres uniformly distributed inside the cylindrical external space, as in Figure 3.1. The results of these simulations at each point of space and time can then be utilised as lookup tables for the transition to multi-fibre simulations using scattered interpolation. Hence, the response of the model would be obtained for any number and location of fibres as well as for any position of the recording electrode. The obvious brute-force approach to acceleration would be to use more powerful computer clusters or potentially GPUs.

The optimal parameters determined with the developed models can aid in optimization of frequency division multiplexing (FDM) and phase division multiplexing (PDM) approaches to imaging neural tissue with EIT (Dowrick & Holder, 2018; Hope *et al.*, 2019). FDM and PDM allow simultaneous AC injection at multiple frequencies and phases for acceleration of obtaining the EIT data set so that high quality EIT images of fast neural activity can potentially be produced in brain and nerves in real time.

Flexibility of the constructed models allows them to be used for the development and optimisation of various techniques involving stimulation or recording from nerves. For example, the novel method which enables inhibition of neural activity by application of high frequency AC currents, known as the conduction block (Patel & Butera, 2018), currently attracts strong interest. By blocking of the specific pathways in peripheral nerves, this technique was shown to be effective for reduction of the symptoms of chronic and acute pain (Soin *et al.*, 2015; Miller *et al.*, 2016) as well as for approaching the treatment of obesity (Apovian *et al.*, 2017). Potential applications may include suppression of pain or hyperactivity during various kinds of injuries or diseases (Patel & Butera, 2018). In addition, conduction block can help to improve selectivity of nerve stimulation by blocking activity in undesired off-target fascicles.

The developed models are either published (Chapter 3, Chapter 5) or under review (Chapter 4) in peer-reviewed scientific journals which makes them available to a broad scientific audience. Apart from optimisation of fast neural EIT or other similar techniques, the models may also be applicable for studying causes and methods for treatment of nerve-related diseases. For example, the myelinated fibre model developed in Chapter 4 may be used for studying how the normal activity of the fibre is affected by demyelination which is responsible for progression of multiple sclerosis. Also, all the created models are suitable for investigation of neuronal behaviour associated with abnormal activity of ion channels and nerve degeneration for approaching the study of conditions like peripheral neuropathy or amyotrophic lateral sclerosis.

Bibliography

Agostoni E, Chinnock JE, Daly MDB & Murray JG (1957). Functional and histological studies of the vagus nerve and its branches to the heart, lungs and abdominal viscera in the cat. *J Physiol* **135,** 182–205.

Agudelo-Toro A & Neef A (2013). Computationally efficient simulation of electrical activity at cell membranes interacting with self-generated and externally imposed electric fields. *J Neural Eng* **10,** 026019.

Altman KW & Plonsey R (1988). Development of a model for point source electrical fibre bundle stimulation. *Med Biol Eng Comput* **26,** 466–475.

Altman KW & Plonsey R (1990). Point source nerve bundle stimulation: Effects of fiber diameter and depth on simulated excitation. *IEEE Trans Biomed Eng* **37,** 688–698.

Apovian CM, Shah SN, Wolfe BM, Ikramuddin S, Miller CJ, Tweden KS, Billington CJ & Shikora SA (2017). Two-Year Outcomes of Vagal Nerve Blocking (vBloc) for the Treatment of Obesity in the ReCharge Trial. *Obes Surg* **27,** 169–176.

Aristovich K, Donegá M, Blochet C, Avery J, Hannan S, Chew DJ & Holder D (2018). Imaging fast neural traffic at fascicular level with electrical impedance tomography: proof of principle in rat sciatic nerve. *J Neural Eng* **15,** 056025.

Aristovich KY, Packham BC, Koo H, Santos GS dos, McEvoy A & Holder DS (2016). Imaging fast electrical activity in the brain with electrical impedance tomography. *Neuroimage* **124,** 204–213.

Aristovich KY, Dos Santos GS & Holder DS (2015). Investigation of potential artefactual changes in measurements of impedance changes during evoked activity: implications to electrical impedance tomography of brain function. *Physiol Meas* **36,** 1245–1259.

Asala S a & Bower a J (1986). An electron microscope study of vagus nerve composition in the ferret. *Anat Embryol (Berl)* **175,** 247–253.

Baillet S, Mosher JC & Leahy RM (2001). Electromagnetic brain mapping. *IEEE Signal Process Mag* **18,** 14–30.

Baker PF, Glitsch HG & Rojas E (1975). Voltage-Dependent Changes in the Permeability of Nerve Membranes to Calcium and Other Divalent Cations [and Discussion]. *Philos Trans R Soc B Biol Sci* **270,** 389–409.

Barr RC & Plonsey R (1992). Electrophysiological interaction through the interstitial space between adjacent unmyelinated parallel fibers. *Biophys J* **61,** 1164–1175.

Basser PJ (1993). Cable equation for a myelinated axon derived from its microstructure. *Med Biol Eng Comput* **31,** S87–S92.

Bayford RH (2006). Bioimpedance Tomography (Electrical Impedance Tomography). *Annu Rev Biomed Eng* **8,** 63–91.

Ben-Menachem E (2001). Vagus nerve stimulation, side effects, and long-term safety. *J Clin Neurophysiol* **18,** 415–418.

Ben-Menachem E (2002). Vagus-nerve stimulation for the treatment of epilepsy. *Lancet Neurol* **1,** 477–482.

Berthold C-H & Rydmark M (1983). Anatomy of the paranode-node-paranode region in the cat ed. Allgair JA & Raymond CJ. *Experientia* **39,** 964–976.

Berthoud HR & Neuhuber WL (2000). Functional and chemical anatomy of the afferent vagal system. *Auton Neurosci Basic Clin* **85,** 1–17.

Birren JE & Wall PD (1956). Age changes in conduction velocity, refractory period, number of fibers, connective tissue space and blood vessels in sciatic nerve of rats. *J Comp Neurol* **104,** 1–16.

Bischoff U, Vogel W & Safronov B V (1998). Na + -activated K + channels in small dorsal root ganglion neurones of rat. *J Physiol* **510,** 743–754.

Blair NT & Bean BP (2002). Roles of tetrodotoxin (TTX)-sensitive Na+ current, TTX-resistant Na+ current, and Ca2+ current in the action potentials of nociceptive sensory neurons. *J Neurosci* **22,** 10277–10290.

Blight AR (1985). Computer simulation of action potentials and afterpotentials in mammalian myelinated axons: The case for a lower resistance myelin sheath. *Neuroscience* **15,** 13–31.

Bonaz B, Sinniger V & Pellissier S (2016). Anti-inflammatory properties of the vagus nerve: potential therapeutic implications of vagus nerve stimulation. *J Physiol* **594,** 5781–5790.

Boone KG (1995). *The possible use of applied potential tomography for imaging action potentials in the brain* (thesis). University College London.

Bossetti CA, Birdno MJ & Grill WM (2008). Analysis of the quasi-static approximation for calculating potentials generated by neural stimulation. *J Neural Eng* **5,** 44–53.

Bostock BYH, Baker M & Reid G (1991). Changes in Excitability of Human Motor Axons Underlying Post-Ischaemic Fasciculation: Evidence for Two Stable States. *J Physiol* **441,** 537–557.

Boyd IA & Kalu KU (1979). Scaling factor relating conduction velocity and diameter for myelinated afferent nerve fibres in the cat hind limb. *J Physiol* **289,** 277–297.

Brown DA & Adams PR (1980). Muscarinic suppression of a novel voltage-sensitive K+ current in a vertebrate neurone. *Nature* **283,** 673–676.

Campbell DT (1992). Large and small vertebrate sensory neurons express different Na and K channel subtypes. *Proc Natl Acad Sci* **89,** 9569–9573.

Castelfranco AM & Hartline DK (2016). Evolution of rapid nerve conduction. *Brain Res* **1641,** 11–33.

Chang RB, Strochlic DE, Williams EK, Umans BD & Liberles SD (2015). Vagal Sensory Neuron Subtypes that Differentially Control Breathing. *Cell* **161,** 622–633.

Chapman CAR, Aristovich K, Donega M, Fjordbakk CT, Stathopoulou T, Viscasillas J, Avery J, Perkins JD & Holder D (2019). Electrode fabrication and interface optimization for imaging of evoked peripheral nervous system activity with electrical impedance tomography (EIT). *J Neural Eng* **16,** 016001.

Choi AQQ, Cavanaugh JKK & Durand DMM (2001). Selectivity of multiple-contact nerve cuff electrodes: a simulation analysis. *IEEE Trans Biomed Eng* **48,** 165–172.

Christian EP & Togo JA (1995). Excitable properties and underlying Na+ and K+ currents in neurons from the guinea-pig jugular ganglion. *J Auton Nerv Syst* **56,** 75–86.

Clancy CE & Rudy Y (1999). Linking a genetic defect to its cellular phenotype in a cardiac arrhythmia. *Nature* **400,** 566–569.

Clark JW & Plonsey R (1971). Fiber Interaction in a Nerve Trunk. *Biophys J* **11,** 281–294.

Cole KS & Cole RH (1941). Dispersion and Absorption in Dielectrics I. Alternating Current Characteristics. *J Chem Phys* **9,** 341–351.

Cole KS & Curtis HJ (1938). Electric impedance of Nitella during activity. *J Gen Physiol* **22,** 37–64.

Cole KS & Curtis HJ (1939). Electric Impedance of the Squid Giant Axon During Activity. *J Gen Physiol* **22,** 649–670.

Coleridge JCG & Coleridge HM (1984). Afferent vagal C fibre innervation of the lungs and airways and its functional significance. In *Reviews of physiology, biochemistry and pharmacology*, pp. 1–110.

Cooper E (1989). Inactivation of A currents and A channels on rat nodose neurons in culture. *J Gen Physiol* **94,** 881–910.

Cross KP & Robertson RM (2016). Ionic mechanisms maintaining action potential conduction velocity at high firing frequencies in an unmyelinated axon. *Physiol Rep* **4,** 1–18.

Csicsvari J, Hirase H, Czurkó A, Mamiya A & Buzsáki G (1999). Oscillatory Coupling of Hippocampal Pyramidal Cells and Interneurons in the Behaving Rat. *J Neurosci* **19,** 274–287.

David G, Modney B, Scappaticci KA, Barrett JN & Barrett EF (1995). Electrical and morphological factors influencing the depolarizing after???potential in rat and lizard myelinated axons. *J Physiol* **489,** 141–157.

DiFrancesco D, Ferroni A, Mazzanti M & Tromba C (1986). Properties of the hyperpolarizing-activated current (if) in cells isolated from the rabbit sino-atrial node. *J Physiol* **377,** 61–88.

Dimitrov AG (2009). A possible mechanism of repetitive firing of myelinated axon. *Pflugers Arch Eur J Physiol* **458,** 547–561.

Djouhri L, Newton R, Levinson SR, Berry CM, Carruthers B & Lawson SN (2003). Sensory and electrophysiological properties of guinea-pig sensory neurones expressing Nav 1.7 (PN1) Na+ channel α subunit protein. *J Physiol* **546,** 565–576.

Dorfman LJ (1984). The distribution of conduction velocities (DCV) in peripheral nerves: A review. *Muscle Nerve* **7,** 2–11.

Dowrick T & Holder D (2018). Phase division multiplexed EIT for enhanced temporal resolution. *Physiol Meas* **39,** 034005.

Durand D (1984). The somatic shunt cable model for neurons. *Biophys J* **46,** 645–653.

Elia S & Lamberti P (2013). The Reproduction of the Physiological Behaviour of the Axon of Nervous Cells by Means of Finite Element Models. In *Innovations in Intelligent Machines -3.Studies in Computational Intelligence*, pp. 69–87.

Springer Berlin Heidelberg. Available at: http://link.springer.com/10.1007/978-3-642-32177-1_5.

Eymard R, Gallouët T & Herbin R (2000). Finite volume methods. In *Computing*, pp. 713–1018. Taylor & Francis.

Eyuboglu BM, Brown BH, Barber DC & Seager AD (1987). Localisation of cardiac related impedance changes in the thorax. *Clin Phys Physiol Meas* **8,** 167–173.

Famm K, Litt B, Tracey KJ, Boyden ES & Slaoui M (2013). A jump-start for electroceuticals. *Nature* **496,** 159–161.

Faulkner M, Hannan S, Aristovich K, Avery J & Holder D (2018*a*). Feasibility of imaging evoked activity throughout the rat brain using electrical impedance tomography. *Neuroimage* **178,** 1–10.

Faulkner M, Hannan S, Aristovich K, Avery J & Holder D (2018*b*). Characterising the frequency response of impedance changes during evoked physiological activity in the rat brain. *Physiol Meas* **39,** 034007.

Finn W & LoPresti P eds. (2002). *Handbook of Neuroprosthetic Methods*. CRC Press. Available at: https://www.taylorfrancis.com/books/9781420040876.

Fitzhugh R (1962). Computation of impulse initiation and saltatory conduction in a myelinated nerve fiber. *Biophys J* **2,** 11–21.

Fitzhugh R (1966). Theoretical Effect of Temperature on Threshold in the Hodgkin-Huxley Nerve Model. *J Gen Physiol* **49,** 989–1005.

Frankenhaeuser B & Huxley AF (1964). The action potential in the myelinated nerve fibre of Xenopus laevis as computed on the basis of voltage clamp data. *J Physiol* **171,** 302–315.

Freeman WJJ (1972). Spatial Divergence and Temporal Dispersion in Primary Olfactory Nerve of Cat. *J Neurophysiol* **35,** 733-.

Frerichs I (2000). Electrical impedance tomography (EIT) in applications related to lung and ventilation: a review of experimental and clinical activities. *Physiol Meas* **21,** R1–R21.

Gacek RR, Malmgren LT & Lyon MJ (1977). Localization of adductor and abductor motor nerve fibers to the larynx. *Ann Otol Rhinol Laryngol* **86,** 770–776.

Gasser HS (1950). Unmedullated fibers originating in dorsal root ganglia. *J Gen Physiol* **33,** 651–690.

Ghitani N, Barik A, Szczot M, Thompson JH, Li C, Le Pichon CE, Krashes MJ & Chesler AT (2017). Specialized Mechanosensory Nociceptors Mediating Rapid Responses to Hair Pull. *Neuron* **95,** 944-954.e4.

Gilad O, Ghosh A, Oh D & Holder DS (2009). A method for recording resistance changes non-invasively during neuronal depolarization with a view to imaging brain activity with electrical impedance tomography. *J Neurosci Methods* **180,** 87–96.

Gilad O & Holder DS (2009). Impedance changes recorded with scalp electrodes during visual evoked responses: Implications for Electrical Impedance Tomography of fast neural activity. *Neuroimage* **47,** 514–522.

Gold C, Henze DA, Koch C & Buzsáki G (2006). On the origin of the extracellular action potential waveform: A modeling study. *J Neurophysiol* **95,** 3113–3128.

Gold MR, Van Veldhuisen DJ, Hauptman PJ, Borggrefe M, Kubo SH, Lieberman RA, Milasinovic G, Berman BJ, Djordjevic S, Neelagaru S, Schwartz PJ, Starling RC & Mann DL (2016). Vagus Nerve Stimulation for the Treatment of Heart Failure.

J Am Coll Cardiol **68,** 149–158.

Goldin AL, Barchi RL, Caldwell JH, Hofmann F, Howe JR, Hunter JC, Kallen RG, Mandel G, Meisler MH, Netter YB, Noda M, Tamkun MM, Waxman SG, Wood JN & Catterall WA (2000). Nomenclature of Voltage-Gated Sodium Channels. *Neuron* **28,** 365–368.

Goldman L & Albus JS (1968). Computation of impulse conduction in myelinated fibers; theoretical basis of the velocity-diameter relation. *Biophys J* **8,** 596–607.

Grafe P, Quasthoff S, Grosskreutz J & Alzheimer C (1997). Function of the hyperpolarization-activated inward rectification in nonmyelinated peripheral rat and human axons. *J Neurophysiol* **77,** 421–426.

Greenberg RJ, Veite TJ, Humayun MS, Scarlatis GN & De Juan E (1999). A computational model of electrical stimulation of the retinal ganglion cell. *IEEE Trans Biomed Eng* **46,** 505–514.

Hallin RG & Torebjörk HE (1973). Electrically induced A and C fibre responses in intact human skin nerves. *Exp Brain Res* **16,** 309–320.

Halter JA & Clark JW (1991). A distributed-parameter model of the myelinated nerve fiber. *J Theor Biol* **148,** 345–382.

Hämäläinen M, Hari R, Ilmoniemi RJ, Knuutila J & Lounasmaa O V. (1993). Magnetoencephalography—theory, instrumentation, and applications to noninvasive studies of the working human brain. *Rev Mod Phys* **65,** 413–497.

Hannan S, Faulkner M, Aristovich K, Avery J, Walker M & Holder D (2018). Imaging fast electrical activity in the brain during ictal epileptiform discharges with electrical impedance tomography. *NeuroImage Clin* **20,** 674–684.

Hannan S, Faulkner M, Aristovich KY, Avery J & Holder DS (2019). Investigating the safety of fast neural electrical impedance tomography in the rat brain. *Physiol Meas*; DOI: 10.1088/1361-6579/ab0d53.

Harper AA & Lawson SN (1985). Electrical properties of rat dorsal root ganglion neurones with different peripheral nerve conduction velocities. *J Physiol* **359,** 47–63.

Harrach B (2019). Uniqueness and Lipschitz stability in electrical impedance tomography with finitely many electrodes. *Inverse Probl* **35,** 024005.

Henze DA, Borhegyi Z, Csicsvari J, Mamiya A, Harris KD & Buzsáki G (2000). Intracellular Features Predicted by Extracellular Recordings in the Hippocampus In Vivo. *J Neurophysiol* **84,** 390–400.

Herzog RI, Cummins TR & Waxman SG (2001). Persistent TTX-resistant Na+ current affects resting potential and response to depolarization in simulated spinal sensory neurons. *J Neurophysiol* **86,** 1351–1364.

Hille B (2001). *Ionic Channels of Excitable Membranes*, 3rd edn. Sinauer Associates, Sunderland.

Hillman EMC (2007). Optical brain imaging in vivo: techniques and applications from animal to man. *J Biomed Opt* **12,** 051402.

Hindmarsh AC, Brown PN, Grant KE, Lee SL, Serban R, Shumaker DE & Woodward CS (2005). SUNDIALS: Suite of nonlinear and differential/algebraic equation solvers. *ACM Trans Math Softw* **31,** 363–396.

Hines ML & Carnevale NT (1997). The NEURON Simulation Environment. *Neural Comput* **9,** 1179–1209.

Hodgkin AL & Huxley AF (1952). A quantitative description of membrane current

and its application to conduction and excitation in nerve. *J Physiol* **117,** 500–544.

Hodgkin AL, Huxley AF & Katz B (1952). Measurement of current-voltage relations in the membrane of the giant axon of Loligo. *J Physiol* **116,** 424–448.

Hodgkin AL & Rushton WAH (1946). The Electrical Constants of a Crustacean Nerve Fibre. *Proc R Soc B Biol Sci* **133,** 444–479.

Holder D (2004*a*). Introduction to biomedical electrical impedance tomography. In *Electrical Impedance Tomography: Methods, History and Applications*, pp. 423–451. Taylor & Francis, London.

Holder D (2004*b*). Brief introduction to bioimpedance. In *Electrical Impedance Tomography: Methods, History and Applications*, pp. 411–422. Taylor & Francis, London.

Holder DS (1992). Impedance changes during the compound nerve action potential: Implications for impedance imaging of neuronal depolarisation in the brain. *Med Biol Eng Comput* **30,** 140–146.

Holt GR (1998). *A critical Reexamination of some assumptions and implications of cable theory in neurobiology* (thesis). California Institute of Technology.

Holt GR & Koch C (1999). Electrical interactions via the extracellular potential near cell bodies. *J Comput Neurosci* **6,** 169–184.

Homma T & Saltelli A (1996). Importance measures in global sensitivity analysis of nonlinear models. *Reliab Eng Syst Saf* **52,** 1–17.

Hope J, Aristovich K, Chapman CAR, Volschenk A, Vanholsbeeck F & McDaid A (2019). Extracting impedance changes from a frequency multiplexed signal during neural activity in sciatic nerve of rat: preliminary study in vitro. *Physiol Meas* **40,** 034006.

Hope J, Vanholsbeeck F & McDaid A (2018). A model of electrical impedance tomography implemented in nerve-cuff for neural-prosthetics control. *Physiol Meas* **39,** 044002.

Horton NG, Wang K, Kobat D, Clark CG, Wise FW, Schaffer CB & Xu C (2013). In vivo three-photon microscopy of subcortical structures within an intact mouse brain. *Nat Photonics* **7,** 205–209.

Howells J, Trevillion L, Bostock H & Burke D (2012). The voltage dependence of I h in human myelinated axons. *J Physiol* **590,** 1625–1640.

Jihwan Woo, Miller CA & Abbas PJ (2009). Biophysical Model of an Auditory Nerve Fiber With a Novel Adaptation Component. *IEEE Trans Biomed Eng* **56,** 2177–2180.

Johnston D & Wu SM-S (1995). *Foundations of cellular neurophysiology*. MIT press., Cambridge.

Karschin A, Brockhaus J, Ballanyi K, Institut IIP, Universit G & D- G (1998). K ATP channel formation by the sulphonylurea receptors SUR1. *J Physiol*339–346.

Kiernan MC, Mogyoros I & Burke D (1996). Differences in the recovery of excitability in sensory and motor axons of human median nerve. *Brain* **119 (Pt 4,** 1099–1105.

Kiss T (2008). Persistent Na-channels: Origin and function. *Acta Biol Hung* **59,** 1–12.

Koopman FA, Chavan SS, Miljko S, Grazio S, Sokolovic S, Schuurman PR, Mehta AD, Levine YA, Faltys M, Zitnik R, Tracey KJ & Tak PP (2016). Vagus nerve stimulation inhibits cytokine production and attenuates disease severity in rheumatoid arthritis. *Proc Natl Acad Sci U S A* **113,** 8284–8289.

Kouranova E V., Strassle BW, Ring RH, Bowlby MR & Vasilyev D V. (2008). Hyperpolarization-activated cyclic nucleotide-gated channel mRNA and protein expression in large versus small diameter dorsal root ganglion neurons: Correlation with hyperpolarization-activated current gating. *Neuroscience* **153,** 1008–1019.

Kunkel MT & Peralta EG (1995). Identification of domains conferring G protein regulation on inward rectifier potassium channels. *Cell* **83,** 443–449.

Lionheart W, Polydorides N & Borsic A (2004). The reconstruction problem. In *Electrical Impedance Tomography: Methods, History and Applications*, ed. Holder DS, pp. 3–64. Taylor & Francis.

Liston A, Bayford R & Holder D (2012). A cable theory based biophysical model of resistance change in crab peripheral nerve and human cerebral cortex during neuronal depolarisation: implications for electrical impedance tomography of fast neural activity in the brain. *Med Biol Eng Comput* **50,** 425–437.

Llano I (1988). Potassium conductance of the squid giant axon. Single-channel studies. *J Gen Physiol* **92,** 179–196.

Lubba CH, Le Guen Y, Jarvis S, Jones NS, Cork SC, Eftekhar A & Schultz SR (2019). PyPNS: Multiscale Simulation of a Peripheral Nerve in Python. *Neuroinformatics* **17,** 63–81.

Lüthi A & McCormick DA (1998). H-current: Properties of a neuronal and network pacemaker. *Neuron* **21,** 9–12.

Maingret F, Coste B, Padilla F, Clerc N, Crest M, Korogod SM & Delmas P (2008). Inflammatory mediators increase Nav1.9 current and excitability in nociceptors through a coincident detection mechanism. *J Gen Physiol* **131,** 211–225.

Martinek J, Stickler Y, Reichel M, Mayr W & Rattay F (2008). A novel approach to simulate Hodgkin-Huxley-like excitation with COMSOL Multiphysics. *Artif Organs* **32,** 614–619.

Maynard EM, Nordhausen CT & Normann RA (1997). The Utah Intracortical Electrode Array: A recording structure for potential brain-computer interfaces. *Electroencephalogr Clin Neurophysiol* **102,** 228–239.

McAlexander MA & Undem BJ (2000). Potassium channel blockade induces action potential generation in guinea-pig airway vagal afferent neurones. *J Auton Nerv Syst* **78,** 158–164.

McIntyre CC, Richardson AG & Grill WM (2002). Modeling the excitability of mammalian nerve fibers: influence of afterpotentials on the recovery cycle. *J Neurophysiol* **87,** 995–1006.

McNeal DR (1976). Analysis of a Model for Excitation of Myelinated Nerve. *IEEE Trans Biomed Eng* **BME-23,** 329–337.

Meves H & Vogel W (1973). Calcium inward currents in internally perfused giant axons. *J Physiol* **235,** 225–265.

Miller JP, Eldabe S, Buchser E, Johanek LM, Guan Y & Linderoth B (2016). Parameters of Spinal Cord Stimulation and Their Role in Electrical Charge Delivery: A Review. *Neuromodulation* **19,** 373–384.

Mountcastle VB, Talbot WH, Sakata H & Hyvärinen J (1969). Cortical neuronal mechanisms in flutter-vibration studied in unanesthetized monkeys. Neuronal periodicity and frequency discrimination. *J Neurophysiol* **32,** 452–484.

De Neef KJ, Jansen JRC & Versprille A (1982). Developmental morphometry and

physiology of the rabbit vagus nerve. *Dev Brain Res* **4,** 265–274.

Neher E & Sakmann B (1976). Single-channel currents recorded from membrane of denervated frog muscle fibres. *Nature* **260,** 799–802.

Ntziachristos V (2010). Going deeper than microscopy: the optical imaging frontier in biology. *Nat Methods* **7,** 603–614.

Ogawa S, Menon RS, Kim S-G & Ugurbil K (1998). On the characteristics of functional magnetic resonance imaging of the brain. *Annu Rev Biophys Biomol Struct* **27,** 447–474.

Oh T, Gilad O, Ghosh A, Schuettler M & Holder DS (2011). A novel method for recording neuronal depolarization with recording at 125–825 Hz: implications for imaging fast neural activity in the brain with electrical impedance tomography. *Med Biol Eng Comput* **49,** 593–604.

Ollinger JM & Fessler JA (1997). Positron-emission tomography. *IEEE Signal Process Mag* **14,** 43–55.

Olney RK, Budingen HJ & Miller RG (1987). The effect of temporal dispersion on compound action potential area in human peripheral nerve. *Muscle Nerve* **10,** 728–733.

Ouzounov DG, Wang T, Wang M, Feng DD, Horton NG, Cruz-Hernández JC, Cheng Y-T, Reimer J, Tolias AS, Nishimura N & Xu C (2017). In vivo three-photon imaging of activity of GCaMP6-labeled neurons deep in intact mouse brain. *Nat Methods* **14,** 388–390.

Patel YA & Butera RJ (2018). Challenges associated with nerve conduction block using kilohertz electrical stimulation. *J Neural Eng* **15,** aaadc0.

Pelot NA, Behrend CE & Grill WM (2017). Modeling the response of small myelinated axons in a compound nerve to kilohertz frequency signals. *J Neural Eng* **14,** 046022.

Pelot NA, Behrend CE & Grill WM (2019). On the parameters used in finite element modeling of compound peripheral nerves. *J Neural Eng* **16,** 016007.

Pepper DW (2017). *The Finite Element Method*. CRC Press.

Pine J (1980). Recording action potentials from cultured neurons with extracellular microcircuit electrodes. *J Neurosci Methods* **2,** 19–31.

Plonsey R & Heppner DB (1967). Considerations of quasi-stationarity in electrophysiological systems. *Bull Math Biophys* **29,** 657–664.

Prechtl JC & Powley TL (1987). A light and electron microscopic examination of the vagal hepatic branch of the rat. *Anat Embryol (Berl)* **176,** 115–126.

Qiao S & Yoshida K (2013). Influence of unit distance and conduction velocity on the spectra of extracellular action potentials recorded with intrafascicular electrodes. *Med Eng Phys* **35,** 116–124.

Raspopovic S, Capogrosso M & Micera S (2011). A computational model for the stimulation of rat sciatic nerve using a transverse intrafascicular multichannel electrode. *IEEE Trans Neural Syst Rehabil Eng* **19,** 333–344.

Rattay F (1989). Analysis of Models for Extracellular Fiber Stimulation. *IEEE Trans Biomed Eng* **36,** 676–682.

Rattay F (1999). The basic mechanism for the electrical stimulation of the nervous system. *Neuroscience* **89,** 335–346.

Rushton WAH (1951). A theory of the effects of fibre size in medullated nerve. *J Physiol* **115,** 101–122.

Sadleir R (2010). A bidomain model for neural tissue. *Int J Bioelectromag* **12,** 2–6.

Sadleir RJ, Fu F & Chauhan M (2019). Functional magnetic resonance electrical impedance tomography (fMREIT) sensitivity analysis using an active bidomain finite-element model of neural tissue. *Magn Reson Med* **81,** 602–614.

Schenk O & Gärtner K (2004). Solving unsymmetric sparse systems of linear equations with PARDISO. *Futur Gener Comput Syst* **20,** 475–487.

Schiefer MA, Triolo RJ & Tyler DJ (2008). A model of selective activation of the femoral nerve with a flat interface nerve electrode for a lower extremity neuroprosthesis. *IEEE Trans Neural Syst Rehabil Eng* **16,** 195–204.

Schmalbruch H (1986). Fiber composition of the rat sciatic nerve. *Anat Rec* **215,** 71–81.

Schmidt RF & Thews G (1989). Information Transfer by Electrical Excitation. In *Human Physiology,* 2nd edn., pp. 19–42. Springer, Berlin, Heidelberg.

Schnabel V & Struijk JJ (2001). Evaluation of the cable model for electrical stimulation of unmyelinated nerve fibers. *IEEE Trans Biomed Eng* **48,** 1027–1033.

Schulte-Mattler WJ, Müller T, Georgiadis D, Kornhuber ME & Zierz S (2001). Length dependence of variables associated with temporal dispersion in human motor nerves. *Muscle and Nerve* **24,** 527–533.

Schwan HP & Ferris CD (1968). Four-electrode null techniques for impedance measurement with high resolution. *Rev Sci Instrum* **39,** 481–485.

Scriven DR (1981). Modeling repetitive firing and bursting in a small unmyelinated nerve fiber. *Biophys J* **35,** 715–730.

Shapeev A V & Lin P (2009). An Asymptotic Fitting Finite Element Method with Exponential Mesh Refinement for Accurate Computation of Corner Eddies in Viscous Flows. *SIAM J Sci Comput* **31,** 1874–1900.

Sheets PL, Jackson JO, Waxman SG, Dib-Hajj SD & Cummins TR (2007). A Nav1.7 channel mutation associated with hereditary erythromelalgia contributes to neuronal hyperexcitability and displays reduced lidocaine sensitivity. *J Physiol* **581,** 1019–1031.

Shimizu T, Hayashi M, Kawata A, Mizutani T, Watabe K & Matsubara S (2011). A morphometric study of the vagus nerve in amyotropic lateral sclerosis with circulatory collapse. *Amyotroph Lateral Scler* **12,** 356–362.

Smallwood RH, Mangnall YF & Leathard AD (1994). Transport of gastric contents (electric impedance imaging). *Physiol Meas* **15,** A175–A188.

Smith GD (1985). *Numerical solution of partial differential equations: finite difference methods*. Oxford University Press.

Soin A, Syed Shah N & Fang ZP (2015). High-frequency electrical nerve block for postamputation pain: A pilot study. *Neuromodulation* **18,** 197–205.

Soltanpour N & Santer RM (1996). Preservation of the cervical vagus nerve in aged rats: Morphometric and enzyme histochemical evidence. *J Auton Nerv Syst* **60,** 93–101.

Soni NK, Paulsen KD, Dehghani H & Hartov A (2006). Finite element implementation of Maxwell's equations for image reconstruction in electrical impedance tomography. *IEEE Trans Med Imaging* **25,** 55–61.

Stephanova DI (2001). Myelin as longitudinal conductor: A multi-layered model of the myelinated human motor nerve fibre. *Biol Cybern* **84,** 301–308.

Stephanova DI & Bostock H (1995). A distributed-parameter model of the myelinated human motor nerve fibre: temporal and spatial distributions of action potentials and ionic currents. *Biol Cybern* **73,** 275–280.

Stephanova DI & Bostock H (1996). A distributed-parameter model of the myelinated human motor nerve fibre: temporal and spatial distributions of electrotonic potentials and ionic currents. *Biol Cybern* **74,** 543–547.

Strassberg AF & DeFelice LJ (1993). Limitations of the Hodgkin-Huxley Formalism: Effects of Single Channel Kinetics on Transmembrane Voltage Dynamics. *Neural Comput* **5,** 843–855.

Sundt D, Gamper N & Jaffe DB (2015). Spike propagation through the dorsal root ganglia in an unmyelinated sensory neuron: a modeling study. *J Neurophysiol* **114,** 3140–3153.

Taylor PK (1993). CMAP dispersion, amplitude decay, and area decay in a normal population. *Muscle Nerve* **16,** 1181–1187.

Thalhammer JG, Raymond S a, Popitz-Bergez F a & Strichartz GR (1994). Modality-dependent modulation of conduction by impulse activity in functionally characterized single cutaneous afferents in the rat. *Somatosens Mot Res* **11,** 243–257.

Tigerholm J, Petersson ME, Obreja O, Lampert A, Carr R, Schmelz M & Fransén E (2014). Modeling activity-dependent changes of axonal spike conduction in primary afferent C-nociceptors. *J Neurophysiol* **111,** 1721–1735.

Toledo-Aral JJ, Moss BL, He Z-J, Koszowski AG, Whisenand T, Levinson SR, Wolf JJ, Silos-Santiago I, Halegoua S & Mandel G (1997). Identification of PN1, a predominant voltage-dependent sodium channel expressed principally in peripheral neurons. *Proc Natl Acad Sci* **94,** 1527–1532.

Torebjo¨rk HE & Hallin RG (1974). Identification of afferent C units in intact human skin nerves. *Brain Res* **67,** 387–403.

Verlinden TJM, Rijkers K, Hoogland G & Herrler A (2016). Morphology of the human cervical vagus nerve: implications for vagus nerve stimulation treatment. *Acta Neurol Scand* **133,** 173–182.

Vongerichten A (2015). *Imaging Physiological and Pathological Activity in the Brain using Electric Impedance Tomography* (thesis). University College London.

Waltz E (2016). A spark at the periphery. *Nat Biotechnol* **34,** 904–908.

Wang B, Aberra AS, Grill WM & Peterchev A V (2018). Modified cable equation incorporating transverse polarization of neuronal membranes for accurate coupling of electric fields. *J Neural Eng* **15,** 026003.

Warman EN, Grill WM & Durand D (1992). Modeling the Effects of Electric Fields on Nerve Fibers: Determination of Excitation Thresholds. *IEEE Trans Biomed Eng* **39,** 1244–1254.

Waxman SG (1980). Determinants of conduction velocity in myelinated nerve fibers. *Muscle Nerve* **3,** 141–150.

Yang Q, Kaji R, Hirota N, Kojima Y, Takagi T, Kohara N, Kimura J, Shibasaki H & Bostock H (2000). Effect of maturation on nerve excitability in an experimental model of threshold electrotonus. *Muscle and Nerve* **23,** 498–506.

Yin S, Dokos S & Lovell NH (2013). Bidomain Modeling of Neural Tissue. In *Neural Engineering*, pp. 389–404. Springer US, Boston, MA.

Yoshida Kozai TD, Langhals NB, Patel PR, Deng X, Zhang H, Smith KL, Lahann J,

Kotov NA & Kipke DR (2012). Ultrasmall implantable composite microelectrodes with bioactive surfaces for chronic neural interfaces. *Nat Mater* **11,** 1065–1073.

Zienkiewicz OC, Taylor RL & Taylor RL (1977). *The finite element method*. McGraw-hill, London.